ANALYSIS TECHNIQUES FOR CHARACTERIZING HIGH POWER TURBULENT SWIRL FLAMES

A Dissertation

Submitted to the Faculty

of

Purdue University

by

Robert Z. Zhang

In Partial Fulfillment of the

Requirements for the Degree

of

Doctor of Philosophy

August 2019

Purdue University

West Lafayette, Indiana

THE PURDUE UNIVERSITY GRADUATE SCHOOL
STATEMENT OF DISSERTATION APPROVAL

Dr. Carson Slabaugh, Co-Chair

Purdue University, School of Aeronautics and Astronautics

Dr. Robert Lucht, Co-Chair

Purdue University, School of Aeronautics and Astronautics

Dr. Timothy Pourpoint

Purdue University, School of Aeronautics and Astronautics

Dr. Carlo Scalo

Purdue University, School of Mechanical Engineering

Approved by:

Dr. Wayne Chen

Head of the School of Aeronautics and Astronautics Graduate Program

To the halcyon visions of youth

ACKNOWLEDGMENTS

A great deal of appreciation is extended to Professor Lucht for taking me on as a graduate research assistant after my first semester at Purdue University. Due to human nature, hiring personnel can be lead to chaotic and unexpected outcomes, but I hope that my efforts have redeemed such risks. In a similar vein, I am grateful towards Professor Slabaugh and Andrew Pratt for their willingness to mentor me as a new student wholly unfamiliar with propulsion testing and laser diagnostics. In addition, thank you for bearing with me as my writing proficiency improved over the years.

As experimentation is the cornerstone of science, thanks must be extended to Robert McGuire for his fabrication expertise of propulsion testing hardware. Scott Meyer is commended for his efforts in keeping the lab running with ever growing research needs. His patience in training new students year after year and dealing with their foolhardy mistakes is admirable. Without the experience gained in previous generations of experiments, our lasers, cameras, and propellants would be directed towards an expensive pile of scrap metal and shattered quartz.

Lastly, the social aspects cannot be ignored in making the arduous process of research bearable. My colleagues at Zucrow Labs have made the unrelenting waves of challenges surmountable. Being around a diverse range of perspectives has opened my eyes towards multiple facets for self-improvement in both technical and soft skills. Assuredly, the community of the high pressure lab has shaped the following thoughts made digital.

PREFACE

The work presented in chapters 2 and 3 has been published in peer-reviewed journals. Chapter 4 is undergoing submission to the journal of Combustion and Flame.

Chapter 2 :

Robert Zhang, Andrew C Pratt, Robert P Lucht, and Carson D Slabaugh. Structure conditioned velocity statistics in a high pressure swirl flame. *Proceedings of the Combustion Institute*, 37(4):5031–5038, 2019.

Chapter 3 :

Robert Zhang, Isaac Boxx, Wolfgang Meier, and Carson D Slabaugh. Coupled interactions of a helical precessing vortex core and the central recirculation bubble in a swirl flame at elevated power density. *Combustion and Flame*, 202:119–131, 2019.

TABLE OF CONTENTS

Page

LIST OF TABLES

LIST OF FIGURES

Figure Page

SYMBOLS

d_j	Jet Diameter
Re	Reynolds Number
Da	Damköhler Number
K	Kelvin
λ_{ci}	Swirling Strength
u_x	Axial Velocity
u_y	Vertical Velocity
u_z	Out-of-plane Velocity

NOMENCLATURE

ACE	Aviation Combustion Experiment
PIV	Particle Image Velocimetry
SPIV	Stereoscopic Particle Image Velocimetry
CRB/Z	Central Recirculation Bubble/Zone
CFD	Computational Fluid Dynamics
LES	Large Eddy Simulation
DNS	Direct Numerical Simulation
CMOS	Complementary metal-oxide-semiconductor
SNR	Signal to Noise Ratio
OSL	Outer Shear Layer
LR	Lift-off and Reattachment
CNN	Convolutional Neural Network
TA	Thermoacoustic
PLIF	Planar Laser Induced Fluorescence
OH*-CL	OH* Chemiluminescence
PRECCINSTA	Prediction and Control of Combustion Instabilities in Industrial Gas Turbines
DMD	Dynamic Mode Decomposition
POD	Proper Orthogonal Decomposition
LPP	Lean premixed prevaporized

ABSTRACT

Zhang, Robert Z. PhD, Purdue University, August 2019. Analysis Techniques for Characterizing High Power Turbulent Swirl Flames. Major Professors: Carson D. Slabaugh and Robert P. Lucht.

High speed laser diagnostics are performed in two vastly differing swirl combustors at conditions relevant for industrial gas turbines. This high quality data can not only be used to elucidate key features of the flow field but also for validation of computational models simulating turbulence, chemistry, and their interactions. The first combustor is a piloted lean premixed prevaporized arrangement common in aviation applications. Fueling parameters are varied and sensitivity towards the pilot flame is observed. Conditioning to the stagnation line demonstrates increased fluctuations of shear and rotation in the inner shear layer when the pilot fueling is reduced.

The second flame has a simpler configuration with a single swirler and combusting natural gas. Thermoacoustic instability coupled to a helical precessing vortex core is found at certain conditions. Sparse Dynamic Mode Decomposition and phase averaging is applied to the velocity fields to create a three dimensional reconstruction of the helical vortex core in a non-precessing reference frame. Heat release is found to be correlated to the interaction strength of the central recirculation bubble and the helical vortex core.

Finally, intermittent phenomena within a thermoacoustic instability are examined. The most prominent deviation is that the flame is observed to randomly lift and reattach. In addition, a convolutional neural network is employed to extract the morphology from otherwise qualitative OH species imaging. The average characteristics of the lifted and attached flame are compared and dramatic differences are found. All of the flow structures have been altered such as the precessing vortex core being greatly intensified during flame lift-off. Evaluating the average events before flame

lift-off revealed the importance of conditions at the combustor inlet. However, evidence for a future reattachment event was only found with a less spatially confined perspective. In addition, transition to lift-off was very sudden while reattachment was far slower.

1. INTRODUCTION

The focus on renewable energy sources such as solar and wind has been in the public spotlight for the past few years. Energy production from coal and oil is projected to substantially decrease. Figure 1.1 shows the estimated split of world energy production through 2050 for an 2°C increase in global average temperature. Gasoline demands for transportation will fall if the rise of electric vehicles is sustained. However, combustion is still the dominant energy conversion mechanism as it accounts for natural gas and biofuels, which are projected to hold steady or grow through 2050. Increased demand for turbofans is evident in the civilian and military aviation markets as engine backlogs grow [3]. Just like the automotive and power generation industries, there is an overwhelming need to increase thermal efficiency and reduce harmful emissions [4]. To achieve these goals, there has been no shortage of research and development to advance gas turbine technology and maintain it as a viable solution for propulsion and power generation in the future.

Full scale engine testing is an extremely expensive endeavor and even component level tests are non-trivial. Large investments of capital are required for the necessary facilities and personnel. Reducing the amount of hardware failures and subsequent design/validation iterations is highly attractive. A competitor gains cost and time-to-market reductions. Therefore, improving design tools is a key priority for the any engine OEM. The physics involved in simulating an aviation combustor are as vast as the operating range that is required of it. A finalized design must take into account all aspects shown in figure 1.2.

Computational fluid dynamics (CFD) is a powerful design tool, but requires experimental data for validation of any modeled aspects. Direct numerical simulation (DNS) involves no modeling but is computationally impractical for the high Reynolds number flows of a industrial combustor. Large Eddy Simulations (LES) has

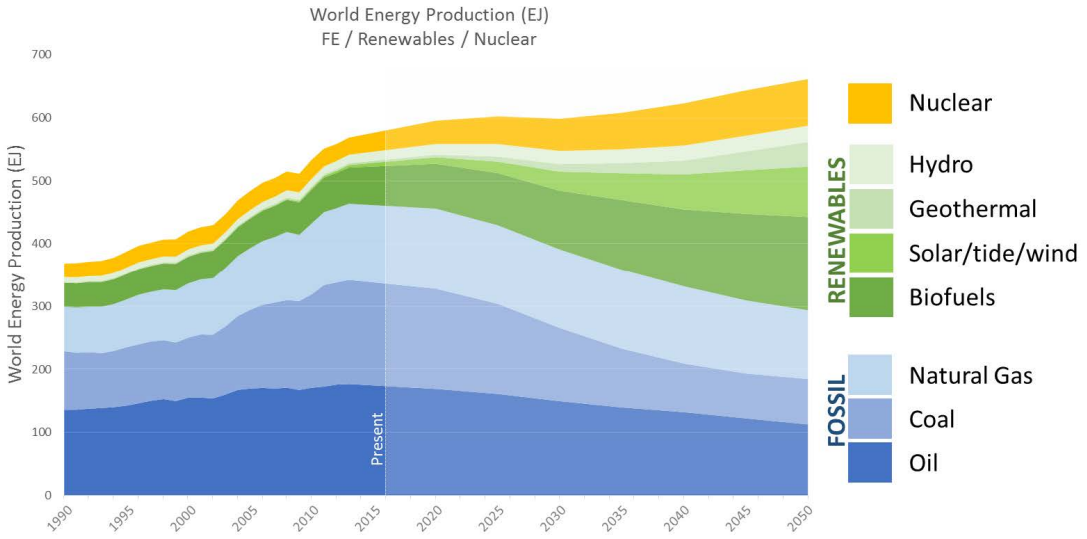

Figure 1.1. Projected Energy Production by Sources. 2015 IEA 2DS Scenario.

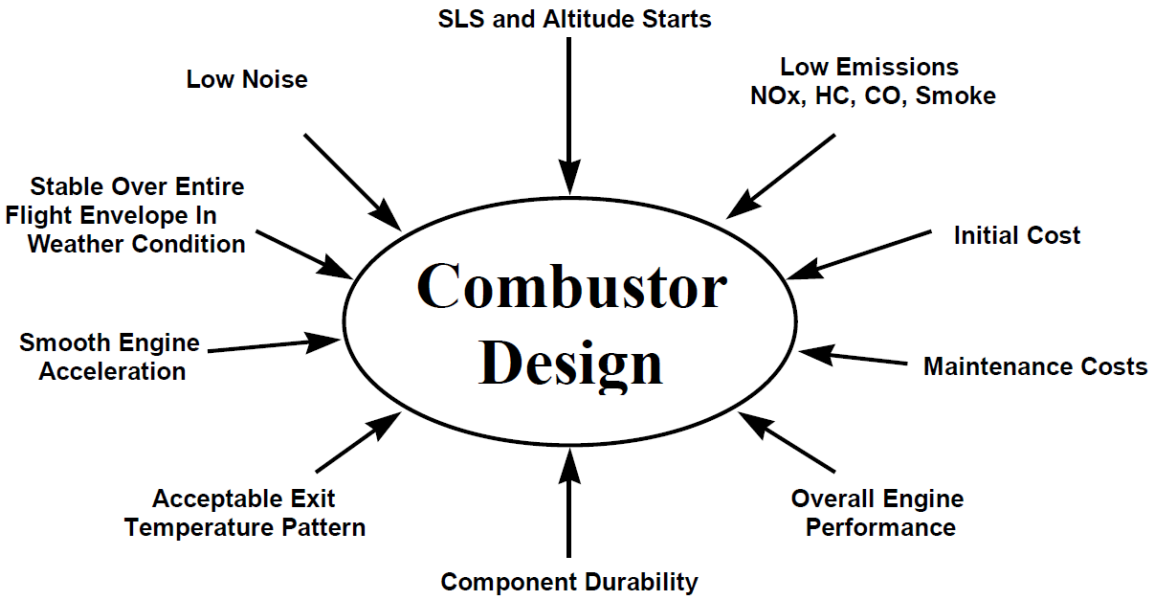

Figure 1.2. Combustor Design Requirements. Courtesy of Dr. Hukam Mongia.

shown increased use in simulating gas turbine combustors, but model development is still required for sub-grid scales and turbulence-chemistry interactions. In addition,

thermoacoustic instability is incredibly damaging and expensive to fix in real-world testing. Ideally, these issues are resolved during the design stage, but they have historically only shown themselves during actual hot-firing. Multiple studies using LES have been able to capture thermoacoustic instabilities mimicking their experimental counterparts but at great computational expense.

Geometrical complexity must also be held back in the interest of fast design iterations. This is an issue for experiments as well due to the complexity of full scale engine testing. Measurements from single element injectors contain all of the fundamental physics from a annular combustor but in an environment that is conducive to non-intrusive optical measurements. However, certain phenomena such as azimuthal thermoacoustic modes are not represented as well as flame-flame interactions between adjacent injectors. Also, inlet and exit boundary conditions are typically not mimicked to an actual gas turbine. The presence of a compressor and turbine can dramatically alter the acoustics within the combustor.

Heat transfer to the liner can affect pollutant formation and thermoacoustics. This is another aspect that is only beginning to be intensely investigated. Reduced temperatures at near-wall conditions can lead to increased CO production. Modeling of the combustor with adiabatic walls can misrepresent the operating window for thermoacoustic stability. These issues are obviously particularly important for flames attached to solid bodies, where perturbations of the flame root can have severe effects.

A key point is that combustion experiments at atmospheric conditions are insufficient to understand the behavior of industrial combustors operating at high temperature, pressure, and Reynolds numbers. A fully representative depiction of an industrial combustor cannot be realized by scaling size, velocity, and equivalence ratio at atmospheric temperature and pressure. Certain reactions show significant pressure dependence such as NOx and soot formation [5, 6]. Laminar and turbulent flame speed also vary greatly with chamber pressure [7, 8]. Reaction rates are exponentially dependent on temperature as seen in the Arrhenius equation that is typically used for combustion modeling.

The aviation industry has seen a trend towards higher pressure ratios in a search for thermal efficiency [9]. With large enough inlet temperature and pressure, atomization of liquid fuel injection undergoes major transformations. Fuel injection transitions from subcritical spray with droplets to a transcritical regime where the spray acts like a dense gas [10–12]. This fundamental change in mixing of fuel and air highlights the need for experimentation at these conditions and the added complexity of liquid versus gaseous fuels.

Moving towards higher Reynolds numbers broadens the spatial-temporal scales to ever finer levels. Longitudinal velocity spectra from multiple experiments demonstrating the turbulence cascade is shown in figure 1.3. The horizontal axis represents the spatial length scales while the vertical corresponds to a scaled energy. Higher Reynolds number flows are observed to have a wider range of length scales. One effect of particular importance to combustion is that a broader range of eddy lengths are formed. This enhances mixing of reactants and causes a flame speed acceleration at high turbulence intensities [13, 14]. Thermoacoustic instability can also become more likely as there are more eddy time scales to lock onto small pressure oscillations and initiate growth to higher amplitudes in a positive feedback cycle.

One could imagine that a different fuel and oxidizer combination could be substituted to mimic flame speeds at high pressure conditions, but that would fundamentally change the chemistry. In addition, increasing pressure increases the Reynolds number, which have consequences to the turbulent flow field. One could then increase the bulk velocity, which might cause the flame to extinguish or lower combustion efficiency. Alternatively, the combustor could be enlarged, but this changes the resonant frequency of the chamber affecting the acoustics. This thought experiment illustrates how certain dependencies of a combustor can be isolated for study, but the value of experimentation at industrial combustor conditions is paramount.

Laser diagnostics can unobtrusively probe temperature, species concentration, and velocity fields with high fidelity. Like any measurement, uncertainty or resolution limitations are present, which are exacerbated at the extreme operating conditions

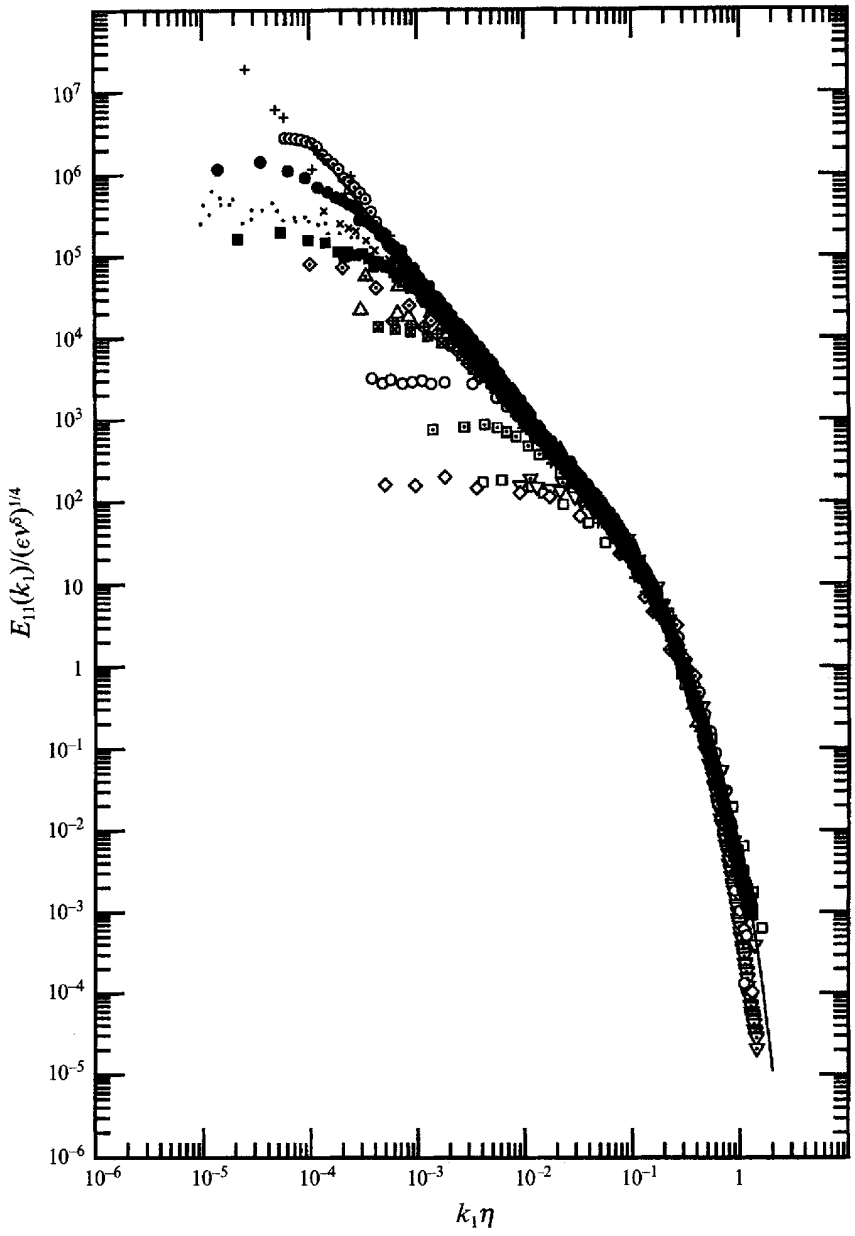

Figure 1.3. 1D longitudinal velocity spectra from many experimental investigations. Figure originally published by Saddoughi and Veeravalli [15].

of industrial combustors. The presented work analyzes such measurements in gas turbine combustors at industry relevant conditions. Such experimental undertakings are heavily time and money consuming, so novel data analysis techniques are utilized

to further enhance our understanding of turbulent combustion in these devices. Flow field sensitivities to fueling in an aviation combustor are first elucidated by tracking along a highly dynamic stagnation line instead of staying static. Turbulence is nothing if not chaotic, so there may be aspects that are hidden at first glance. Chapters 3 and 4 demonstrate this by first presenting a flame with limit-cycle thermoacoustic instability. Then the perspective changes to reveal that the flame was also undergoing intermittent lift-off.

2. STRUCTURE CONDITIONED VELOCITY STATISTICS IN A HIGH PRESSURE SWIRL FLAME

2.1 Introduction

Aerodynamic swirl stabilization is used in the majority of gas turbine combustors. Swirl keeps the combustor short thus saving weight and reducing overall engine size. The key feature of high swirl flows is a toroidal central recirculation zone (CRZ). The swirling flow eventually encounters vortex breakdown and is redirected upstream back towards the injector. These combusted gases transfer heat and radicals to the incoming reactant flow to sustain ignition [16]. Large mass flows of fuel and oxidizer must be mixed and reacted to create a compact and energy dense flame. With a deep spectrum of length scales produced at high Reynolds number, the reactants can be rapidly mixed. For example, a volume with high fuel mass fraction will encounter eddies of multiple sizes. The fuel volume will be fragmented into smaller clusters, drastically increasing its surface area. Molecular diffusion can now effectively bring species together for reaction [13]. This along with secondary recirculation zones to increase residence time has enabled a reduction in combustor size.

Laser based techniques can provide quantitative measurements of physical properties in reacting flows, including temperature, species concentration, and gas velocity. With the advances in the quantity and depth of information that can be acquired with high-speed measurements, there has been significant interest in the extension of these capabilities from canonical, laboratory-scale flames to large-scale facilities. High speed cameras and lasers are necessary to capture complex flow-flame interactions. Increasing pressure to simulate industrial engine operation results in high Reynolds number flows, creating a spectrum that extends to ever smaller spatial and temporal scales. For example, the Princeton Superpipe operates at over 22 MPa and has eddies

the size of typical PIV seeding particles for reacting flows [17]. Therefore significantly more resolution is needed to describe the flow field in a high pressure combustor at all scales. Nevertheless, high speed laser diagnostics have been successfully utilized to investigate the larger scales. Experimental efforts are focused on understanding parameters that affect combustor performance such as thermo-acoustics and coherent flow structures.

High pressure swirl flames have been investigated by a few groups with kHz rate laser diagnostics. Slabaugh et al. demonstrated 5 kHz PIV/OH-PLIF measurements in a liquid-fueled aeropropulsion combustor at up to 1.4 MPa. They achieved suitable resolution to image large-scale turbulent structures and used conditioned statistics to observe a bias towards lower velocity magnitudes normal to the flame front [18]. The well characterized dual-swirl burner was elevated to 500 kPa, and simultaneous 3 kHz PIV and OH-PLIF measurements were taken. The location of the recirculation zone was found to be consistent with the reaction fronts. The combustor also displayed thermo-acoustic pulsation, but no precessing vortex core was present, a dominating feature at atmospheric pressure [19]. Another swirl-stabilized liquid-fueled flame at 520 kPa was studied with 5 kHz stereoscopic PIV and PLIF. The authors showed how the flame shape and position changes with inlet temperature and equivalence ratio [20].

The intent of this work is to elucidate sensitivities in an aviation combustor to operating conditions. Stereoscopic-PIV (SPIV) is performed at various fuel flow rates with constant inlet conditions. Conclusions from unconditioned statistical moments can be found wanting. Results presented in this article involve conditioning velocity and spatial gradient derived measures based on the instantaneous position of a stagnation line, a coherent flow structure, at three operating conditions. The stagnation line represents the interface between reactants and recirculated combustion products. The dynamics of this interface affect flame stability in terms of both local equivalence ratio and gas velocity. The spatial distribution of conditioned statistics are then examined relative to the changes in fuel distribution. Dynamic mode and

proper orthogonal decompositions are another direction for analysis and has shown great insights for combustors exhibiting thermoacoustic instabilities [21]. However, no coherent thermo-acoustic pulsation was observed, and their application on this SPIV dataset was not a focus for this paper.

2.2 Experimental Configuration

The Purdue high pressure Aviation Combustion Experiment (ACE) has been well documented in previous works [18, 22], hence, only a brief explanation is given. A piloted, partially premixed, liquid-fueled swirl burner is installed. High pressure, preheated air is supplied to the pilot and main air swirlers from a common manifold. Two independently controlled and metered circuits deliver fuel to the pilot and main nozzles for control of the pilot-main fuel split. Figure 2.2 shows a schematic of the fuel nozzle with its air and fuel routing. The combustor has a square cross-section with windows on all four sides. The exhaust is directed through a contraction, a common feature for gas turbine combustors. The operating conditions studied are summarized in table 2.1. The Reynolds number based on unburned reactants and combustor inlet geometry was 140,000 and 105,000 for the pilot and main flows respectively. The investigated operating conditions displayed no combustion instability. This was determined by pressure and optical measurements. Considerable quenching water is injected downstream of the combustor and is highly absorptive of pressure oscillations. The rig has very consistently shown a lack of combustion instabilities with multiple burners.

Figure 2.1 shows a detailed view with respect to the injector for these measurements. Labeled flow features are overlaid on the average velocity field. Annotation 2 corresponds to the black line denoting the stagnation line bordering the CRZ (1) and the pilot jet (3). Variations along this stagnation line will be discussed in this paper. Since the pilot flame is expected to keep the combustor lit even in adverse conditions, this interface is of great interest. Obviously, the entirety of the CRZ is not within

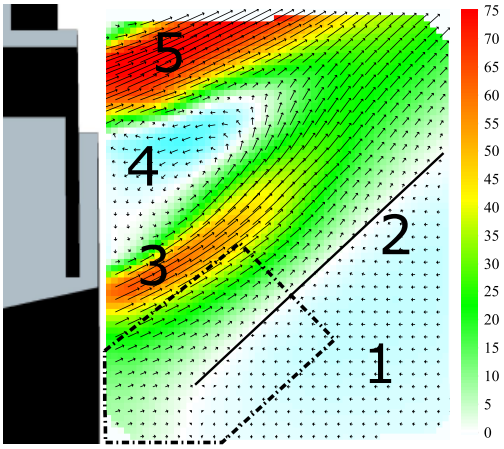

Figure 2.1. Averaged velocity field with labeled flow features. Contours denote the axial component, and vectors correspond to the in-plane components.

Table 2.1. Operating conditions studied.

Operating Condition	Pressure (P3) [MPa]	Temperature (T3) [K]	Thermal Power [kW]	Pilot Fuel Split [%]	Overall ϕ
A	1.0	700	500	20	0.50
B	1.0	700	360	20	0.34
C	1.0	700	390	50	0.37

the field of view as it greatly extends downstream. Annotation 4 represents the small recirculation zone from the bluff-body of the injector, and 5 is the main jet. The pilot jet interaction with these flow structures is highly complicated and dynamics can be intermittent.

2.2.1 Stereoscopic particle image velocimetry

A dual-cavity, diode-pumped, solid state Nd:YAG laser (Edgewave IS811-DE) provided 532 nm light at 5 mJ/pulse with a repetition rate and pulse separation of 6 kHz and 4 μs, respectively. Four cylindrical optics formed the laser sheet to approximately 650 μm wide. A fluidized bed was used to seed Titanium Dioxide

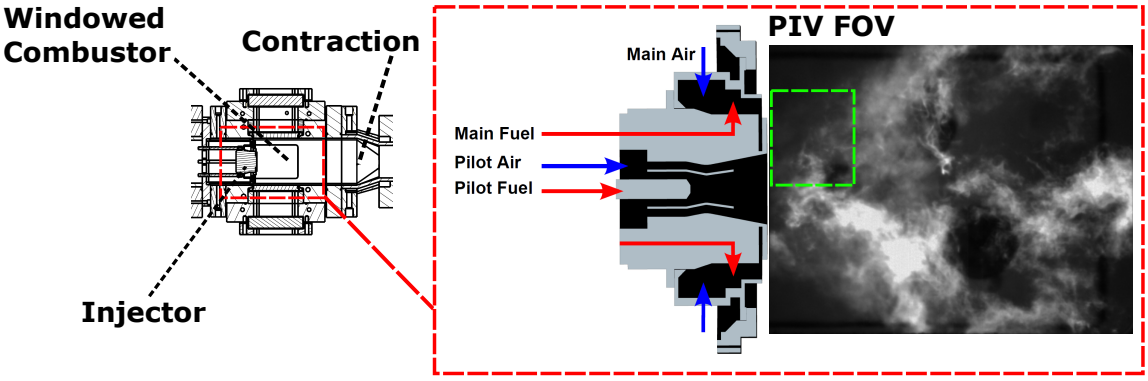

Figure 2.2. Combustor schematic with SPIV measurement domain highlighted over an instantaneous visible emission image.

(TiO_2) particles, 250nm in diameter, into the combustor air flow. The average seed density within the combustor was approximately 0.01 particles/pixel.

Two high-speed CMOS cameras (Photron SA-4), positioned on opposing sides and looking up towards the laser sheet, recorded the Mie scattering from the particles through 200 mm focal length, f/4.0 objective lens (Nikkor AF-S Micro). LaVision v3 Scheimpflug adapters were mounted onto both cameras to correct for defocussing of the tilted image plane relative to the laser sheet.

Raw images were masked to remove solid bodies and dense fuel sprays. A 5x5 pixel window sliding minimum was subtracted from each image to remove unwanted background intensity. Images were then intensity normalized to remove variations in particle illumination. Stereo self-calibration was performed for each dataset. Average image disparity between cameras was less than one pixel after corrections. The velocity field was calculated using a multi-pass stereo cross-correlation algorithm (LaVision DaVis 8.3.0). Spatial derivatives were calculated on an interpolated velocity field. Vector dropouts were filled in with values determined by the average of its neighbors. All spatial dimensions are normalized by the average pilot jet diameter, d_j. The velocity fields were processed using a final window size of 32 x 32 pixels with 75% overlap resulting in 0.0588 d_j vector spacing thus 0.1764 d_j vector resolution. 3000 image pairs were recorded for each test condition.

2.3 Stagnation Line Conditioning

In turbulent swirling flows, the large scale structures are highly dynamic. To better understand the fundamental mechanisms of their interaction, conditional sampling of the instantaneous flow-field based on proximity of the large-scale structures can elucidate key dynamic features of the reacting shear layer. We describe the boundary of the CRZ and pilot jet by a stagnation line defined in terms of axial velocity. Without a measure of combustion radicals, such as OH or CH, we cannot explicitly relate the stagnation line location to a flame front. Nevertheless, given the extensively

documented structure of swirl stabilized flames, the shear layer between the reactant jet and CRZ is a location for flame stabilization [23, 24]. We can infer this notion, because the CRZ's role is to transport combustion products that will then cross the stagnation line into the pilot jet to maintain ignition.

A marching squares algorithm [25, 26], is used to calculate the axial and vertical positions of the constant axial velocity contours. The constant was set at +1.0 m/s instead of exactly 0 m/s. Biasing towards positive velocities allowed for the isocontour to more reliably track the shear layer and not deviate into the CRZ interior at certain instances due to large turbulent fluctuations within the CRZ. The detected iso-contours were then filtered based on length. The length thresholds were determined by analyzing the contour length histogram of each dataset prior to filtering. The histograms were found to be bimodal, and the threshold was determined by the minimum between the two maxima [27]. The threshold was 6 d_j and effectively removed small contours that do not correspond to any large scale stagnation line. An additional filtering operation was then applied to remove contours that were not within the proximity of the expected spatial location of the CRZ boundary. If no portion was found in the root of the pilot jet and CRZ border, shown by the dashed region in figure 2.1, then they were neglected. Typically these filtering steps result in one stagnation line per time step.

The instantaneous stagnation line positions are interpolated back to the grid coordinates of the original velocity field. A bivariate pdf is generated from the aggregated spatial coordinates. Figure 2.3 shows side-by-side a representative instantaneous stagnation line with the bivariate pdf for condition B. The detected stagnation lines occasionally wrap around the entirety of the pilot jet, which explains the higher probability density near the injector's bluff body. This feature is highlighted in figure 2.3 as a green ellipse that corresponds to the border between the pilot jet and bluff-body recirculation zone. It is less evident for conditions A and C, where more fuel is introduced through the pilot. Greater amounts of high viscosity and low density product gas dampens the pilot jet flapping. Unconditioned average axial velocity also

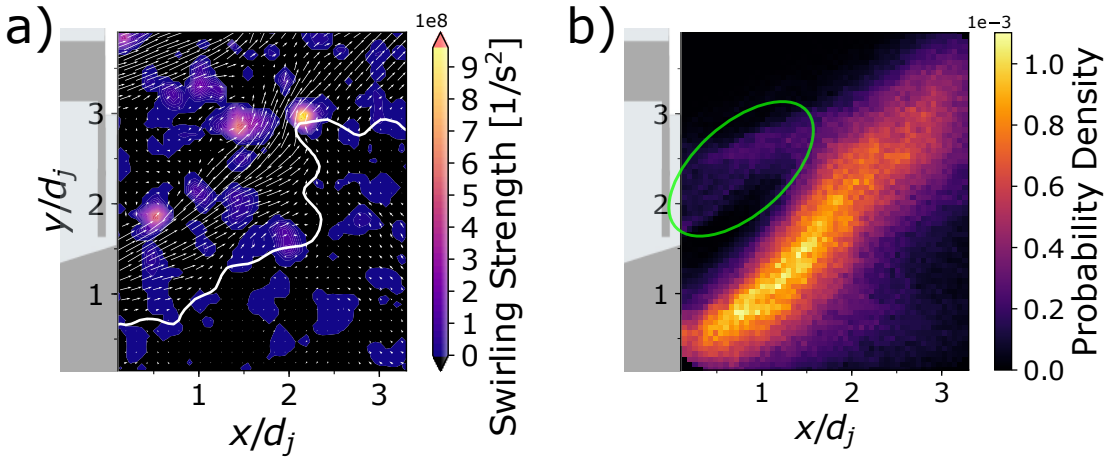

Figure 2.3. (a) Instantaneous stagnation line plotted in white. In-plane velocity vectors overlaid on contours of swirling strength. (b) Joint pdf of the stagnation line position.

shows greater penetration of the pilot jet into the combustor for conditions A and C, where C has the strongest jet. This is to be expected as the jet velocity is increased from a less dense pilot flame.

Conditioning along the instantaneous stagnation line allows for a description of the flow field that is not fixed to the lab reference frame. The stagnation line positions act as a mask that can be applied to other quantities. Conditioning velocity or its spatial derivatives is straightforward, because the mask has a direct correspondence to the original velocity grid. The normal vector and curvature of the stagnation line are interpolated by binning values between the grid edges. The value for a specific spatial coordinate is taken as the mean of all values that lie between the grid edges. If a grid center had less than 30 conditioned data samples, corresponding to 1% of the number of time steps, then that location was removed when calculating statistics.

2.3.1 Curvature

Curvature of the parametrically defined stagnation line was calculated by $\kappa = \frac{x'y'' - y'x''}{[(x')^2+(y')^2]^{\frac{3}{2}}}$. Typically, this is used to detect flame-front contours from thinned gradients of PLIF images [28, 29]. Due to the second order derivatives from a lower resolution PIV grid, the curvature values are expected to be noisier than typically seen PLIF contours. A Savitsky-Golay filter was applied to smooth the stagnation lines with a window length of 13 and second order polynomial fitting. Following the findings of Haq et al. in resolving curvature of digitized circles, a threshold for the maximum curvature was applied to the filtered contours [30].

Figure 2.4 displays the mean stagnation line curvature for condition B. Stagnation lines closer to the average pilot jet location show positive curvature. Moving towards the center of the combustor, the mean curvature becomes negative. This transition is gradual and persists along a upward diagonal trajectory through the measurement domain. The stagnation line is expected to have an oscillatory shape due to vortex shedding from the pilot shear layers. Circled in green is the border between the pilot jet and bluff-body recirculation zone. Curvature shows the same characteristic sign change across this shear layer with positive values near the pilot jet. The spatial length scales are smaller here as compared to the side bordering the CRZ. Larger vortices are being shed from the pilot jet into the CRZ thus changing the stagnation line curvature over a wide spatial extent.

2.4 Results

2.4.1 Velocity

The mean conditioned out-of-plane velocity (u_z) is displayed in figure 2.5b for condition A. A portion of the spatial domain is masked due to glare in the raw images that introduced a clear measurement bias in u_z. However, the statistics of the in-plane velocities were not drastically affected by the glare. u_z values are predomi-

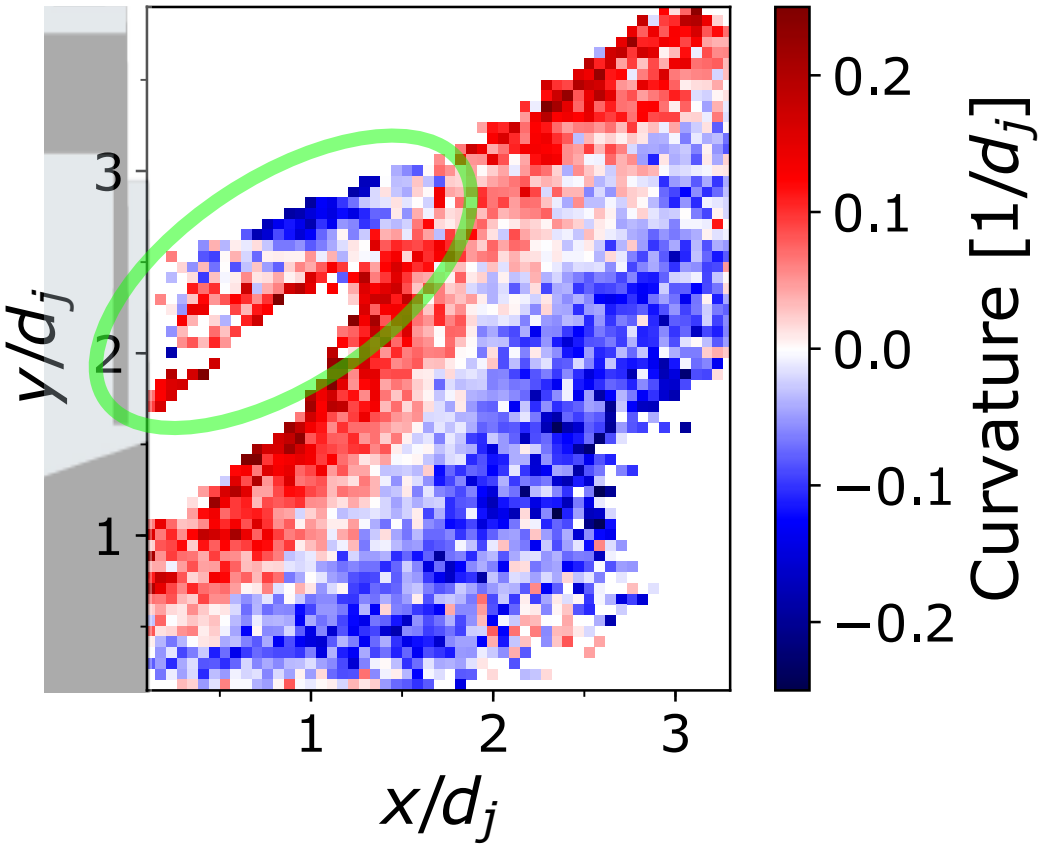

Figure 2.4. Mean stagnation line curvature for condition B.

nantly negative due to the orientation of the bulk swirl. There is a concentration of high magnitudes from roughly $\frac{x}{d_j} = 1.0$ to $\frac{x}{d_j} = 2.5$. The fluctuation RMS statistic also has the highest values in this region, so there is a clear increase in out-of-plane motions for this portion of the flow. The spatial location of this feature does not vary greatly between the operating conditions studied. However, mean and fluctuation RMS magnitudes are appreciably larger for condition A than B or C, which is attributed to the higher global equivalence ratio of condition A (see table 2.1).

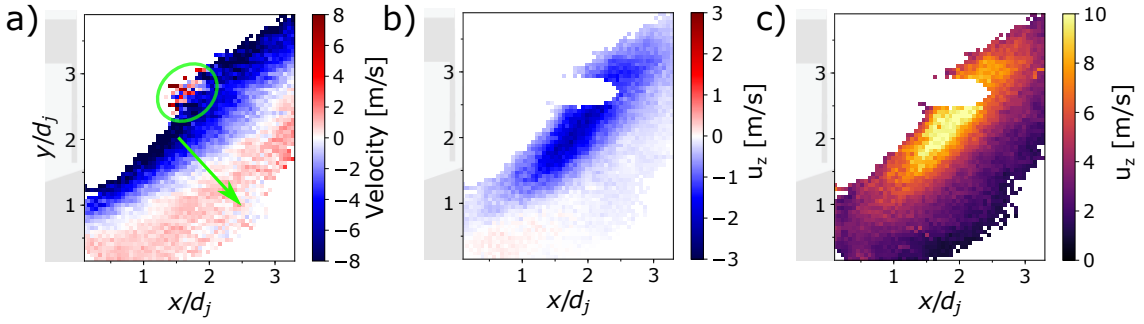

Figure 2.5. Conditioned velocity for test condition A. Mean stagnation line projected velocity (a), conditioned mean of u_z (b), and fluctuation RMS (c) of u_z.

2.4.2 In-Plane Shear

The average in-plane shear, $S_{xy} = \frac{1}{2}(\frac{\partial u}{\partial y} + \frac{\partial v}{\partial x})$, can highlight variations in the local shearing dynamics with changing fuel flows. Furthermore, in the presence of highly three-dimensional vortical structures, the local S_{xy} magnitudes have been shown to be elevated [31]. Mean and fluctuation RMS statistics were calculated on the conditioned S_{xy}. Figure 2.6 compares the spatial distributions for conditions B and C; the two conditions with comparable global heat release but largely different pilot-main fuel splits.

Figure 2.6b indicates the mean conditioned shear for condition C. Since C has the highest pilot fuel flow rate, there is higher positive shear near the root of the pilot jet. Figure 2.6c presents the conditioned fluctuation RMS of 2.6, which has a concentrated maximum in the region of (x,y) = (1.7, 2.5). Circled in figure 2.6c is a concentration of large fluctuation RMS for condition B. B has the lowest pilot fuel flow, which was previously shown to result in wider spatial traverses of its stagnation line. Therefore, a more stationary pilot jet leads to the absence of a fluctuation RMS hotspot. The circled location in figure 2.6c also corresponds to where shear displays negative values in the mean. When the stagnation line appears in this location, the pilot flow will

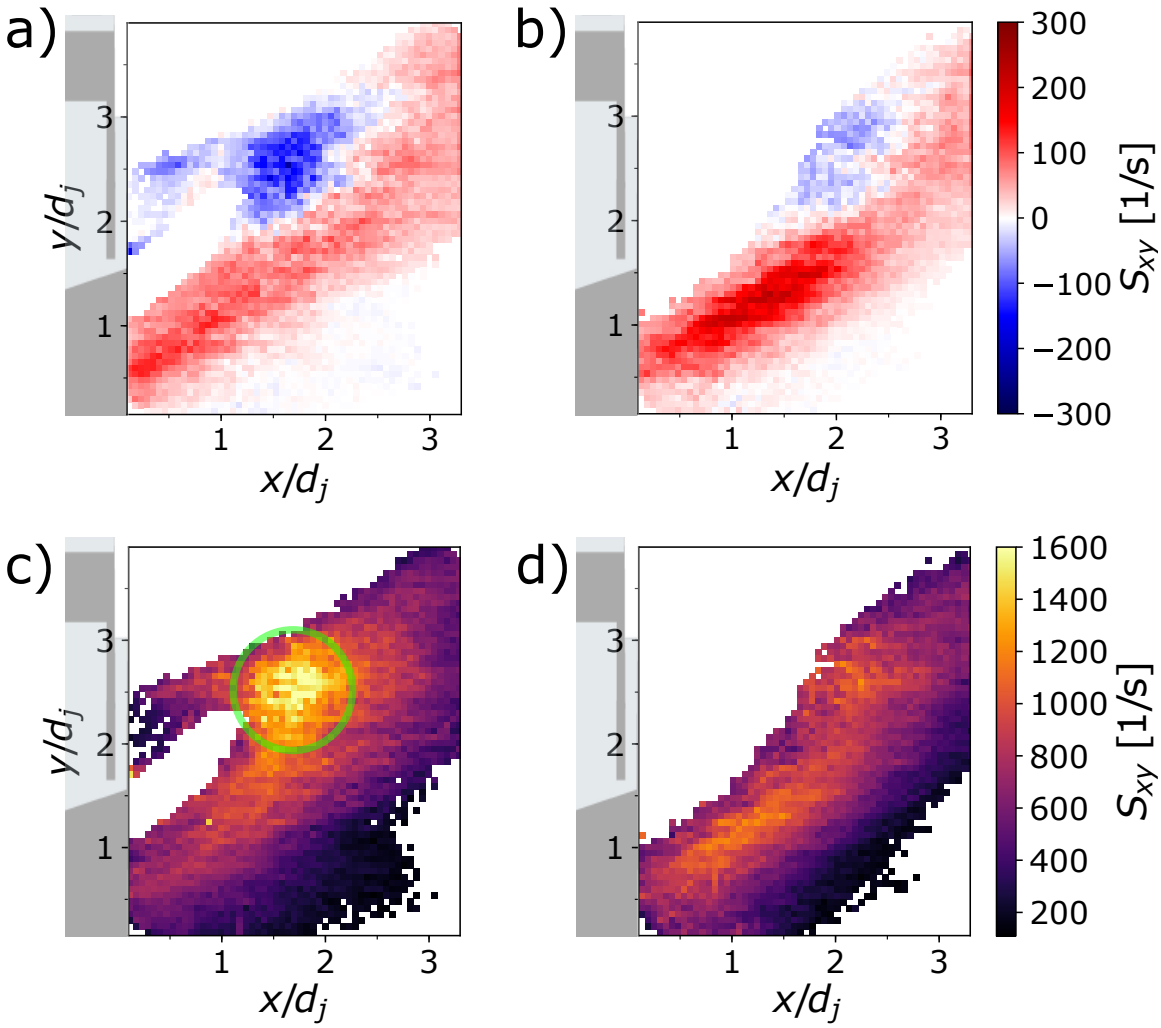

Figure 2.6. Mean and fluctuation RMS of in-plane shear for test conditions B (a & c) and C (b & d).

be mixing with the main jet and bluff-body recirculation flows. This is no longer the pilot jet shearing against a low velocity CRZ. The sign of mean S_{xy} reverses indicating a directional change in the shearing of fluid elements. This interaction is prevalent for all operating conditions, and a key feature of this combustor for reactant mixing and flame stabilization.

2.4.3 Swirl Strength

The imaginary component of the complex eigenvalues of the velocity gradient tensor was used by Zhou et al. to define the swirling strength to identify hairpin vortices [32]. In particular, iso-surfaces of squared swirling strength (λ_{ci}^2) were illustrated, and the presented figures follows their convention of the squared term. Adrian et al. showed that iso-contours of swirling strength were the most reliable method evaluated in their study to identify eddies from 2D PIV in a pipe flow [33]. No decomposition of the velocity field or change of reference frame is necessary. Using vorticity is undesirable for vortex identification, because it does not discern between shearing or swirling motion. However, any vortex that has its axis aligned in the measurement plane will not be detected from planar PIV. Only vortices that have out-of-plane alignment with respect to the laser sheet will be found.

Figure 2.7 shows the mean conditioned swirling strength for all reacting test conditions. Condition B contains two regions of very high swirling strength circled in green. The first circled region, centered at $\frac{x}{d_j} = 2.0$ and $\frac{y}{d_j} = 2.5$, corresponds to vortex shedding from the pilot jet into the CRZ. The large magnitude and spatial extent illustrate the enhanced hydrodynamic instability of the stagnation line associated with low pilot fueling. Based on observation from the instantaneous velocity fields, the pilot jet also has the largest radial excursions either into the main jet or CRZ. Higher swirling strength magnitudes indicate faster rotating vortices. This can result in local extinction events that increase the unsteadiness seen in the shear layer from lower pilot fueling. The second circled region for condition B, centered at $\frac{x}{d_j} = 1.25$ and $\frac{y}{d_j} = 2.6$, is due to the vortex shedding from the side of the pilot jet bordering the bluff-body recirculation zone. This is not detected for A and C due the motion of the stagnation line mentioned in section 3.

Condition A has a slight concentration of large swirling strength at $\frac{x}{d_j} = 2.0$ and $\frac{y}{d_j} = 2.5$, but the intensity is much lower than condition B. C displays the lowest swirl strength but a more uniform spatial distribution. This suggests that lower pilot

fuel percentages produce a localized region of large swirl strength. Lowering global equivalence ratio while keeping the same fuel split has a dramatic effect as shown from conditions A to B. Stronger vortices are frequently shed at the extremity of the pilot jet at the leaner pilot flames.

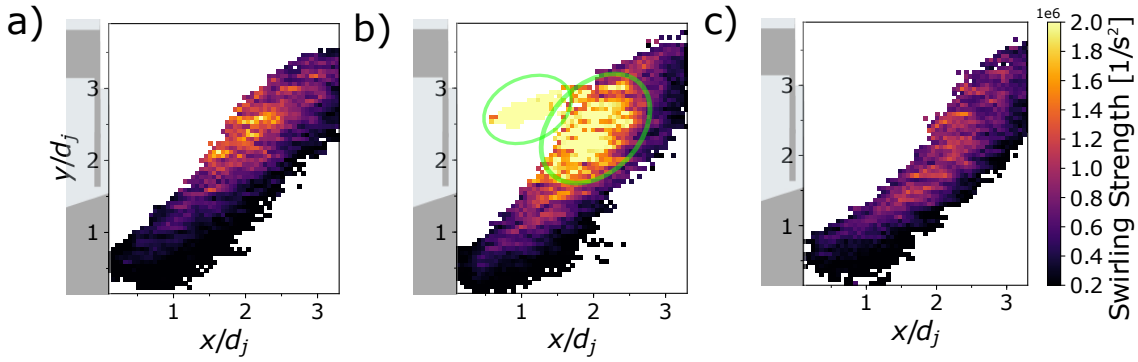

Figure 2.7. Mean swirling strength for conditions A (a), B (b), and C (c).

Similarities appear between the mean spatial distributions of u_z and swirling strength. Figure 2.8 shows a scatter plot of swirling strength with respect to u_z with points colored by S_{xy} for condition B. Scatter plots for the other operating conditions showed similar trends. As swirling strength increases, the range of u_z increases in both positive and negative directions. However, beyond swirling strength values of 10^7, there is no more growth in u_z range. Any vortex with significant rotation seems to correspond to large values of u_z indicating strong helical motion. The entirety of a vortex will show large swirling strength values, while only a portion it may be at the most extreme u_z magnitudes. This explains why the range of u_z increases. Large magnitudes of S_{xy} occur at all levels of u_z and swirling strength. However, it is most dense at swirling strengths above 10^8. This means that intensely swirling eddies are creating regions of high shear stress, which is beneficial to entrain combustion radicals into the pilot jet across the stagnation line.

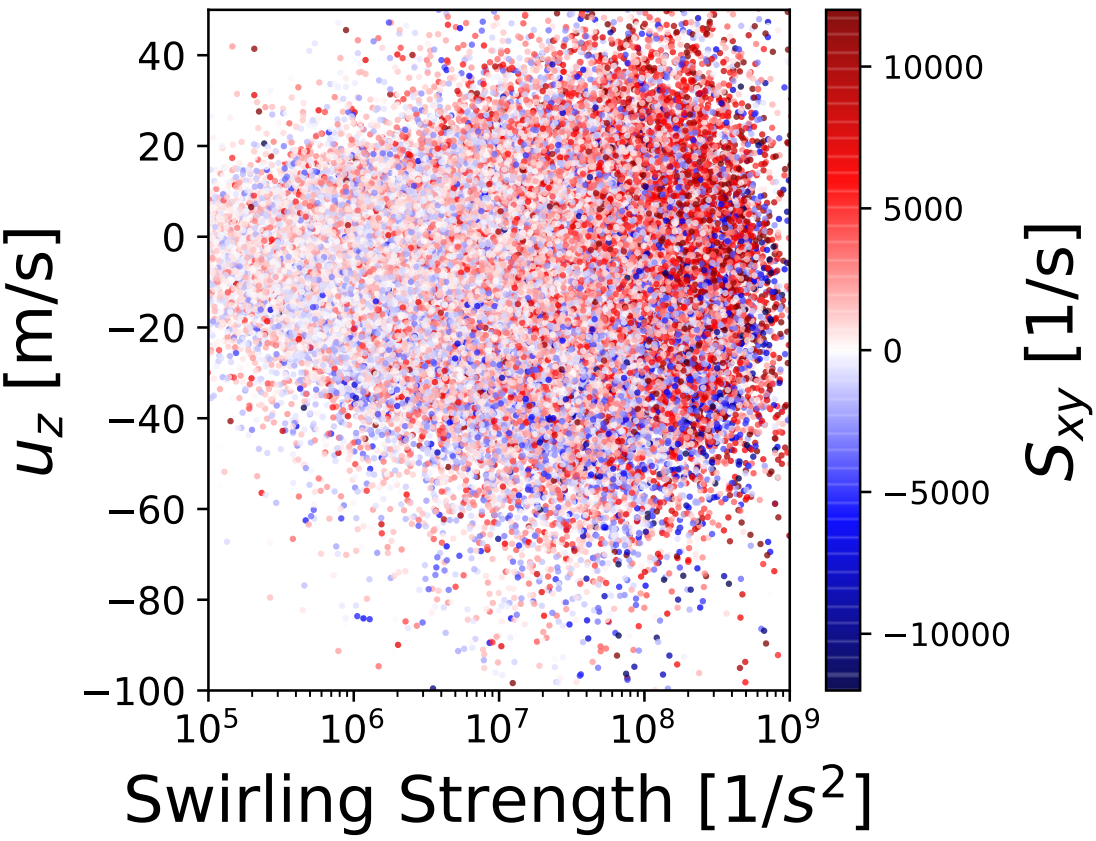

Figure 2.8. Scatter plot of swirling strength and u_z with points colored by S_{xy} for condition B. Points with low values of S_{xy} have a degree of transparency. Swirling strength is plotted logarithmically.

2.5 Conclusions

The stagnation line bordering the CRZ and the pilot jet was targeted for extraction at three operating conditions. Certain stagnation lines also included the pilot jet and bluff-body recirculation interface due to the dynamics of the pilot jet in condition B, but this was not heavily focused upon. The velocity field and its derivatives, such as swirling strength, were conditioned along this stagnation line to discriminate variations in flow structures with varying pilot to main fuel ratio and global equivalence ratio.

Statistical analysis on the conditioned results displayed distinct spatial patterns. The statistics of u_z, stagnation line projected velocity, and stagnation line curvature were invariant to operating condition. This can be a desirable feature in aviation combustors. They must meet performance parameters such as flame stability and combustion efficiency throughout an enormous range of operating conditions. However, swirling strength and shear show significant differences based on fueling. Statistics from condition B display a concentrated region of large in-plane shear and swirling strength that are not seen in the other two reacting conditions. The fuel nozzle design dictates that reducing pilot fueling and global ϕ will make flame stabilization more difficult; thus, displaying that flameout margin will depend heavily on the conditioned swirling strength and shear.

3. COUPLED INTERACTIONS OF A HELICAL PRECESSING VORTEX CORE AND THE CENTRAL RECIRCULATION BUBBLE IN A SWIRL FLAME AT ELEVATED POWER DENSITY

3.1 Introduction

Swirling flows are often used in aerospace and industrial combustion systems. A bulk swirling flow is typically generated by fixed vanes upstream of the combustion zone. If the geometry of the combustor promotes a sufficient level of swirl, the bulk swirling flow breaks down and generates a central recirculation bubble (CRB) [24]. This allows for hot combusted gases to recirculate back to the fresh reactants, thus stabilizing the flame. A CRB may also be formed by other means (such as a bluff-body), but swirl induces greater mixing through strong shear layers. Swirl also produces a compact flame, because fuel and oxidizer mixing is enhanced through vortex rollup events with the CRB [34]. This characteristic is highly desirable for aviation applications where reducing combustor weight and size is vital.

In a global effort to reduce NO_x and particulate matter (smoke) emissions, the gas turbine industry has given increased focus to lean combustion system, with (partial) premixing [16]. An undesirable consequence of this operating condition is an increased susceptibility for combustion dynamics, where pressure oscillations couple with the flame heat release in a positive feedback loop that can negatively impact engine performance and significantly reduce combustor life. Operating near the lean blowout limit allows for smaller hydrodynamic pertubations to greatly affect heat release through extinction and re-ignition events [35, 36]. Modern combustors also use less liner cooling air to allow more air into the combustion zone and improve

the temperature distribution to the turbine. This cooling flow is then less effective at absorbing acoustic oscillations as it begins to act as a hard instead of a porous wall [37,38]. The susceptibility of a combustor to instability would ideally be foreseen in the design phase and remedied, but computationally inexpensive numerical tools have not demonstrated such predictive capabilities with engine-relevant conditions and geometries. Extensive studies involving complex computational simulations and experimental measurements have been undertaken to understand and control combustion dynamics. However, more work is required to achieve this capability, especially in practical applications with increased flame power density and complex combustor geometries [39].

As a target case for the International Workshop on Measurement and Computation of Turbulent Flames, the PRECCINSTA gas turbine model combustor (GTMC) has been the subject of extensive experimental and numerical investigation at atmospheric pressure. In a distinct range of operation, this GTMC has been shown to exhibit strong self-excited thermoacoustic pulsations. Meier et al. performed a detailed experimental characterization of this unstable operation by studying two different equivalence ratio conditions [40]. Utilizing multiple laser diagnostics, significant differences were observed between the quiet and noisy (unstable) flames with respect to the turbulent flow structure, mixing characteristics, flame shape, and the reaction progress. These results showed that the feedback loop for the sustained, self-excitation of thermoacoustic oscillations in the PRECCINSTA GTMC (at atmospheric pressure) was an oscillation in mixture fraction coupled with a convective time delay. Franzelli et al. performed LES computations, which agreed with the previous experimental findings of equivalence ratio oscillations driving the thermoacoustic instability [41].

Subsequent investigations with 10 kHz PIV and OH-PLIF identified the presence of a helical precessing vortex core (PVC) only in the unstable flame by inspecting the time-evolution of the flow field and proper orthogonal decomposition (POD). The stable flame only displayed periodic formation and ejection of symmetric vortex

pairs in the inner shear layer. The PVC was hypothesized to be strongly coupled to the thermoacoustic oscillation, because the PVC precession frequency occurred at an integer multiple of the thermoacoustics [42, 43]. However, later experimental findings have shown that the PVC frequency can be at non-integer multiples of the thermoacoustic pulsation [44]. Oberleithner et al. identified operating conditions that displayed intermittent flame shape transitions between V and M flames in the PRECCINSTA GTMC [45]. It was found that the formation of a PVC was a precursor to the M flame shape and increased pressure oscillations. The generation of a PVC was coupled to the density and mean flow fields at the combustor inlet. A suppression of the radial density gradient resulted in the formation of the PVC, thus leading to lift-off of the flame root from the combustor nozzle.

Flames must also be studied at industrial engine relevant conditions, because coupling mechanisms can develop from a much broader spectrum of physical processes at high power density and Reynolds number. Swirl stabilized flames are particularly complex because the flow structure supports a wide range of interacting hydrodynamic structures. Experimental studies on the role of a PVC in relation to combustion dynamics are far fewer at elevated pressure and temperatures conditions where industrial engines operate. This is attributed to the increased infrastructure requirements as only a few research labs in the world have capabilities to operate combustors at the megawatt level [22, 46–48]. Combined with the requirements of optical access for laser diagnostics, the sparsity of such investigations in the literature is perhaps unsurprising. The current work adds to the literature on combustion instability at conditions approaching those found in a gas turbine engine.

Slabaugh et al. investigated the PRECCINSTA GTMC at DLR-Stuttgart with simultaneous OH*-CL, SPIV, and OH-PLIF at two equivalence ratios and at elevated pressure and temperature [44]. They found that the lower equivalence ratio condition led to combustion dynamics and coincided with the appearance of a PVC. At atmospheric conditions, the PVC precession occurred at a constant Strouhal number, and this was still the case for the elevated pressure results. However, the PVC

precession frequency was twice the highest values reported for atmospheric operating conditions. A reconstructed velocity field from the ten most energetic POD modes displayed the PVC drastically distorting the CRB. Therefore, the PVC is coupled to the thermoacoustics by modulating mixing in the reacting inner shear layer similar to findings at atmospheric conditions. This study expands upon the previous elevated pressure findings where the time-scale of the PVC precession is nearly four times that of the thermoacoustic instability. An extensive characterization of the three dimensional structure of the PVC and CRB interaction is presented to further elucidate the mechanism of the self-sustained thermoacoustic oscillation.

3.2 Experiment Configuration

3.2.1 Burner and Flame

With an extensive experimental and numerical database in place for atmospheric pressure flame conditions, the focus of the present work is to characterize the PRECCINSTA GTMC at elevated thermal power density operation. The geometry of the mixer and nozzle have remained unchanged, with natural gas and air being *technically premixed* (not perfectly premixed [49]) in the swirler section using 12 radial vanes and 12 corresponding $1\,mm$ fuel injection ports. The exit of the nozzle is $27.85\,mm$ in diameter, with a rounded, conical center-body aligned to the central axis.

Figure 3.1 displays the installation of the PRECCINSTA burner into the High Pressure Optical (HIPOT) test rig operated at DLR-Stuttgart. Full optical access to the flame is provided through all four walls of the combustion chamber using a series of fused quartz windows. In-depth descriptions of the combustor geometry and experimental platform is provided in [44]. All operating conditions, including pressures, temperatures, and air/fuel/water mass flow rates were monitored and recorded at a $1\,Hz$ interval. Dynamic pressures were also measured in the upstream plenum, the combustion chamber, and the downstream section with high-frequency piezo-resistive pressure transducers (Kistler 4043A with a 4603A amplifier). The signals were simul-

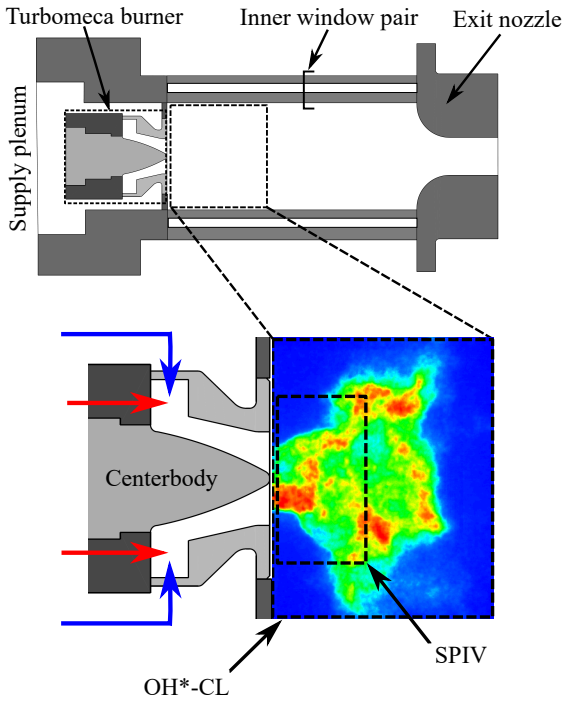

Figure 3.1. Schematic of PRECCINSTA burner installed into HIPOT test rig with measurement fields of view indicated.

taneously recorded (with dedicated A/D converters) at 100 kHz, below the natural frequency of the instruments, along with the intensifier gate signal from the OH*-CL detection system in order to synchronize the optical measurements to the measured acoustic signals.

Previous work investigated two operating conditions: one flame was stable (Flame A) and the other (Flame B) exhibited thermoacoustic instabilities. All conditions were identical between the two cases except for the fuel mass flow rate, which was lower for the unstable case [44]. The presence of a PVC was evident in the flow field measurements from Flame B. The PVC was not present in the stable case, Flame A. Therefore, Flame B was chosen for more extensive analysis relating to the observed thermoacoustics in this work. The global equivalence ratio was 0.58, and the flame thermal power was $150\,kW$. The inlet air mass flow rate of 88 g/s was preheated to 600 K, and the combustor was operated at 0.5 MPa. This resulted in a

bulk velocity of 55 m/s, and a Reynolds number, based on the nonreacting flow, of 130,000. The Damköhler number was estimated to be 0.04 for this flame. This was based on the integral time scale computed in the previous study, and a chemical time scale calculated using the GRI-Mech 3.0 for a laminar flame at identical operating conditions of this work [44, 50]. The Strouhal number, $St = f_{PVC} d_{nozzle}/u_{x,bulk}$, of the PVC precession was calculated to be 0.87, which closely matched previous investigations of the burner at atmospheric conditions [44]. The experiment was always given a minimum of 10 minutes to stabilize, prior to acquiring measurements. $5\,g/s$ of unheated inlet air was diverted through the particle seeding system, then reintroduced to the inlet plenum. Though the particle seeding was limited to only short bursts during data acquisition, this unheated flow was maintained throughout the entire test by diverting it through a bypass circuit. This process ensured negligible impact on the combustor inlet conditions during data acquisition.

3.2.2 Measurement Systems

Simultaneous measurements of scalar and three-component velocity fields were acquired at a 6 kHz interrogation frequency using combined OH* chemiluminescence (OH*-CL) and stereoscopic particle image velocimetry (SPIV). A schematic representation of the optical measurement system configuration is given in Figure 3.2. The reader is referred to [44] for complete details of each sub-system including resolution considerations. The SPIV and OH*-CL cameras had sufficient on-board memory to acquire 5457 double-frame image pairs and 6826 images per run, respectively. Image system calibrations were performed by imaging a dual-sided, dual-plane dot target (LaVision Type 07). The same target was used for the SPIV and OH*-CL systems, hence spatial alignment of all measurement fields was achieved by mapping to the same coordinate system.

Image processing was undertaken to increase image quality for the PIV algorithm. The minimum intensity over the previous and future five images is subtracted

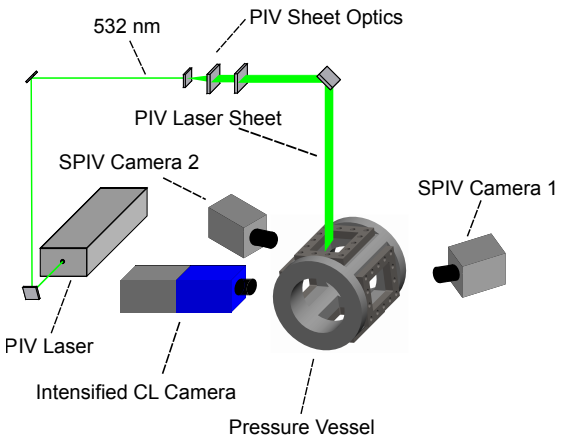

Figure 3.2. Schematic of measurement system.

to remove background noise and decrease glare. A 7x7 pixel sliding window intensity normalization is implemented to reduce any laser sheet intensity variations and sets all particles to comparable intensities. Particle cross-correlations were performed using the multi-pass adaptive window offset cross-correlation algorithm in the LaVision commercial software (DaVis 8.4.0). SPIV results presented in this work were processed using a final window size of 24×24 pixels with 50 % overlap. The corresponding window resolution is $1.25\,mm$ with vector spacing of $0.63\,mm$. A 3×3 sliding window median filter was repeatedly applied three times to remove spurious vectors. The median filter removes velocities outside twice the standard deviation of its neighbors. The removed vectors are replaced with an alternative displacement correlation peak if it is suitable [51]. Vectors were also removed if their correlation peak ratio was less than two. The resulting instantaneous velocity fields had empty spaces where spurious vectors were removed. These locations are filled in by a linear interpolation from their neighbors. An anisotropic denoising filter was applied to better match the interpolated vectors to the flow field [52]. The top two-thirds of the velocity field consistently yielded over 90% first-choice vectors with less than 2% (removed) spurious vectors. Internal reflections and other noise sources caused a

reduction in vector quality near the bottom of the image, so that region was cropped to avoid contamination of the subsequent, quantitative analysis.

Chemiluminescence from electronically-excited hydroxyl (OH*) was imaged using a high-speed CMOS camera coupled to an external two-stage intensifier. An intensifier gate width of $25\,\mu s$ was used for all of the acquired datasets. A 305-315 nm interference filter was placed in-front of the objective lens to isolate the OH*-CL emission. The field of view for the OH*-CL system was approximately $65 \times 80\,mm$ to capture the full spatial extent of the flame zone. White field correction was applied to remove the spatial intensity variations from the detection system [53].

3.3 Deconvolution of Flow Dynamics

Reacting turbulent flows are highly complex due to non-linear coupling of chemistry, turbulence, heat transfer, and acoustics through a vast range of spatiotemporal scales. The interest here lies in the interaction between hydrodynamics and acoustics in a combustor exhibiting sizable pressure oscillations. The amplitude of the thermoacoustics are affected by the hydrodynamics that drive mixing thus reaction rate and heat release. However, these dynamics are perturbed by turbulence in a seemingly stochastic manner. Our method to isolate the large-scale dynamics from the velocity field data is presented below.

Dynamic mode decomposition (DMD) is a parameter-free and data-driven method for understanding complex and high-dimensional datasets. It is in the vein of other lower order dynamics identification algorithms such as POD. DMD is an approximation of the Koopman operator, which characterizes a non-linear system through an infinite dimensional linear operator acting on a set of observables. In practice, the observables are typically the directly measured quantities, such as velocity in this case. An eigendecomposition of the approximated Koopman operator results in a series of modes, each with a growth rate and frequency. DMD generates a linear model of the typically underlying non-linear dynamics. Unlike POD, which associates and ranks

modes based on energy, DMD modes are associated with a unique frequency [54, 55]. For example, the dynamics associated with the thermoacoustic oscillation frequency in this dataset were observed across multiple POD modes [44].

DMD was first applied to non-reacting jets where it identified the spatial structure and frequency of the jet's vortex shedding [56, 57]. DMD has since been extended to the analysis of numerous experimental and numerical efforts in understanding the coupling between hydrodynamics and the resulting thermoacoustics [21, 58–62]. Variants of DMD have been proposed to tackle specific problems such as resolving transient and quasi-periodic dynamics [63]. Methods also exist for debiasing the DMD eigenvalues if the dataset is rank truncated by the most energetic POD modes [64, 65]. The following analysis uses the Exact DMD formulation because of its superior generality [66]. The data does not need to be uniformly sampled in time. Datasets from repeated experiments can be appended to improve accuracy of the modes and frequencies. A brief outline of the DMD implementation is as follows.

The snapshot arrays are formed by flattening the three component, $m \times n$ velocity field at each time step to form z_t as

$$u_x, u_y, u_z \in \mathbb{R}^{mn} \qquad z_t = \begin{bmatrix} u_x(t) \\ u_y(t) \\ u_z(t) \end{bmatrix}.$$

Ordering of the velocity components in z_t is inconsequential as long as the mapping back to the original data structure, $\mathbb{R}^{m \times n}$, is preserved. The data vectors are then concatenated into X and Y arrays as

$$\begin{aligned} X &\triangleq \begin{bmatrix} | & | & & | \\ z_0 & z_1 & \dots & z_{T-1} \\ | & | & & | \end{bmatrix}, \\ Y &\triangleq \begin{bmatrix} | & | & & | \\ z_1 & z_2 & \dots & z_T \\ | & | & & | \end{bmatrix}. \end{aligned} \tag{3.1}$$

The first time step, z_0, is solely within X. Likewise the last time step, z_T, is only contained in Y. A singular value decomposition (SVD) is performed on the X data array, resulting in

$$X = U\Sigma V^*. \tag{3.2}$$

The approximated Koopman operator, $\tilde{A}$, is formed as

$$\tilde{A} \triangleq U^* Y V \Sigma^{-1}. \tag{3.3}$$

This is a matrix multiplication of the previously calculated SVD matrices and the Y data array. Next, an eigendecomposition of the square matrix $\tilde{A}$ results in eigenvectors and eigenvalues, W and λ respectively. Finally, the dynamic modes of the dataset are then defined as

$$\Phi \triangleq Y V \Sigma^{-1} W, \tag{3.4}$$

incorporating the eigenvectors of $\tilde{A}$. The corresponding temporal frequencies (in Hz) for each dynamic mode are the imaginary portion of the scaled eigenvalues

$$f_i = \frac{\mathbb{I}\mathrm{m}\{ln(\lambda_i)\}}{2\pi\Delta t}, \tag{3.5}$$

where Δt is the measurement sampling frequency.

In order to select the suitable DMD modes for construction of a lower order model, the importance of each mode to the original dynamics is needed. Sparse DMD is chosen as the mode selection method for this study, and the following formulation closely follows the original work of Jovanovic et al. [67]. It has been applied to PIV in non-reacting flows to identify coherent structures and their frequencies [68, 69].

A complex amplitude is associated with each DMD mode, which dictates its contribution to the dynamics of the lower order model. The vector of optimal DMD mode amplitude is defined as

$$\alpha = [(W^* W) \odot (\overline{V_{and}\ V_{and}^*})]^{-1}\ \overline{diag(V_{and} X^{\dagger *} W)}, \tag{3.6}$$

where $*$ denotes the complex conjugate transpose, $\odot$ is a element-wise multiplication, $\overline{D}$ is the complex conjugate of matrix D, D^{-1} is the matrix inverse of D, diag(D) forms a vector from the diagonal elements of matrix D, and

$$V_{and} = \begin{bmatrix} 1 & \lambda_0 & \lambda_0^2 & \dots & \lambda_0^T \\ 1 & \lambda_1 & \lambda_1^2 & \dots & \lambda_1^T \\ \dots & \dots & \dots & \dots & \dots \\ 1 & \lambda_n & \lambda_n^2 & \dots & \lambda_n^T \end{bmatrix} \tag{3.7}$$

for an $n-1$ and $T-1$ number of DMD modes and time steps, respectively. Each row of the Vandermonde matrix in equation 3.7 corresponds to a damped or undamped sinusoid governing the temporal evolution of each DMD spatial mode, Φ. Henceforth, these rows are referred to as a temporal mode.

Equation 3.6 was modified from Jovanovic et al. [67] to use the original snapshot array, $X^{\dagger} \triangleq X \cup Y$ (neither the first nor last time step is missing), necessary for Exact DMD. We seek to find an α that minimizes the reconstruction error defined as the Frobenius norm of the difference between the original snapshots and the dynamics from a sparse set of DMD modes

$$J(\alpha) \triangleq \|X^{\dagger} - \Phi D_{\alpha} V_{and}\|_F^2, \tag{3.8}$$

where D_{α} is a diagonal matrix of the previously calculated optimal mode amplitudes.

Applying a penalty to the cardinality of α would reflect the goal of finding sparse modes, but Jovanovic et al. [67] states that the objective function then becomes intractable for large datasets. Therefore, the objective function is defined as

$$\min_{\alpha} \; J(\alpha) + \gamma \sum_{i=1}^{T-1} |\alpha_i|, \tag{3.9}$$

where γ is the penalty multiplier to the sum of absolute values of the optimal mode amplitudes.

A wide range of sparsity multipliers were initially swept to gauge the DMD mode spectrum for the velocity dataset. However, just two sparsity levels are presented to

illustrate the robustness of the modes selected for analysis. Figure 3.3a shows the eigenvalues of the DMD modes on the complex plane with the unit circle depicted as the dotted yellow line. The non-sparse modes (shown by black ∘ symbols) display increased density near the unit circle. Likewise the sparse DMD modes (red and teal ×) are only present near the unit circle. Hence sparse DMD preferentially selects neutrally stable dynamics representing limit-cycle behavior, thereby removing modes representing rapidly decaying turbulent fluctuations.

The amplitude spectrum is shown in Figure 3.3b for sparse and non-sparse modes. Identifying the most important modes in the non-sparse spectrum (shown by the black ∘ symbols) is difficult. The highest amplitude modes have large decay rates, thus their influence on the reduced order model only lasts a short period of time. Red and teal ★ symbols represent sparse DMD modes with γ values of 5000 and 10,000 respectively. Doubling the penalty multiplier from 5000 to 10,000 preserves a few sub 50 Hz modes along with the 455, 1600, and 1704 Hz modes.

Previous POD analysis of the flame revealed the presence of a PVC. The power spectra of these POD temporal modes displayed broadband content centered at 1710 Hz along with a narrow peak around 450 Hz. The thermoacoustic frequency was determined to be 450 Hz from analysis of the OH*-CL and dynamic chamber pressure [44]. Therefore, the 455 Hz DMD mode corresponds to the thermoacoustics, and the 1600 and 1704 Hz modes relate to the PVC.

The DMD mode at 1704 Hz had greater spatial coherence and more easily identifiable centers of rotation compared to the 1600 Hz mode. This leads to setting the sparsity structure to only the 455 and 1704 Hz modes. Figure 3.4 shows the real part of the selected DMD modes for brevity. The 455 Hz mode clearly represents a modulation of the reactant jets and CRB. The pulsating inflow, at the same frequency as the combustor and plenum pressure oscillations, plays a key role in the feedback mechanism resulting in combustion dynamics. Therefore, the 455 Hz DMD mode is referred to as the thermoacoustic mode. Contrastingly, the 1704 Hz mode displays two adjacent counter-rotating vortices corresponding to the PVC dynamics.

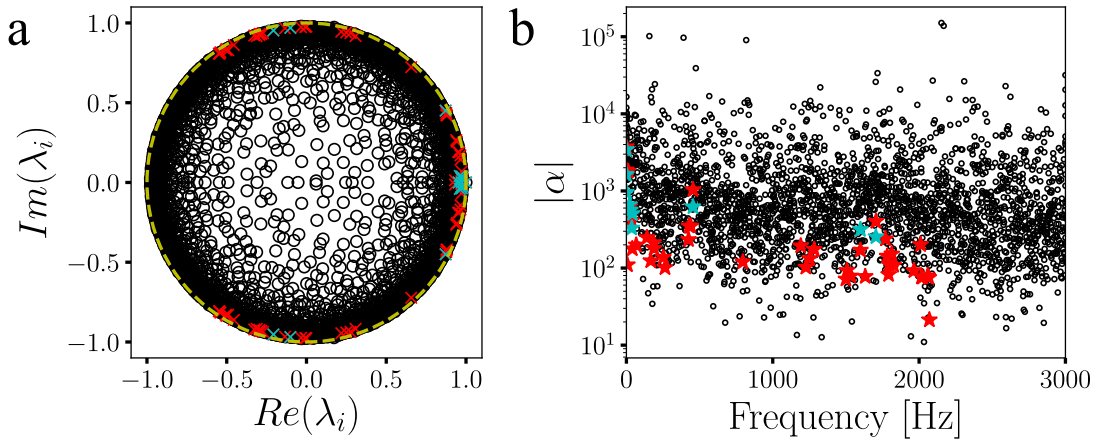

Figure 3.3. Argand diagram of DMD eigenvalues (a) and amplitude spectra (b) for sparse and non-sparse results. Red and teal symbols represent γ values of 5,000 and 10,000 respectively.

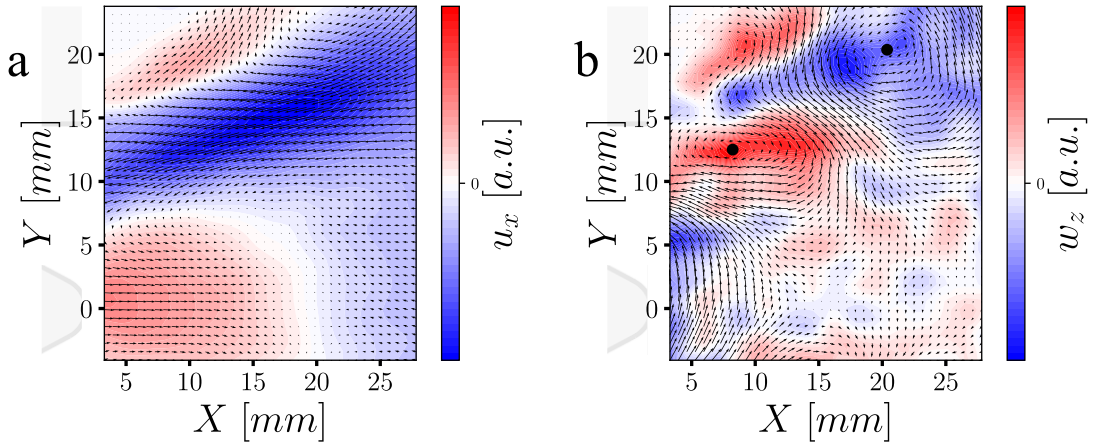

Figure 3.4. (a) Real portion of the 455 Hz DMD mode. Velocity vectors overlaid on filled contours of axial velocity. (b) Real portion of the 1704 Hz DMD mode with the center of the two counter-rotating vortices annotated by •. Velocity vectors overlaid on filled contours of in-plane vorticity. Units in the colorbars are the unscaled DMD spatial mode values.

The time evolution of a simplified flow field from these two DMD modes can now be generated. The optimal amplitudes are recalculated by equation 3.6 for a sparsity structure of just the 455 and 1704 Hz modes associated with the most prominent limit-cycle dynamics. A superposition of the two DMD modes and the mean velocity field by

$$\begin{bmatrix} u_x \\ u_y \\ u_z \end{bmatrix}_{mean} + \left[\Phi D_\alpha V_{and}\right]_{455+1704} \tag{3.10}$$

produces the reconstructed dynamics for further analysis.

Three probe locations in the flow field are selected to demonstrate the effectiveness of the DMD reconstruction in terms of capturing the cyclic oscillations of the underlying data. Figure 3.5 displays the probe points overlaid on the time averaged velocity field. Points labeled P1-3 are located within the reactant jet, the inner shear layer, and CRB respectively. These probe locations coincide with the location of flow structures found in previous studies of the combustor [43]. The line plots in figure 3.5 show the axial velocity for the DMD reconstruction and original dataset over last 200 time steps demonstrating reconstruction accuracy even towards the end of the time sequence. The global trends have been preserved, but the turbulent, aperiodic fluctuations are removed by the reconstructed signal similarly to other work using DMD [70]. The superposition of 1704 and 455 Hz oscillations fits the original data well for P1 and P2. The reconstruction at P3 is dominated by the 455 Hz mode, because the PVC mode does not strongly perturb the inner most part of the CRB. Overall, the DMD reconstruction acts as a bandpass filter over the original data removing the turbulent fluctuations in each of the probe locations, while leaving the high-power dynamics associated with the large-scale structures of interest.

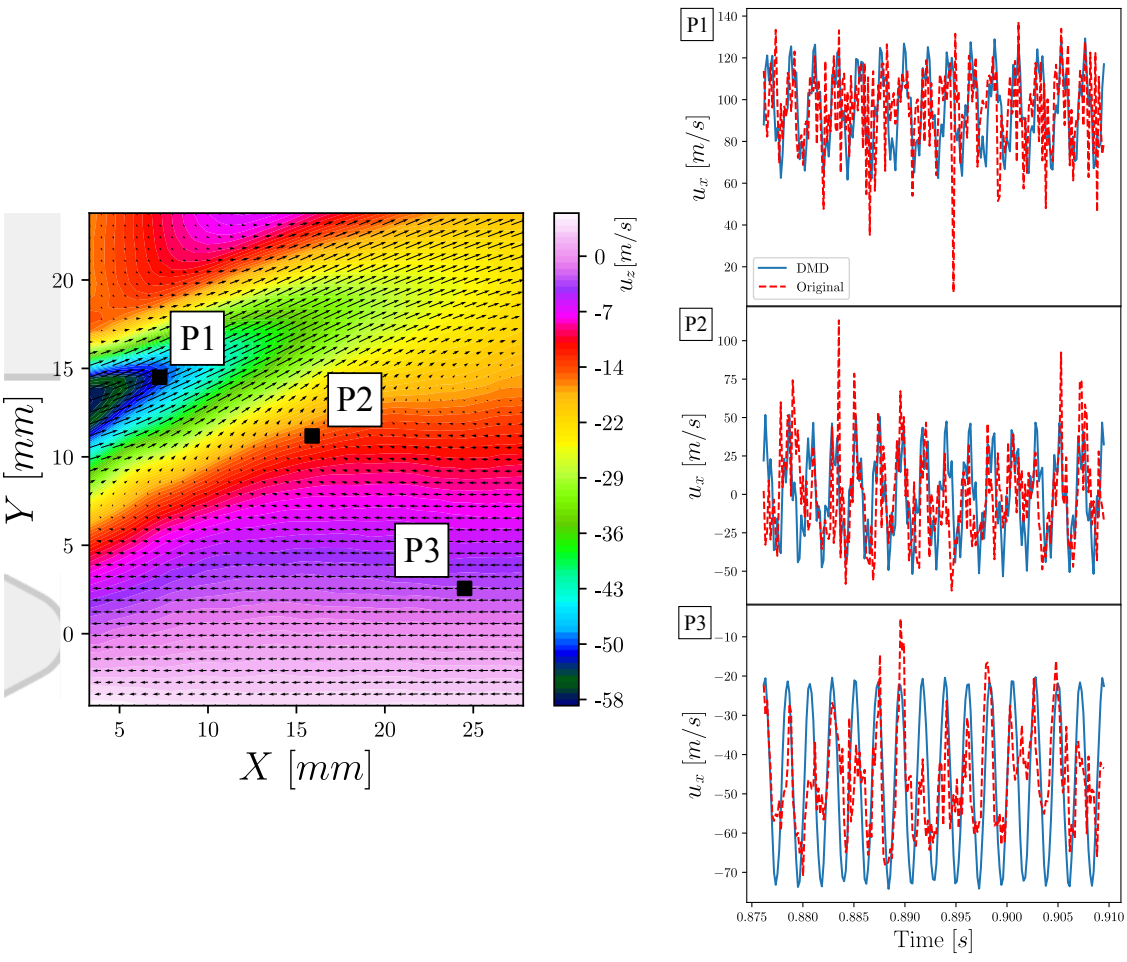

Figure 3.5. Average velocity field with contours of u_z. The DMD reconstruction and the original velocity field is compared at three probe points.

3.4 Phase-Conditioned Statistics

Both 455 and 1704 Hz temporal modes are undamped but stable, and this behavior is previously shown by the time series in figure 3.5. Conditioning simultaneously acquired datasets on the phase of the temporal mode isolates it from other processes, such as turbulent fluctuations. The instantaneous phase for each DMD temporal mode is calculated by taking the argument of the analytic signal derived from a Hilbert transform of the temporal mode [71].

3.4.1 Thermoacoustic Mode

The chamber dynamic pressure and OH*-CL were phase conditioned by the 455 Hz DMD temporal mode representing the thermoacoustic oscillation. The chamber dynamic pressure is band-passed between 450 and 460 Hz with a zero phase shift 2nd order Butterworth filter before phase conditioning. Each measurement is then sorted into 12 bins resulting in a bin width of $\pm 15^{\circ}$ or $\pm \pi/12$. Figure 3.6 shows the phase averages of the OH*-CL images at four equally spaced phase angles. A clear dependence of OH*-CL intensity on the 455 Hz DMD phase signal is observed, which is consistent with the frequency identified in previous analysis of this flame [44]. Intensity throughout the image nearly doubles from $\pi/2$ to $3\pi/2$. The flame shortens axially and shows a slight radial contraction at its base during the minimum intensity. This reinforces the notion that the 455 Hz DMD mode corresponds to the thermoacoustic oscillations. The mean intensity is calculated over the spatial domain for each phase angle to better quantify the OH*-CL signal. Figure 3.7 displays this along with the phase averaged chamber dynamic pressure. A phase lag of $2\pi/3$ between the two signals is present. Similar lags have been reported in studies of atmospheric swirl flames. Lower pressure oscillations corresponded to greater phase lag than conditions with higher pressure oscillations in accordance to Rayleigh's criterion [72].

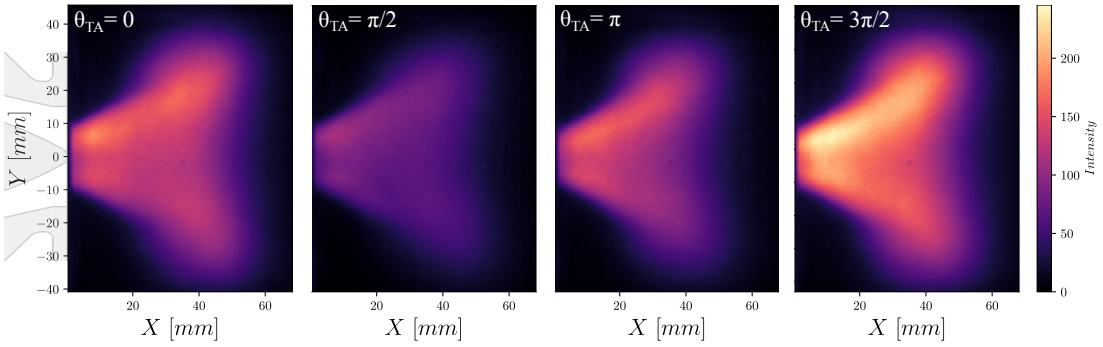

Figure 3.6. Phase average of OH^* chemiluminescence images through the thermoacoustic cycle.

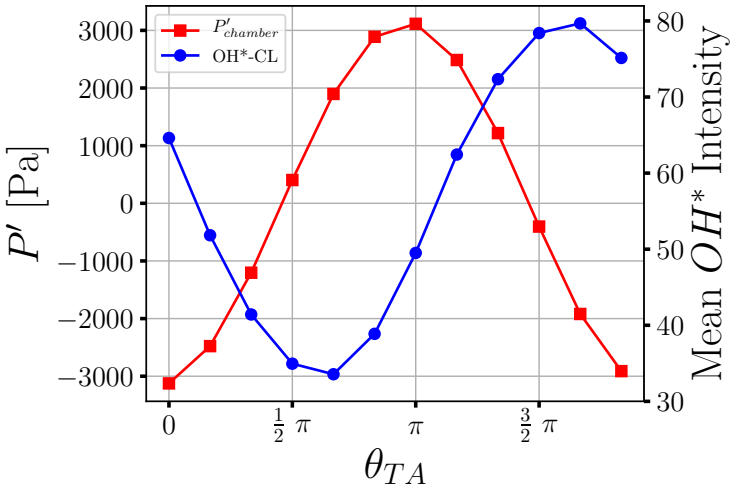

Figure 3.7. Phase average of mean OH^* intensity and chamber dynamic pressure.

3.4.2 3D Structure

Swirl stabilized flames result in highly three-dimensional flow fields, so it is helpful to illustrate the full dimensionality of the most influential flow structures. Two-dimensional representations can be ambiguous. For example, uncertainty in the origin of isolated flame kernels was investigated in the PRECCINSTA burner at atmospheric conditions. Further analysis pinned down the flame kernels to convection from the out-of-plane PVC motion and not auto-ignition [73]. High repetition rate measurements allow for phase locking multiple dynamic processes within one dataset. In contrast to much earlier work where low speed diagnostics were locked to a plenum pressure measurement, and thus were only able to resolve trends with the respect to the frequency locked process [49].

PVCs have been identified in swirling flows by phase averages of 2D SPIV data using the harmonic content of POD temporal coefficients as the phase reference in multiple previous studies. Stohr et al. reconstructed multiple coherent vortex cores from the DLR dual-swirl burner with no thermoacoustic oscillations [74, 75]. Steinberg et al. performed a doubly-phase-resolved analysis on the dual-swirl burner at operating conditions exhibiting thermoacoustic oscillations [72]. The plenum pressure was used to determine the thermoacoustic phase, and the POD temporal coefficient from one mode was used for the PVC phase. The geometry and thermoacoustic coupling between the PVC and flame surface areas was investigated for three different flames. Azimuthal symmetry of the PVC was assumed in all of these studies.

Similar to previous work, the 3D structure of the PVC coupled with thermoacoustic oscillations is generated by a doubly phase conditioned analysis. The phase signal of the 1704 Hz DMD temporal mode is calculated similarly to the 455 Hz phase signal used for conditioning from the previous section. This corresponds to the phase angle (or angular orientation) of the PVC, which exists throughout the thermoacoustic cycle. The DMD reconstructed velocity field is then phase conditioned by both 455 and 1704 Hz DMD phase signals. The PVC and thermoacoustics are separated into

16 and 12 bins respectively. This results in 192 phase bins with roughly 28 velocity fields each that are then averaged. The average velocity field for each phase bin was found to have narrow 3σ confidence intervals leading to the conclusion that the statistic is sufficiently resolved. Further details on the bin number selection is provided in Appendix A. The azimuthal dimension is generated by rotating the PVC phase averaged velocity around the $Y = 0$ axis at regular intervals of 22.5°. The velocity fields are cropped below $Y = 0$, so the rotation does not produce any interference at π intervals. The azimuthal location of the 0° PVC phase is arbitrary, because the thermoacoustic phase has no phase relationship to the PVC orientation.

Figure 3.8 shows three coherent flow structures at all 12 thermoacoustic phase angles. The PVC is defined by an iso-surface at a swirling strength (λ_{ci}) of $8000/s$. This is a user specified threshold chosen to produce the clearest reconstruction. Swirling strength has been used by numerous groups for vortex identification [32, 33, 74, 75] and is defined as the imaginary portion of the complex eigenvalues of the velocity gradient tensor. It is Galilean invariant and ignores shear layers which have large vorticity magnitudes but no spiraling motion. Also swirling strength is extendable to compressible flows, which is not the case for other popular methods such as Q and λ_2 criteria [76]. Nevertheless, the authors would like to note that the visualizations with Q criteria does produce similar results as λ_{ci}. Iso-surfaces of $u_x = 0\ m/s$ and $u_x = 80\ m/s$ represent the boundary of the CRB and a swirling reactant jet, respectively. The $u_x = 80\ m/s$ threshold is empirically determined by the axial velocity magnitude that encompasses most of the reactant jet in the mean velocity field. Contours of $u_x = 0\ m/s$ have been used to demarcate the CRZ in previous studies on GTMCs, so this work follows that convention [44, 72, 74].

The minimum axial extent of the PVC occurs at $\theta_{TA} = \pi/3$ and grows into a coherent helical shape by $\theta_{TA} = \pi$. The PVC is bound by the CRB and jet in-flow throughout the measurement domain. This is clearly shown from $\theta_{TA} = \pi$ to $3\pi/2$, and alludes to the role of the PVC in transporting hot gases from the CRB into the reactant jets to sustain combustion. The CRB is highly asymmetric and contracted

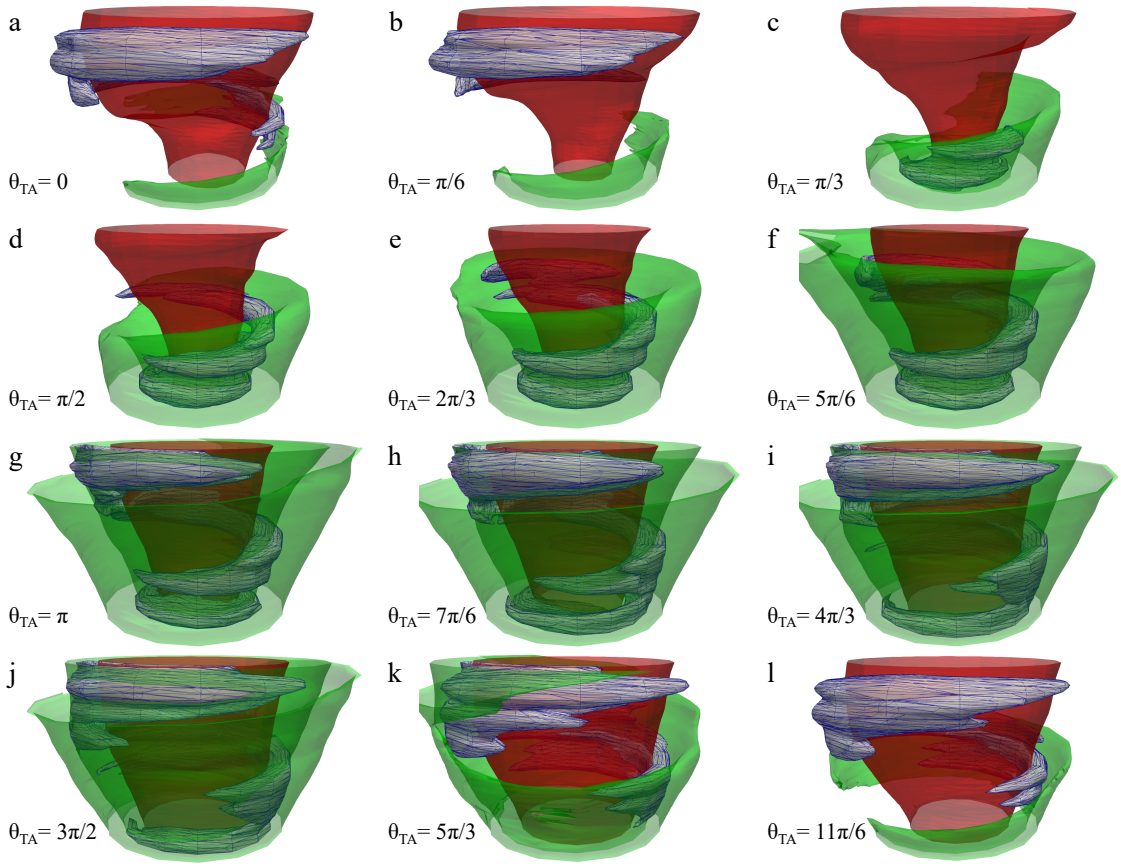

Figure 3.8. Flow structure evolution through the thermoacoustic cycle. The red and green iso-surfaces are $u_x = 0\ m/s$ and $u_x = 80\ m/s$, respectively. The gray and outlined iso-surface corresponds to the PVC defined as $\lambda_{ci} = 8000/s$.

at the base from $\theta_{TA} = 0$ to $\pi/3$ when the reactant jets and PVC are weak, thus no longer confining the CRB. However, the jets and PVC then increase in strength and spatial extent, thereby molding the CRB into a more symmetric shape. The CRB undergoes radial expansion beginning at $\theta_{TA} = \pi/2$, thereby pushing the PVC and jets outward. Eventually the jets rapidly decay near $\theta_{TA} = 3\pi/2$ and the PVC along with it. The thermoacoustic cycle then restarts with a large CRB unimpeded by a strong reactant jets.

Figure 3.9 displays a 2D slice of the reconstructed 3D flow structures from figure 3.8 overlaid on the phase averaged OH*-CL. The 2D slice represents a fixed phase angle, thus spatial orientation, for the PVC. OH*-CL is a path integrated measurement, so any spatial relationship with the 2D contours is not exact. However, this figure further illustrates that the PVC is spatially confined between the reactant jets and the CRB. As expected for a reacting shear layer, the reactant jets typically border the edge of heat release. The expansion and contraction of the CRB is greater than any change in the OH*-CL topology. However, the OH*-CL intensity is highly correlated to size of the CRB. For example, the CRB is shown to be contracted from $\theta_{TA} = 0$ to π coinciding to the lowest OH*-CL intensity distributions.

The evolution of these structures can be more quantitatively described by figure 3.10 showing the volume enclosed by each iso-surface with respect to the thermoacoustic phase angle. The volume of the PVC and jets closely track each other with a small phase shift around one phase bin spacing. The CRB and jet volumes have a much larger phase shift. The jet volume is maximum at $\theta_{TA} = \pi$, while the CRB grows to a maximum at $\theta_{TA} = 11\pi/6$. At this phase, the jet volume has decreased dramatically, and the PVC volume is begins to reduce. However, the CRB is now unconstrained and reaches the maximum volume. The described sequence matches the visualization of figure 3.8.

The CRB is a source of hot gas that acts to assist ignition and stabilize the high-power swirl flame. Recirculated combustion products are transported into the reactant jets through the shear layer between the two structures. The volumetric flow rate ($\dot{Q}$) through the CRB surface is calculated at each face of the interpolated zero axial velocity iso-surface by a dot product of velocity and the area vector. $\dot{Q}$ out of the CRB is then equal to the sum over the entire iso-surface, and it is plotted against the thermoacoustic phase angle in figure 3.11. Values are positive throughout the thermoacoustic cycle indicating a net flow out of the CRB, which is fed by entrainment due to vortex breakdown downstream of the field of view. This is expected, because the role of the CRB is to transport combusted hot gases back to the reactant jets

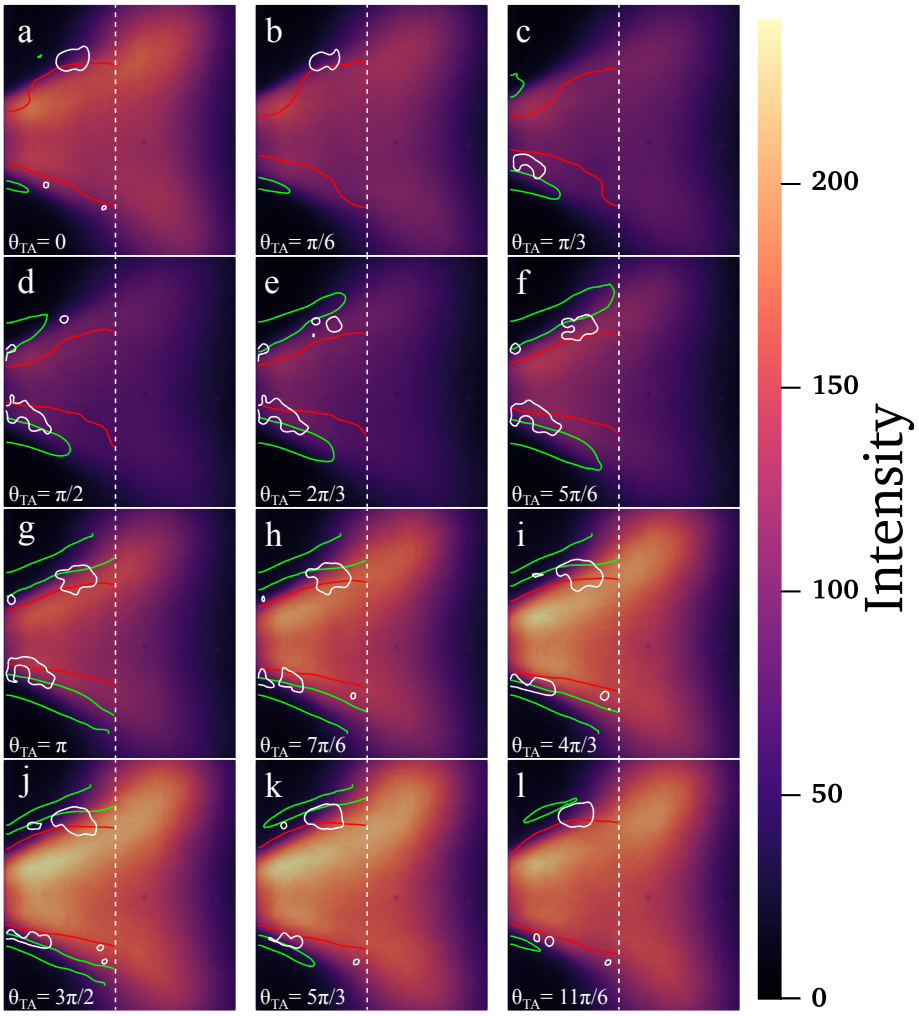

Figure 3.9. Overlaid 2D slices of the flow structures and the OH*-CL intensity distribution over the thermoacoustic cycle. The red and green contours are $u_x = 0\ m/s$ and $u_x = 80\ m/s$, respectively. The white contours corresponds to the PVC defined as $\lambda_{ci} = 8000/s$. Dotted white lines denote the maximum axial extent of the velocity measurements.

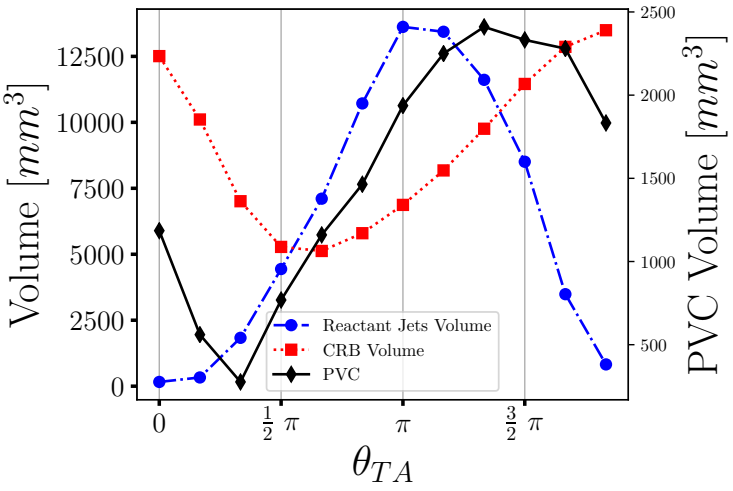

Figure 3.10. Volume of reactant jets, CRB, and PVC with θ_{TA} phase angle.

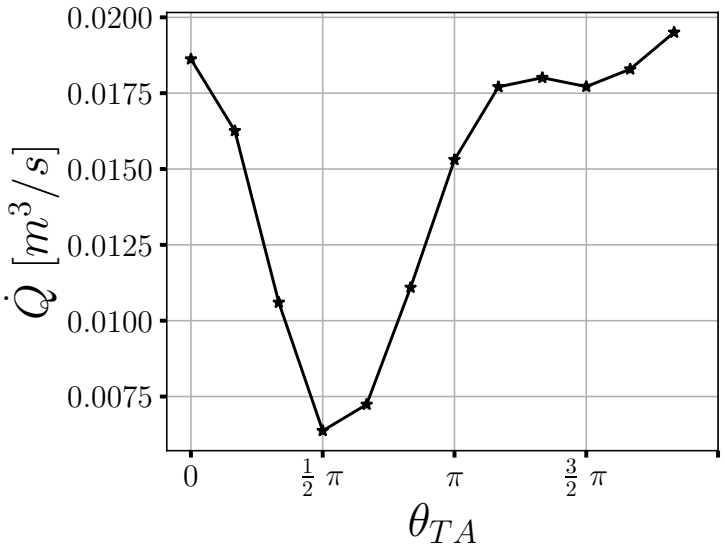

Figure 3.11. Volumetric flow rate out of the CRB throughout the thermoacoustic cycle.

to maintain ignition. Variation through the thermoacoustic cycle is similar between the CRB volume and $\dot{Q}$, but $\dot{Q}$ stays near its largest magnitudes even when the CRB volume is reduced from its maximum. This is illustrated from $\theta_{TA} = 7\pi/6$ to $3\pi/2$. This indicates transport out of the CRB is significant even at the phases where the CRB is still undergoing expansion to a maximum. Consequentially, the inflow into the CRB was observed to increase at these phase angles. The lowest $\dot{Q}$ is at $\pi/2$, which is near the minimum CRB volume and mean OH*-CL intensity. The maximum $\dot{Q}$ and OH*-CL intensity also coincide at nearly the same thermoacoustic phase. This can be attributed to a few causes. At around $\theta_{TA} = \pi/2$, the reactant jet volume is increasing but still low. Reduced reactant inflow along with low outflow from the CRB causes the observed minimal heat release. Moreover, the reduced flow of hot gases from the CRB into the reacting shear layer results in less reactant preheating. This phenomena can also cause a decrease in flame speed and reaction rate [**?**], thereby also resulting in lower heat release at this point in the thermoacoustic cycle.

3.5 CRB and PVC Coupling

The PVC influences combustion by generating flame roll-up events that rapidly mix burned and unburned gas to increase reaction rates as shown by previous studies with simultaneous SPIV and OH-PLIF measurements [74]. Regions of large swirling strength on the CRB surface gives an indication of contact with the PVC, thus greater transport between the recirculated hot product gas and fresh reactants. The CRB definition as the $u_x = 0\ m/s$ surface is physically robust, because that is the interface where recirculated gas with negative u_x meets the reactant inflow with positive u_x. Again, the PVC does not have a strict definition, and a criteria based on visualization was used in figures 3.8 and 3.10. Nevertheless, figure 3.12 shows the CRB surface area with $\lambda_{ci} \geq 8000/s$, which was the threshold used to identify the PVC previously. This provides a sense of how much of the CRB surface is impacted by intense vortical flow. Figures 3.14 and 3.13 illustrate the unthresholded distribution of λ_{ci} on the CRB; thereby, reinforcing the quantitative analysis of the interaction between the CRB and PVC. Figure 3.13 displays the surface area weighted PDF of λ_{ci} on the CRB for four equally spaced phases through the thermoacoustic cycle. Figure 3.14 shows the surface of the CRB colored by λ_{ci} with translucent lower magnitudes to display the helical structure especially for $\theta_{TA} = \pi/2$. The view is rotated by approximately 180° from figure 3.8 to provide another view of the reconstructed PVC and CRB.

The PVC and CRB coupling is weakest near $\theta_{TA} = \pi/2$. The minimum area of λ_{ci} on the CRB shown in figure 3.12 occurs at $\theta_{TA} = \pi/3$ and corresponds to the minimum PVC volume in figure 3.10. The CRB is observed to be heavily contracted and the PVC just starting to grow at $\theta_{TA} = \pi/2$ in figure 3.14b. This is also when the mean OH*-CL intensity figure 3.7) and CRB $\dot{Q}$ (figure 3.11) are nearing or at their minimums. This suggests that when the PVC is weakly interacting with the CRB, then transport of hot gas out of the CRB decreases and heat release is, correspondingly, reduced.

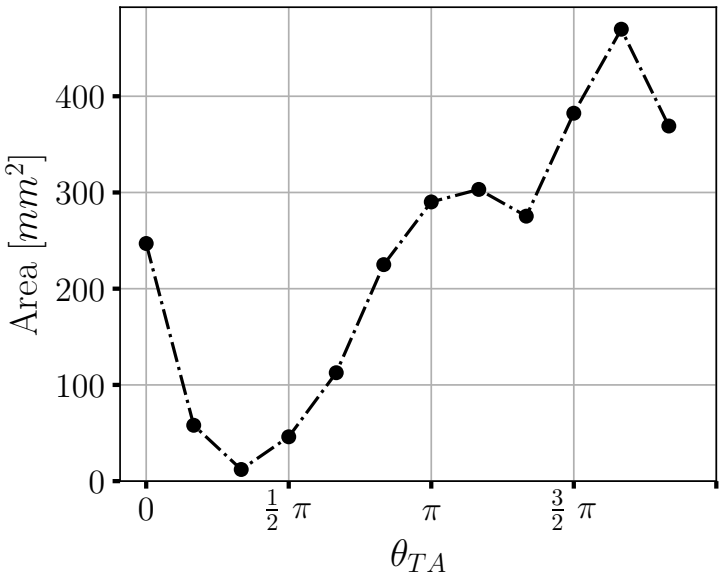

Figure 3.12. CRB surface area with $\lambda_{ci} \geq 8000/s$.

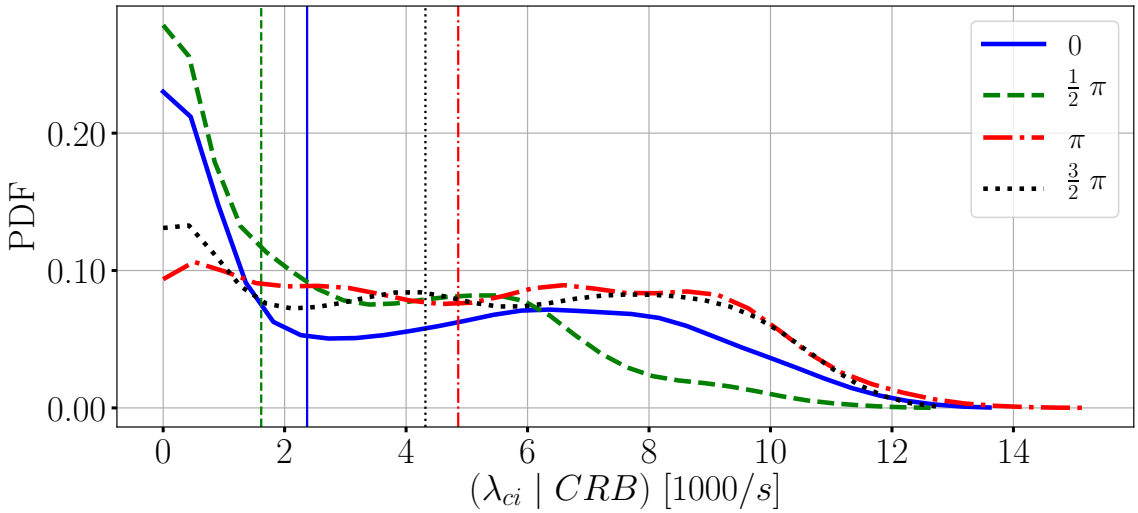

Figure 3.13. PDF of swirling strength on the CRB surface. Median values are shown by vertical lines.

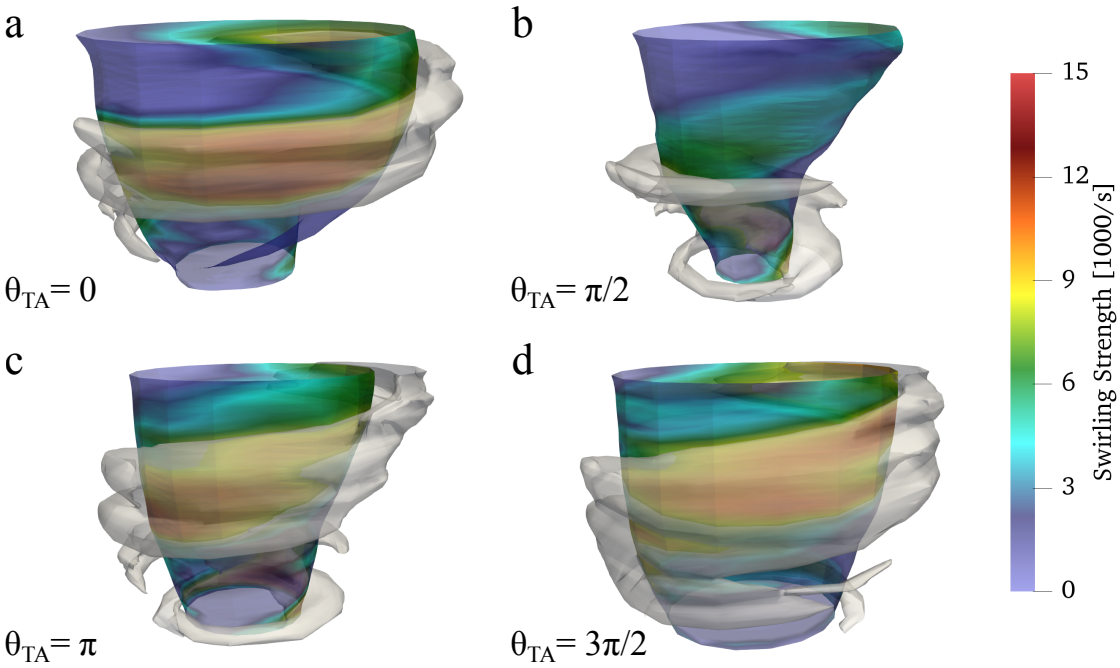

Figure 3.14. Surface of the PVC and CRB colored by λ_{ci} at four phase angles of the TA cycle.

Moving to $\theta_{TA} = \pi$ and $3\pi/2$, the peak in the distribution at zero swirling strength (figure 3.13) is less prominent. A more uniform distribution also appears from λ_{ci} = 2000/s to 9000/s; a sign that the rotation within the PVC has increased. Values of $\lambda_{ci} \geq$ 12,000/s are most abundant at $\theta_{TA} = 3\pi/2$. The PVC enhances mixing but could also produce significant local quenching at the operating condition investigated in this work. Findings in the DLR dual-swirl burner (DSB) at low Damköhler numbers reported that the PVC induced high enough flame stretch rates to cause local quenching of flame kernels and delaying heat release [77]. The manner of premixing in the DSB is different than the PRECCINSTA burner, so the sensitivity of local quenching to flame stretch rates could be altered. However, the flames of the DSB has been noted to operate in a premixed manner, so the comparison is reasonable [78]. This mechanism could be attributing to lower heat release at $\theta_{TA} = \pi$ than $3\pi/2$ because the median λ_{ci} at $\theta_{TA} = \pi$ is greater than the median at $3\pi/2$. In addition, the surface area of large λ_{ci} values on the CRB is much larger at $\theta_{TA} = 3\pi/2$ than π. This is demonstrated visually in figure 3.14c-d by the radial expansion of the CRB volume with the PVC maintaining its helical structure. Therefore, the PVC and CRB intersection and coupling is near maximum at $\theta_{TA} = 3\pi/2$, which corresponds to the second highest mean OH*-CL intensity.

Starting the cycle again at $\theta_{TA} = 0$, the PVC begins to wane as shown by a reduced intersection with the CRB near its root in figure 3.14a. The peak at 0 λ_{ci} has reappeared in the distribution of figure 3.13, but $\lambda_{ci} \geq 6000/s$ values are still present in high quantities. These larger λ_{ci} values correspond to the presence of the PVC at the top half of the CRB as shown in figure 3.14a. Looking back to figure 3.7, this corresponds to an intermediate value in the global heat release indicated by OH* chemiluminescence.

As the structure of the PVC and CRB is modulated due to the combustor pressure oscillations, mixing between the reactants and recirculated product gas is affected. When the CRB expands radially, its surface area increases. The PVC is constrained between the reactant jets and the CRB such that the contact between the CRB and

PVC is increased. Under these conditions, mixing between the recirculated products and incoming reactants is enhanced, modulating heat release. As the cycle progresses, the CRB, PVC, and reactant jets are reduced in size and strength, thereby reducing the interaction of these structures within the confined volume of the combustor. Less intersection between the CRB and PVC causes a reduction in transport through the reaction zone, continuing the cycle. The dynamics of the PVC are not a direct cause of the instability. The precession frequency of the PVC is 1704 Hz, which does not correspond to the frequency of the thermoacoustic instability at 455 Hz or an under/overtone of that frequency. Nevertheless, the PVC and CRB coupling demonstrates that the presence of the PVC is an important factor in driving and sustaining combustion instability, even at elevated pressure and power conditions when the time-scale of the PVC precession is a factor of 2-3 shorter than in previous investigations of this burner.

3.6 Conclusions

Simultaneous 6 kHz SPIV, OH*-CL, and 100 kHz pressure measurements were acquired in the PRECCINSTA GTMC at elevated pressure and temperature to emulate more engine-realistic conditions. Sparse DMD was performed on the measured velocity fields and successfully identified the thermoacoustic (455 Hz) and PVC (1704 Hz) modes as dominant. Both frequencies were similar to those identified in previous work of analysis upon POD results. Reconstructing the velocity time series with the mean velocity and the two DMD modes reasonably matched the temporal evolution to the raw SPIV results. However, the incoherent turbulent fluctuations were removed resulting in velocity field reconstruction that contained only the principal dynamic content. Phase conditioning the OH*-CL and dynamic chamber pressure on the thermoacoustic DMD temporal mode resulted in an expected sinusoidal modulation that agreed with previous analysis of this dataset.

A three dimensional reconstruction of the flow field was created by double phase conditioning off the two DMD temporal modes. The reactant jets, PVC, and CRB were tracked throughout the thermoacoustic cycle. The CRB displayed large asymmetric distortions when the PVC and jets were decayed. However, the CRB was molded into a symmetric structure when the PVC and jets gained strength to spatially constrain the CRB. Tying together multiple derived quantities and statistics from the phase conditioned results, it was found that lower levels of heat release generally coincided with reduced interaction between the PVC and CRB. Likewise the thermoacoustic phases with the highest amount of intersection between the PVC and CRB displayed the largest levels of heat release. This was also accompanied by a swelling of the CRB and an increase in volumetric flow rate out of the CRB.

This work has shown that the presence of a PVC between the CRB and the reactant jets remains a key factor in the sustainment of thermoacoustic oscillations at elevated pressure and power for this flame. Despite very different characteristic hydrodynamic time-scales, compared to low power conditions, the rapid mixing induced by the PVC remains a significant mechanism for combustion dynamics in this configuration.

4. INTERMITTENT LIFTOFF OF A THERMOACOUSTICALLY UNSTABLE SWIRL FLAME AT ELEVATED POWER DENSITY

4.1 Introduction

In Chapter 3, the limit cycle behavior of a thermoacoustically unstable swirl flame at elevated power density was analyzed using double phase conditioning of the TA and PVC DMD modes. These DMD modes extracted from the time series of velocity fields did not correspond to transient events, because the growth rates indicated neutral stability. We now turn our attention to aperiodic or intermittent events that may be difficult to investigate with DMD, but still of major importance to characterizing combustor performance. A cursory examination through the time series of either OH*-CL or OH-PLIF datasets reveals dramatic occurrences of flame lift-off at irregular intervals. During these lift-off events, the flame does not exhibit any tendency towards total extinction based on the wide field of view afforded by the OH*-CL images.

Intermittent flame liftoff has been known to occur at atmospheric conditions in the PRECCINSTA combustor. SPIV and OH-PLIF measurements were made at a bistable operating condition, which demonstrated that the transient formation of a PVC induced flame liftoff [45]. The PVC was shown to form at the onset of flame liftoff through instantaneous flow field snapshots and a flow asymmetry measure near the combustor inlet. An inflow increase of unburned reactants is observed to precede the formation of a PVC, and this repeats at $\approx$ 10 ms intervals when the flame is attached. However, not every instance of the PVC leads to a flame lift-off. Thermometry of the central conical bluff body was performed at 1 kHz [79]. The results illustrated that the temperature slowly rises when the flame is attached and rapidly

drops by about 50 K during lift-off. The bluff body temperature also has oscillations at the same frequency as the PVC when the flame is lifted. In another study, spectral proper orthogonal decomposition and linear stability analysis was used to analyze the velocity field of one transition to flame lift-off [80]. An outline of events from flame liftoff back to reattachment is provided. Slow drifts of the inflow conditions enables a sufficiently strong perturbation from the turbulent flow to initiate a PVC. The flame lifts off and a new flame root is established downstream. The combustor also becomes thermoacoustically unstable. This causes the formation of symmetric vortices stemming from the inlet, which then reduces the strength of the PVC. Periodic flame reattachment and liftoff is observed preceding sustained anchoring to the conical bluff body. Finally, suppression of the TA instability occurs shortly afterwards.

Strain rate and flame extinction lengths at a bistable condition were analyzed in the PRECCINSTA combustor with larger dimensions and no exhaust contraction [82]. The ratio of time averaged strain rate at the inlet and extinction strain rate linearly correlated to the average flame extinction length and lift-off probability. The time averaged strain rate by itself did show the same trends. Multiple operating conditions of varying fuel compositions and equivalence ratios were also investigated. Flame lift-off was found to be more probable at higher bulk velocities in most cases.

Imperfect premixing of fuel and air in the PRECCINSTA combustor has also shown intermittent flame lift-off at atmospheric conditions [81]. The attached flame demonstrated thermoacoustic instability while the lifted flame had lower amplitude oscillations. An increase in backflow within the CRB is observed prior to flame reattachment, but the cause of lift-off was not apparent.

The presence of a bistable flame is not unique to the PRECCINSTA combustor and similar behaviors have been reported in various other swirl flames. Acoustic forcing of a swirl flame was investigated with OH-PLIF phase locked to the instability frequency [83]. High amplitude forcing resulted in the flame undergoing a lift-off and reattachment process depending on the TA phase. However, results indicated a non-monotonic relation between the severity of the flame root movement and forcing

amplitude. All of the preceding literature has been on gaseous fuels, but spray flames can also show aperiodic lift-off and reattachment. A swirl flame combusting heptane illustrated this behavior while investigating flame response near LBO [84].

LES has been routinely applied to study gas turbine combustors at operating conditions where high resolution measurements are exceedingly difficult to acquire. The capability of LES and modern combustion models has been demonstrated to resolve even transient events such as local flame extinction and lift-off. Simulations of a piloted swirl burner illustrated that either a lifted or attached flame could exist at the same operating condition [85]. Flame liftoff was triggered by a sudden change in operating condition. Gradual changes resulted in the flame staying attached and lacking a PVC. Both flame types also had different responses to acoustic forcing of the inlet air supply. The lifted flame transitions to an attached state in the presence of high amplitude forcing, but none of the forcing amplitudes could lift-off the attached flame. The accuracy of LES applied to non-premixed gaseous and spray swirl flames in these regimes has been demonstrated by a reasonable agreement in flame lift-off height statistics to OH-PLIF measurements [86, 87].

The work presented in this chapter expands upon the previous PRECCINSTA investigations at atmospheric conditions for a bistable flame with imperfect premixing [81]. The swirl flame is operated at elevated temperature, pressure, and Reynolds number with a greater number of lift-off events being recorded. A multifaceted analysis is performed to illustrate the characteristics of both lifted and attached flames as well as transitions between the two. Furthermore, semantic segmentation of OH-PLIF images is demonstrated to enable quantitative analysis even in the limit of low SNR images found at high pressure operation or with low laser pulse energies.

4.2 Experiment Configuration

The experimental configuration is identical to Chapter 3.2 with Flame B being the studied. Therefore, most experimental details are not repeated and only

an additional description of the OH-PLIF system is provided. The OH-PLIF measurements were performed simultaneous to the SPIV and OH*-CL. Figure 4.1 illustrates the measurement systems with the additional OH-PLIF assembly. The laser system consisted of a frequency-doubled dye laser (Sirah Cobra-Stretch HRR) pumped by a Q-switched, diode-pumped, solid-state Nd:YLF pump laser (Edgewave IS811-E). Using Rhodamine 590 dye (in ethanol), the $566.4\,nm$ fundamental wavelength was frequency-doubled to $283.2\,nm$ to excite the $Q_1\,(7)$ line of the $A\ ^2\Sigma^+(v'=1) \leftarrow X\ ^2\Pi(v''=0)$ transition of OH. The average laser pulse energy at $283.2\,nm$ was $0.25\,mJ/pulse$ at a 3 kHz repetition rate. The PLIF excitation sheet was formed using two cylindrical lenses ($f_{PLIF,1} = -50mm$, $f_{PLIF,2} = 150mm$) in a cylindrical telescope arrangement, resulting in a collimated sheet height of approximately $20\,mm$. A third cylindrical lens ($f_{PLIF,3} = 750mm$) was used to focus the sheet to the beam waist ($\approx 400\mu m$ FWHM) at the combustor centerline. The 283 nm OH-PLIF laser pulse was delayed from the first 532 nm PIV pulse by $\Delta t/2$ (1.5 μs)

The fluorescence signal was collected using a $64\,mm$ focal length, f/2.0 objective lens (Halle). A two-stage, lens-coupled intensifier (LaVision HS-IRO) was used to amplify the signal, which was imaged by a high-speed CMOS camera (LaVision HSS6). The intensifier gate width was run at the minimum value possible (100 ns) to minimize background noise from flame luminosity. An optical band-pass filter isolated the fluorescence signal from the $A\ ^2\Sigma^+(v'=1) \rightarrow X\ ^2\Pi(v''=1)$ and $A\ ^2\Sigma^+(v'=0) \rightarrow X\ ^2\Pi(v''=0)$ bands occurring over the $305-315\,nm$ range of wavelengths.

Figure 4.2 displays an overlay of a instantaneous snapshot of all three camera based measurements. The spatial extent of the OH*-CL and SPIV are identical to Chapter 3.2. The OH-PLIF laser sheet is placed a few millimeters from the burner face and intersects a portion of the SPIV domain. The reactant jets, CRB, and multiple shear layers are visible within the interrogation region. A white-field dataset

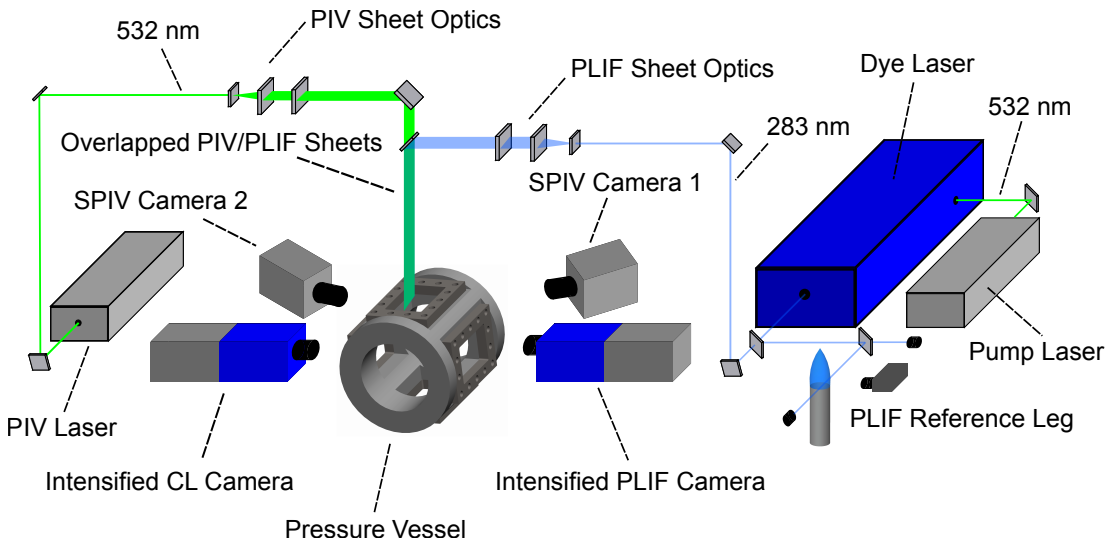

Figure 4.1. Schematic of laser diagnostic measurement systems.

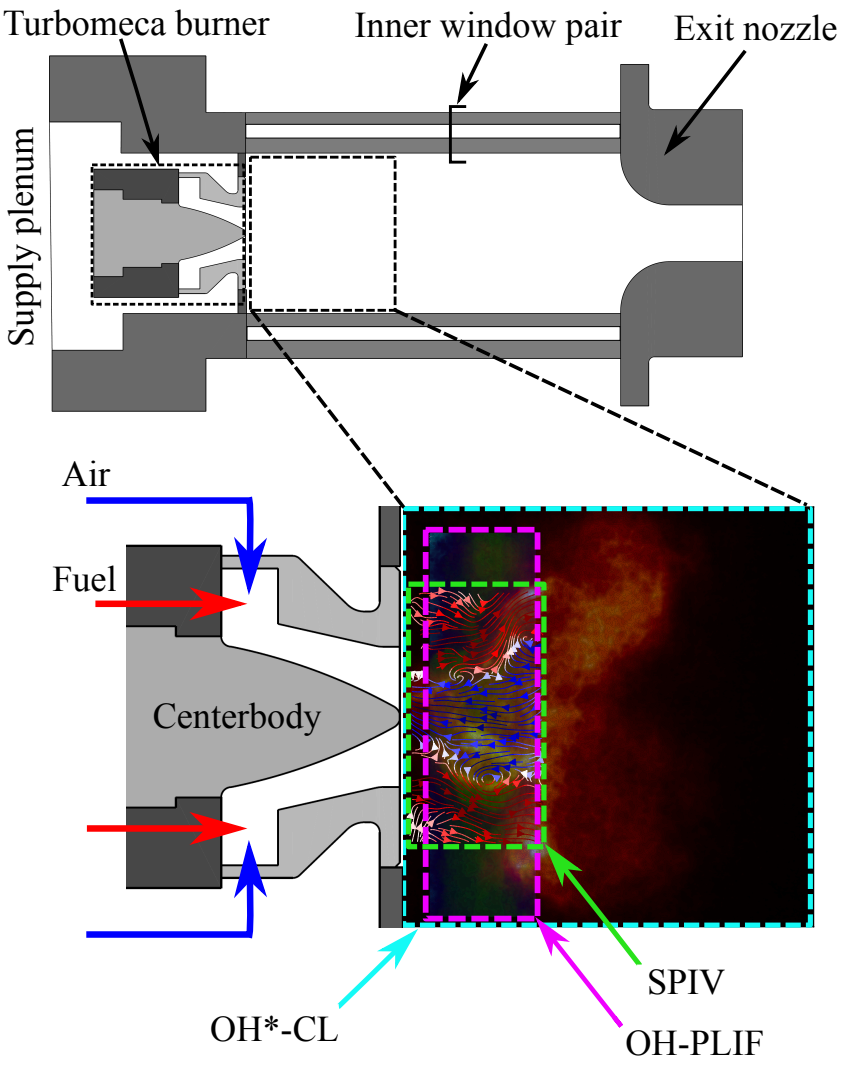

Figure 4.2. Schematic showing the spatial interrogation domain for each diagnostic.

consisting of a homogeneously lit target was also collected for intensity normalization purposes.

4.3 Semantic Segmentation of OH-PLIF

The OH-PLIF images displayed multiple processing challenges. Reduced SNR at the lower portion of the images is evidence of absorption of the laser sheet. This is a well known trait of OH-PLIF imaging at elevated pressure and has a stronger

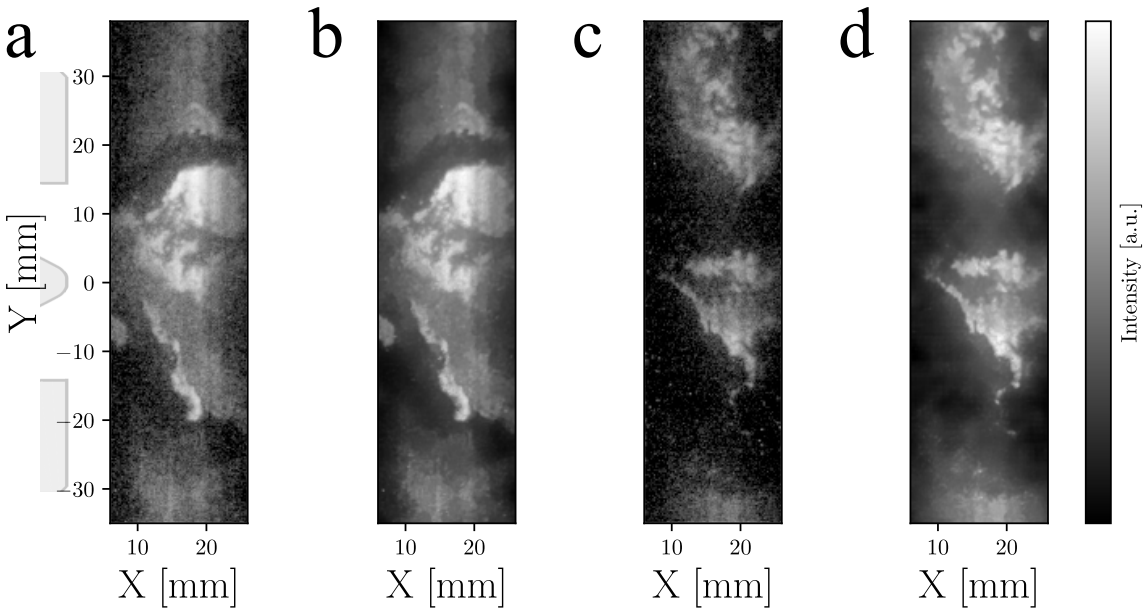

Figure 4.3. Before and after applying non-local means denoising to OH-PLIF images (a and b) attached flame (c and d) lifted flame

effect as pressure increases [19, 88]. Sheet intensity variations are also present due to non-uniform laser output and can change for every laser pulse. Techniques to correct this can involve calibration using images of homogeneous acetone vapors and direct measurement of shot-to-shot spatial intensity distributions [18, 89–91].

Correction of laser sheet intensity variations through frequency domain filtering proved futile in this dataset, because it introduced low spatial frequency artifacts in regions originally without striations. Ultimately, only the removal of Gaussian and impulse noise was successful. Figure 4.3a,c shows a pair of images corresponding to attached and lifted flames. White field correction was performed akin to the OH*-CL images. Images were log-scaled to enhance contrast. Non-local means denoising was then performed (fig. 4.3b,d) and dramatically reduced the Gaussian noise evident in the reactant jets [92, 93]. Importantly, the denoising preserved edges to maintain the morphology of the OH structures.

Quantitative analysis of the OH-PLIF images typically involves edge extraction. Multiple techniques varying in complexity from a simple threshold to multi-step algorithms were evaluated, but none produced satisfactory results across the entire dataset [18, 94–97]. Classical segmentation methods were also evaluated and found lacking [98, 99]. Tuning specific parameters such as a gradient threshold could give marginally acceptable results compared to a human expert in turbulent swirl flames. However, the deep range of spatial scales characteristic of high Reynolds number flows combined with sheet intensity spatial variation and absorption proved too much for any of the evaluated methods.

Recent advancements in deep learning arguably stem from the dominating performance of AlexNet compared to classical techniques relying on hand-crafted feature engineering in the ImageNet classification competition [100]. Thus, convolutional neural networks (CNN) provide another avenue for analysis of the OH-PLIF images. The ultimate goal is to automate edge extraction or semantic segmentation at the level of a subject matter expert. Edge extraction with CNNs has been demonstrated in color images with complex scenes [101,102]. Semantic segmentation is chosen instead, because it provides area and centroid measures in addition to edges. The semantic aspect points to the unique capability of automatically classifying segments based on the flow structures. Based on human labels provided in the training set, the CNN learns which portions of the image correspond to the CRB or upper OSL. The lower OSL is ignored in this analysis due to low SNR resulting in too much ambiguity in segmentation.

DeepLabv3+ is a state-of-the-art architecture for semantic segmentation and recently demonstrated the highest performance in the PASCAL VOC 2012 project [102]. A ResNet-101 image classification network is used as the backbone of the DeepLabv3+ architecture for results presented in this work [103]. The dataset for the PASCAL VOC competition contains images of everyday objects and scenes with no relation to OH-PLIF images [104]. Nevertheless, transfer learning has been shown to be successful applied to vastly differing datasets [105–107]. Parameters of a pre-trained CNN

on the segmentation task from the PASCAL VOC 2012 project are used as an initialization for fine-tuning on the OH-PLIF images. Details on the training methodology including examples of expert labeled ground truths are provided in Appendix B.

Representative outputs of the CNN for OH-PLIF images during attached and lifted flames are shown in figure 4.4a and b, respectively. Segments colored in blue and green correspond to the CRB and upper OSL classes, respectively. The lower OSL is successfully ignored. Simply cropping the lower portion of the images would be a poor choice, because the CRB displays a wide range of vertical motion. Notably, the highly wrinkled edges of the OH segments and small pockets are well captured.

Figure 4.5a,c display the direct output of the CNN where segments of the CRB and upper OSL are mixed. Post-processing in the form of region merging is required, so that resulting morphological measures are accurate. A rules based methodology is implemented where the largest upper OSL segment is checked for adjacent CRB segments. These regions are merged into the upper OSL class if the CRB segment does not correspond to the largest segment by area in the image. This can be seen by the region circled in red in figure 4.5a. The same steps are then applied to the largest CRB segment. Next, any remaining small regions with adjacent classes are merged to whichever class has the largest area. A pocket of OH circled in red in figure 4.5c initially has both class labels and subsequently merged as seen in figure 4.5d. A final step of removing any isolated segments less than 10 pixels [108]. Likewise, any segment with a hole that is smaller than this threshold is closed.

Certain images display ambiguity in semantic segmentation when the CRB and OSL structures are connected. Figure 4.5b shows a region circled in red where a delineation between the two classes is not well defined even for a subject matter expert. Figure 4.5d shows a region circled in red is not segmented. It appears to possibly be connected to the main CRB body. However, the limited axial extent of the images makes classification difficult. It is also located where the lower OSL typically resides, so there is insufficient context in the image to give a high confidence for semantic segmentation. In addition, there are two isolated segments within the red

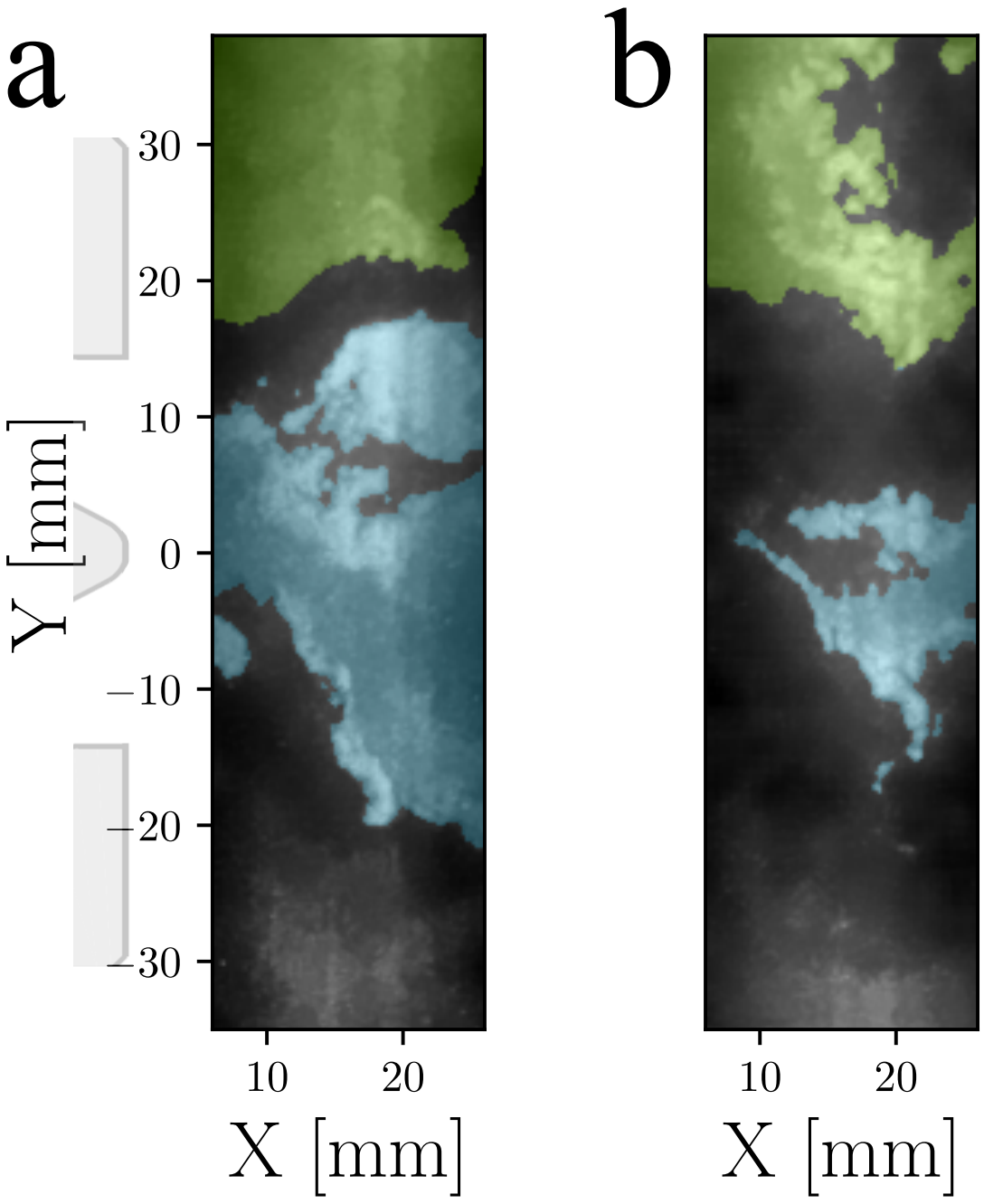

Figure 4.4. Semantic segmentation of OH-PLIF images (a) attached flame (b) lifted flame.

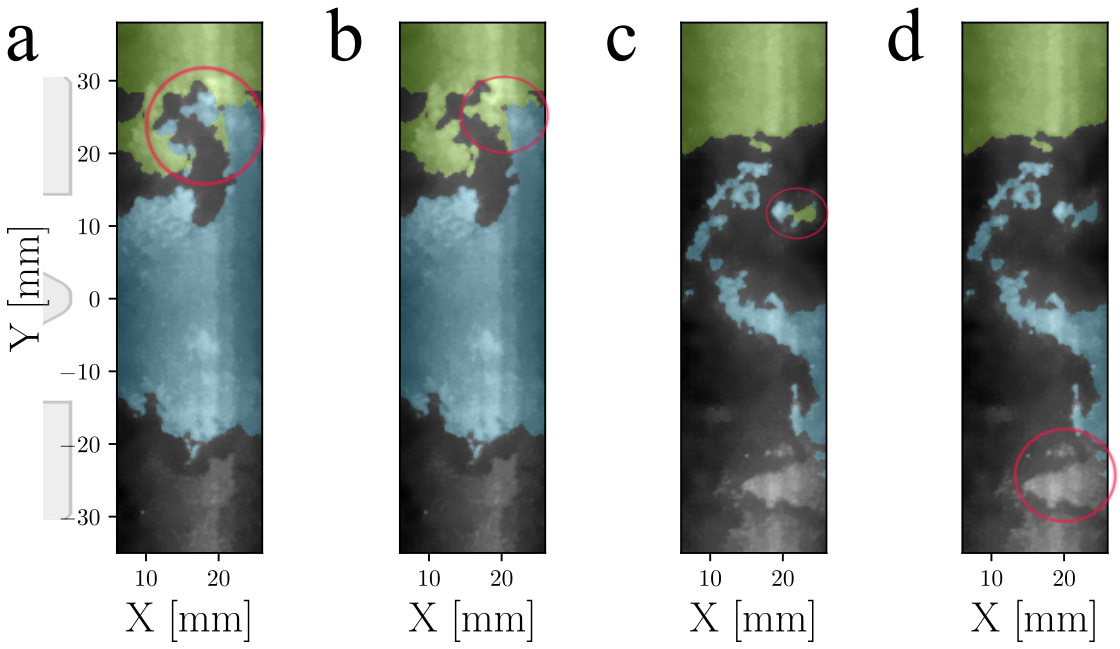

Figure 4.5. Examples of segment merging showing the input(a,c) and outputs (b,d) for the attached flame(a,b) and lifted flame(c,d).

circle that should not be disconnected. These examples are presented to illustrate that the image processing methods are not perfect. Additional training on these failure modes could improve segmentation accuracy. Nevertheless, these issues are rare, and the results provide key insights into the turbulent swirl flame.

4.4 Flame Liftoff and Reattachment

Previous studies on intermittent flame lift-off and reattachment (LR) in swirl flames typically demonstrated the chain of events for a single instance. Every occurrence of flame LR is different due to the chaotic nature of turbulence. Concrete examples are shown in the next section to demonstrate the variance observed at these elevated power density conditions. Instead of detailing the sequence at every LR event, an averaged depiction of flame LR is analyzed. An aggregate of multiple LR

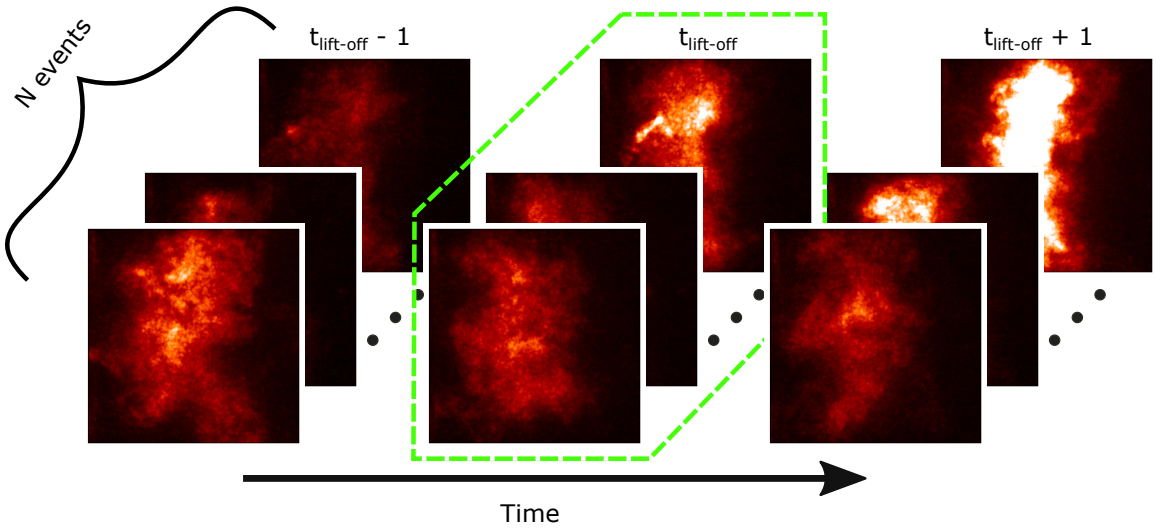

Figure 4.6. Schematic of the flame lift-off conditioning concept. Each row corresponds to a different instance of the flame but is time shifted to the same reference point with respect to flame lift-off.

events using repeated high-speed recordings enables construction of this perspective starting from the precursors of flame lift-off to sustained attachment. This methodology highlights the commonalities between widely varying flame LR events.

The basic concept for this analysis is that a reference time step is determined for every instance of LR. Fields of SPIV, OH*-CL, OH-PLIF, and their derived quantities are then used to calculate conditional statistics. Figure 4.6 shows a diagram of this concept. A time step for flame lift-off is found for each of the N separate lift-off instances and that is used as a new reference point for the time series. As an example, to calculate an average OH*-CL image at the inception of lift-off, all the images in the dashed green box in figure 4.6 are used. The same process applies to conditioning on the flame reattachment time step.

4.4.1 Transient Event Detection

The OH*-CL images are used to detect the onset of flame lift-off and reattachment. A previous investigation utilized OH-PLIF for detection, because it had a higher SNR than the OH*-CL [81]. However, the axial extent of the OH-PLIF images for this work was limited. Moreover, chemiluminescence is a path-integrated measurement, so it provides a better indication of global heat release at the inlet than a planar perspective.

As expected, inspection of multiple lift-off events shows that they are preceded by a decrease in OH*-CL intensity at the inlet. Previous investigations of the combustor at different operating conditions also point to the inlet being very sensitive towards flame lift-off [45, 80, 82]. Figure 4.7 shows a OH*-CL image at the point of flame lift-off. A rectangular mask at the inlet spans ± 10 mm in the vertical (Y) and 0-5 mm in the axial (X) direction. OH*-CL intensities within the rectangular domain are averaged to create a 1D time series. In addition, figure 4.7 displays a partially transparent gray mask based on an Otsu threshold of the image [96]. All OH*-CL intensities below this threshold are set to zero for creation of the 1D time series. Therefore, the average inlet intensity for this instance is zero indicating flame lift-off. This produces a distinct delineation for the onset of flame lift-off.

The Otsu threshold maximizes the variance between two parts of the intensity distribution for each image. This naturally distinguishes between the low intensity background and the bright flame regions. Other global thresholding techniques were evaluated such as Yen's, Minimum Cross Entropy, and ISODATA methods which all gave similar results [109–111]. The Otsu threshold is thus chosen, because it has a simple interpretation and multiple other experimental investigations also use this technique for OH species imaging in swirl flames [112–114].

An example OH*-CL time series is shown in figure 4.8. The two LR events are evident based on a sustained period of near zero intensities. The methodology to automatically detect these events is outlined as follows. The first time step where the

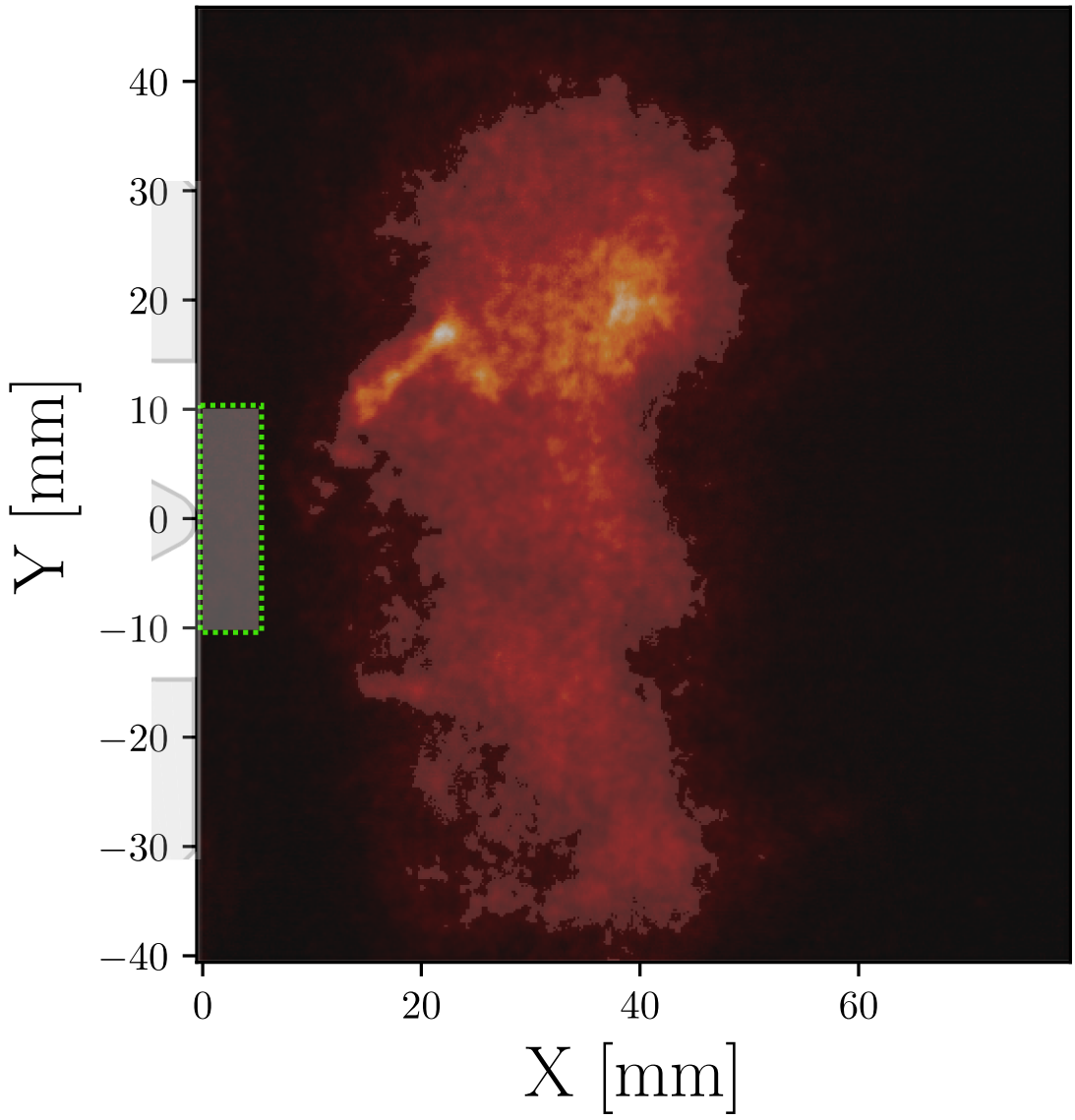

Figure 4.7. Sample OH*-CL image at the point of flame lift-off with an overlay of an Otsu threshold. The rectangular averaging domain is outlined in green.

intensity equals zero is selected. The average intensity for over a number of future time steps is compared against the 25th percentile of all intensity values in the time series. Only sustained periods of flame lift-off are analyzed in this work, so any short lived events are filtered out. An empirical choice of three thermoacoustic periods is used, as represented by a green bracket in figure 4.8. The thermoacoustic frequency was found to be 450 Hz as denoted in previous investigations at the same operating condition [44]. If the average intensity during this period is greater than the 25th percentile, then the next time step where intensity equals zero is chosen. This is shown in figure 4.8 by points a and b, where a is ignored and b is chosen as the beginning of flame lift-off.

Time step selection for flame reattachment is simply based on a 75th percentile threshold. The dotted blue lines in figure 4.8 show the first time steps after flame lift-off where the intensity is above this threshold. Lastly, subsequent LR events must be spaced by at least 5 thermoacoustic periods to avoid cases of exceedingly brief reattachment.

Figure 4.9 shows multiple LR events with varying characteristics to illustrate the chaotic nature of these transient events. Chamber pressure is also overlaid to show its response to flame lift-off. Two LR events lasting about 10 and 12 ms are shown in figure 4.9a and c, respectively. a displays intensity oscillations throughout the lift-off duration with a sudden transition back to an attached flame. In contrast, c shows no oscillations after lift-off, but flame reattachment is preceded by a few time steps at elevated intensities. Figure 4.9b illustrates a lifted flame that lasts over 40 ms. Here, chamber pressure oscillations are even more damped than the shorter LR instances. In all three lift-off events, the very prominent TA oscillation becomes distorted by higher frequency oscillations until the flame is reattached. In addition, a pattern appears that the time steps for flame LR coincide to the positive anti-node of the chamber acoustics. A ignored flame LR event is highlighted by an asterisk in figure 4.9d to illustrate that the empirical thresholds in the LR detection scheme were able to neglect these short LR events. In addition, three instances, circled in green on

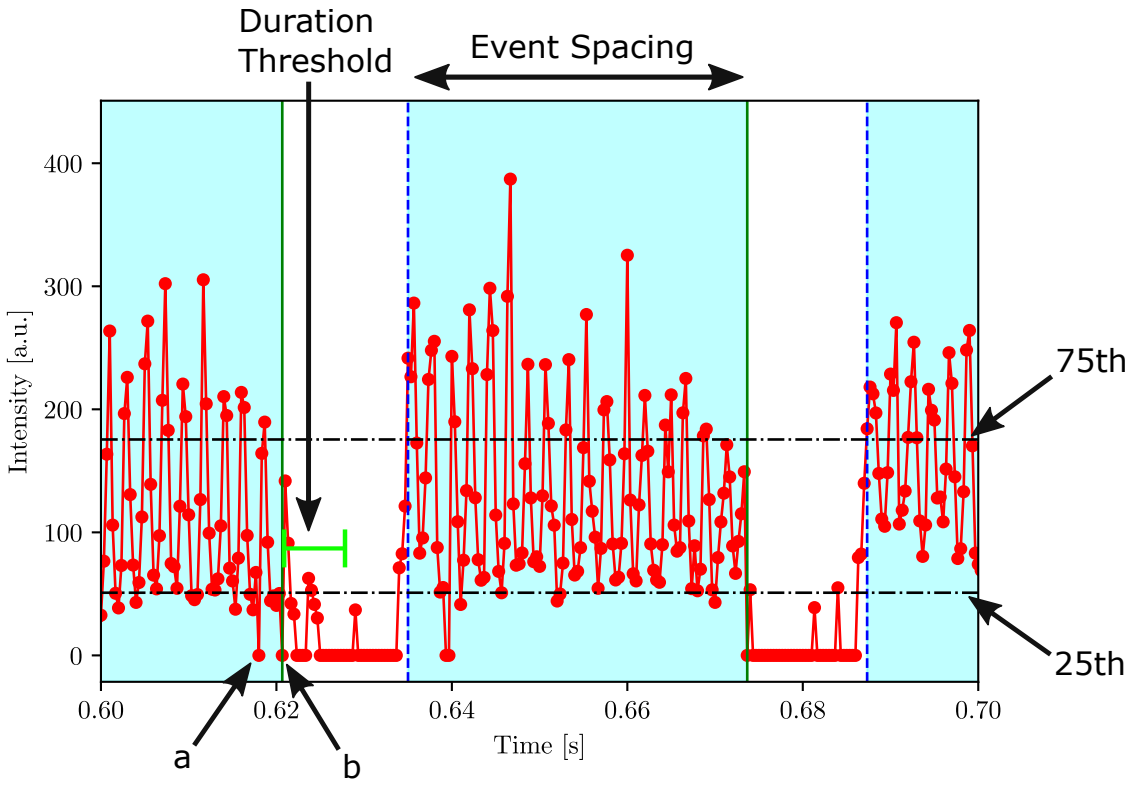

Figure 4.8. Averaged OH*-CL intensities near the inlet demonstrating two LR events. Annotations correspond to empirical metrics used for time step selection of LR.

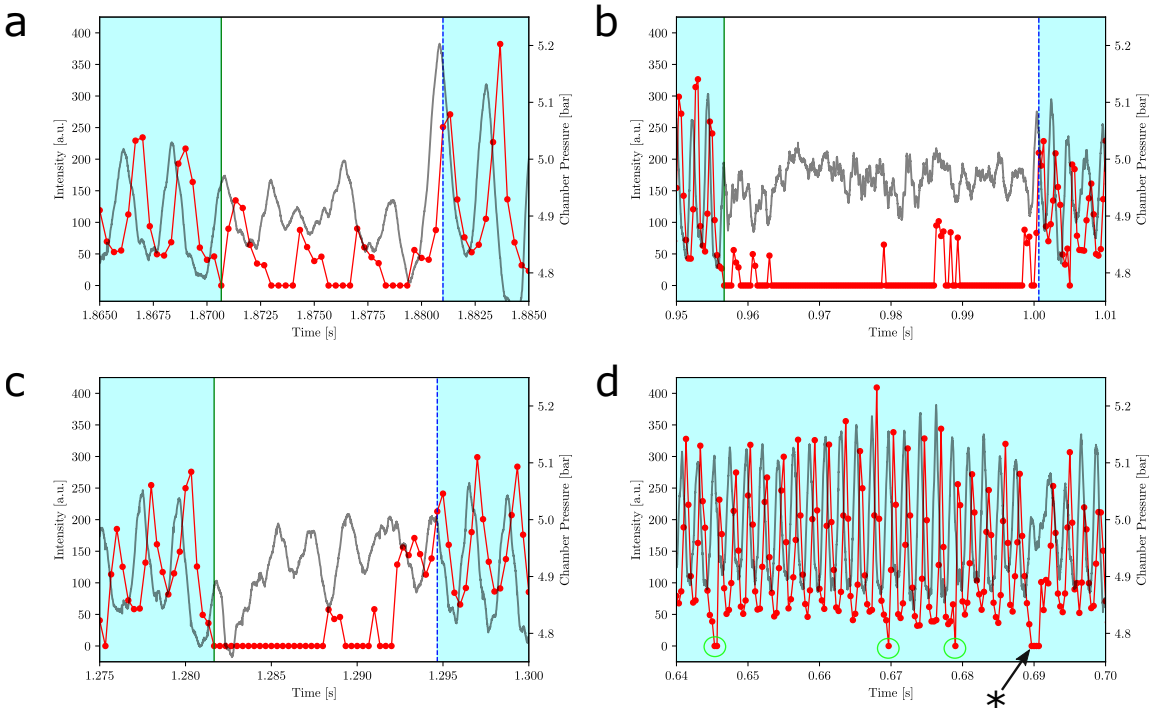

Figure 4.9. Three accepted instances of flame lift-off (a,b,c), and one realization, shown by an asterisk, that is ignored (d). Gray and red lines correspond to chamber pressure and average OH*-CL at the inlet, respectively.

figure 4.9d, where the inlet OH*-CL intensity drops to zero for only one or two time steps. The limit-cycle chamber pressure oscillations show no change at these time steps, so these cases are also rejected.

4.4.2 Average Characteristics

Using the time steps for flame lift-off, an average lifted and attached flame can be investigated. The longer OH*-CL recordings allowed for 36 instances of flame lift-off, while the OH-PLIF and SPIV measurements only netted 26 instances of flame lift-off. There was one more instance of flame reattachment, because the beginning of a recording was when the flame was already lifted. The previous investigation at

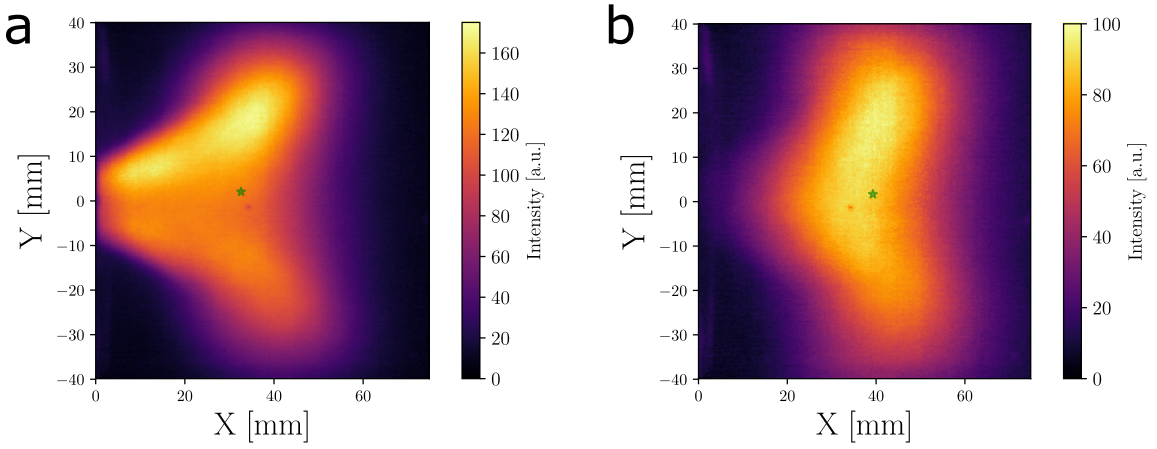

Figure 4.10. Averaged OH*-CL image for the attached (a) and lifted (b) flames. The intensity weighted centroid position is shown by the $\star$ symbol. Note that the colormap is scaled differently between the two images.

atmospheric conditions had only incorporated 7 instances of lift-off and reattachment [81]. The attached and lifted flame images are averaged over 33 and 20 time steps, respectively. This coincides with the parameters used in the detection scheme in the previous section.

Figure 4.10a shows the average OH*-CL image for the attached flame with a characteristic V shape. In contrast, the lifted flame in figure 4.10b is more diffuse with the highest intensities shifted further downstream. Note that the intensity scaling is different for the lifted and attached flames. As expected for a lifted flame, the inlet region from $0 \leq X \leq 10$ mm shows a characteristic absence of heat release. The intensity weighted centroid of both averages are displayed as green $\star$ symbols in figure 4.10. The centroid axial position is 6.7 mm further downstream for the lifted than the attached flame.

The CRB and upper OSL OH-PLIF segments are separated to construct two distinct averages for the attached and lifted flames. For example, while calculating the average CRB image, any pixel that doesn't coincide to the CRB class is ignored. This

effect can be seen in figure 4.11, where all of the uncolored portions of the images correspond to spatial locations where either the CRB or upper OSL were never present. Figure 4.11a,b shows the average OH-PLIF intensities for the CRB of the attached and lifted flames, respectively. The attached flame shows the highest OH concentrations in the inner shear layer where the reactant jets and CRB interact. In contrast, the lifted flame has the highest concentrations near the vertical centerline. The instantaneous OH-PLIF images for the lifted flame indicates that this concentration peak is due to the downstream shift of the flame root. The OH concentrations are also more diffuse similarly to the average OH*-CL image for the lifted flame. Figure 4.12a,b shows the average OH-PLIF intensities for the upper OSL of the attached and lifted flames, respectively. For the same axial positions, the lifted flame shows higher OH concentrations indicating more recirculation into the corner or wall regions of the combustor. This phenomenon is characteristic of other lifted or "M" shaped flames [45,84]. In addition, the upper OSL has a greater spatial extent downwards to the centerline of the combustor. Overall, there are less striking differences in the OH concentrations between lifted and attached flames in the upper OSL than the CRB.

The averaged velocity components along with swirling strength (λ_{ci}) are shown in figure 4.13 for attached flames in panels a,c,e,g and lifted flames in panels b,d,f,h. Swirling strength has been used in multiple experimental investigations to identify vortices [32,33]. Vorticity has a fundamental drawback for vortex identification where shear without rotation results in high values, whereas swirling strength better isolates rotation.

The CRB has been shown to undergo dramatic changes during flame lift-off from OH*-CL and OH-PLIF meausurements. Likewise, the region of negative u_x corresponding to the CRB spatially contracts and has lower velocities in the lifted flame. This means less recirculation of hot combustion products to sustain heat release in the inner shear layers as seen in the OH measurements.

A distinct alternating spatial pattern appears for the lifted flame u_y average image. This is indicative of rotation, and the average swirling strength images suggest the

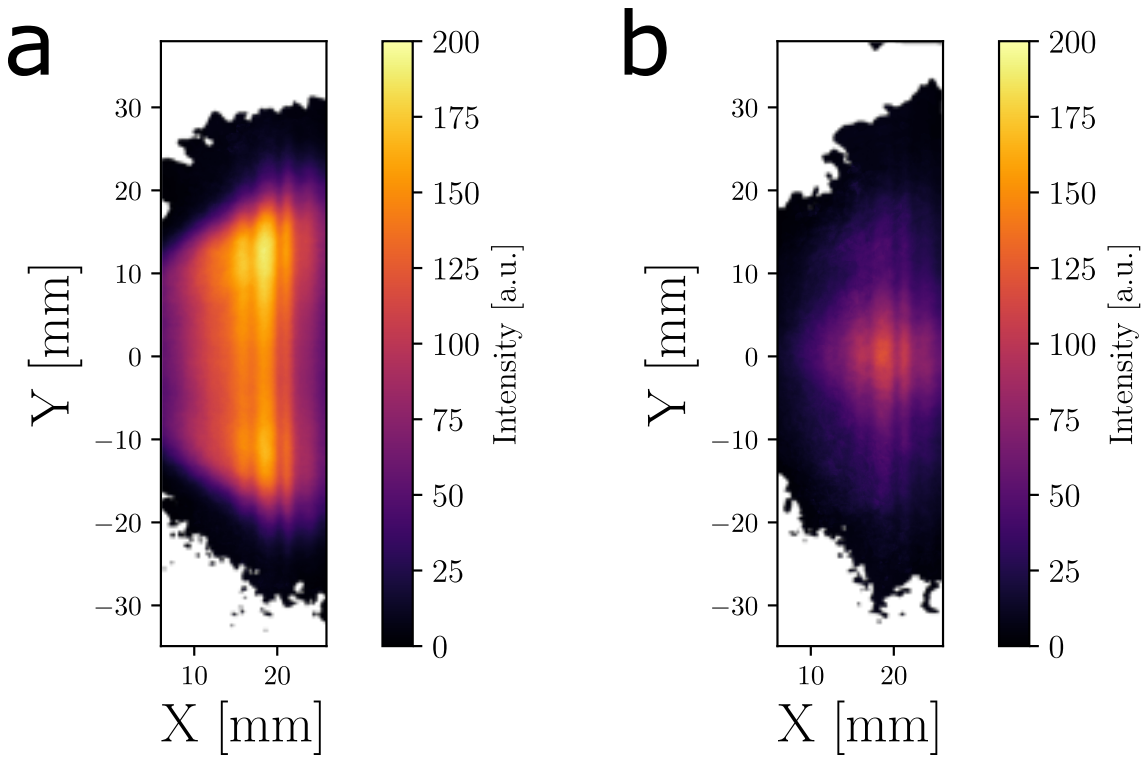

Figure 4.11. Average OH-PLIF images of the CRB for the attached (a) and lifted (b) flames.

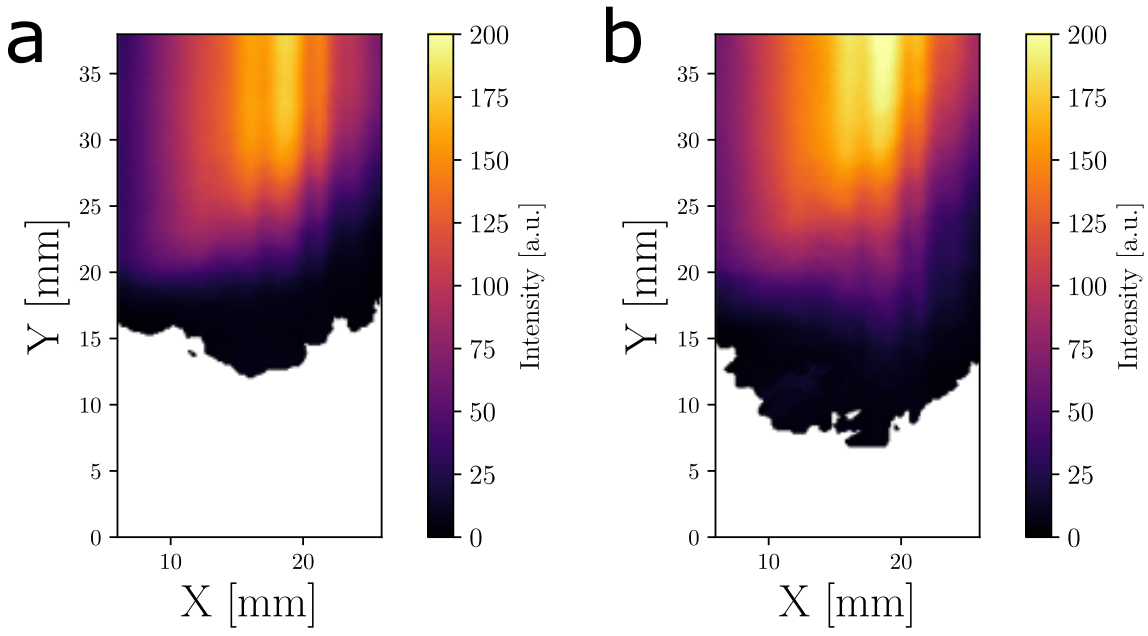

Figure 4.12. Average OH-PLIF images of the upper OSL for the attached (a) and lifted (b) flames.

same phenomena. The inner and outer shear layers of the reactant jet are easily discernible in figure 4.13g,h as two diagonal bands of high swirling strength. The inner shear layer shows far higher values while the flame is lifted than attached. Previous investigations of the PRECCINSTA burner with bistable flames observed the formation of a PVC leading to flame lift-off. However, at this operating condition the PVC is present when the flame is attached, but the rotation rate is greatly increased when the flame is lifted. A series of staggered vortices, indicative of a helical PVC, are seen in the instantaneous velocity fields for the lifted flame. The PVC also seems to become more vertically narrow as it borders the CRB which is contracted while the flame is lifted.

A previous investigation of this combustor at elevated power density demonstrated that the presence of a PVC was the delineating flow structure for TA instability [44]. The PVC modifies mixing and the associated time delays between the acoustics and heat release to generate the limit cycle behavior seen in the attached flames. Chamber pressure oscillations are reduced for the lifted flame as seen in figure 4.9, but the PVC is still present. The average OH*-CL and OH-PLIF images indicate that heat release is no longer concentrated in the inner shear layer where the PVC resides. This changes the convective time delays enough to dampen the thermoacoustic coupling, which is observed in the chamber pressure measurements as the periodic oscillations are reduced.

Based on u_x and u_y alone, the opening angle of the reactant jets does not appear to be greatly different between the attached and lifted flames. However, the average u_z images tell a different story. Figure 4.13e shows high velocity jets that quickly decay for the attached flame, but the jet angle flattens by about 10° in the lifted case (figure 4.13f). The high u_z velocities also extend farther downstream and coincide to the largest values of swirling strength in the lifted flame. It appears that increased rotation rate in the inner shear layer is accompanied by higher out-of-plane velocities.

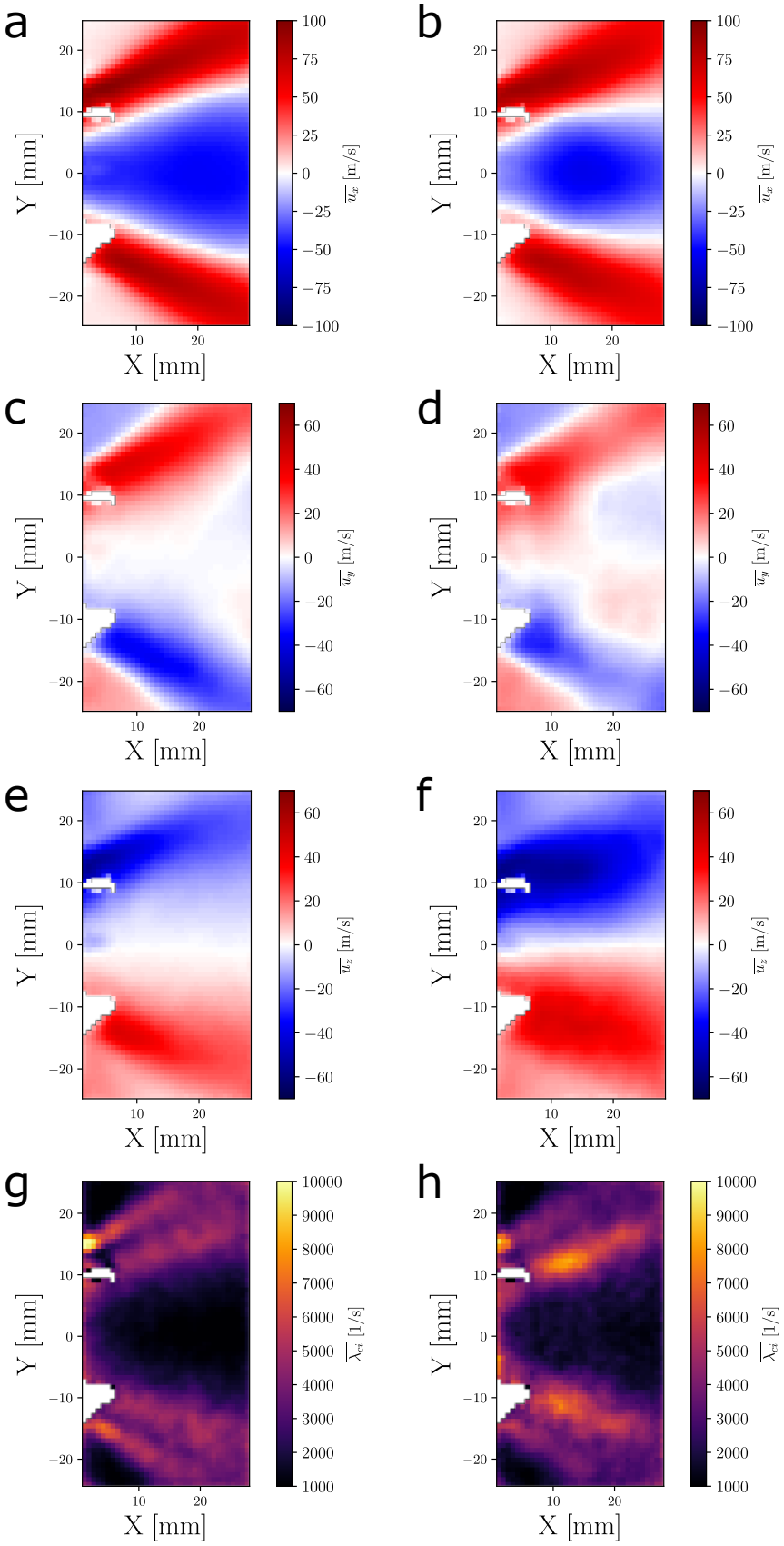

Figure 4.13. Averaged velocity and swirling strength fields for attached (a,c,e,g) and lifted (b,d,f,h) flames.

4.4.3 Morphology

The edges of the CRB or upper OSL segments are computed by a marching squares method applied to a binarized image [115]. Therefore, no intensity weighting is performed such as only including edges around super equilibrium concentrations of OH. Thus, edges in this analysis do not always correspond to flame fronts. Even with this limitation, much can be deduced from the morphology of the flow structures seen in the OH-PLIF images.

Figure 4.14a,b shows the probability that a CRB edge will be present at every pixel for attached and lifted flames, respectively. The regions of high probability correspond to the expectations laid out in the previous section. The V flame shape is very prominent for the attached flame. The flame root has moved downstream for the lifted flame, so more edges are concentrated near the vertical centerline where there are seldom edges in the attached flame.

The changes to the upper OSL are again not as dramatic as the CRB. The average trajectory of the edges has been maintained, but downstream regions have more vertically downward spread for the lifted flame (figure 4.15). This follows the patterns suggested in the previous section where the negative u_x region narrows, which then causes the reactant jet trajectory to flatten. Thus, enabling the upper OSL to move downward.

Another method to observe the changes to the CRB is analyze the stagnation lines, which is defined by an iso-contour of $u_x = 0$. The contours in the outer shear layers are removed by enforcing a threshold that most of the contour positions must lie within a empirically determined spatial mask. The only stagnation lines left correspond to the inner shear layer. Figure 4.16a,b shows the probability that a stagnation line exists at each spatial position for attached and lifted flames, respectively. The spatial dispersion of probability for the lifted flame is larger than the attached flame indicating greater fluctuation of the stagnation line. The inlet region from $0 \leq X \leq 5$ mm also displays increased probability, because the flame lifts and the root appears

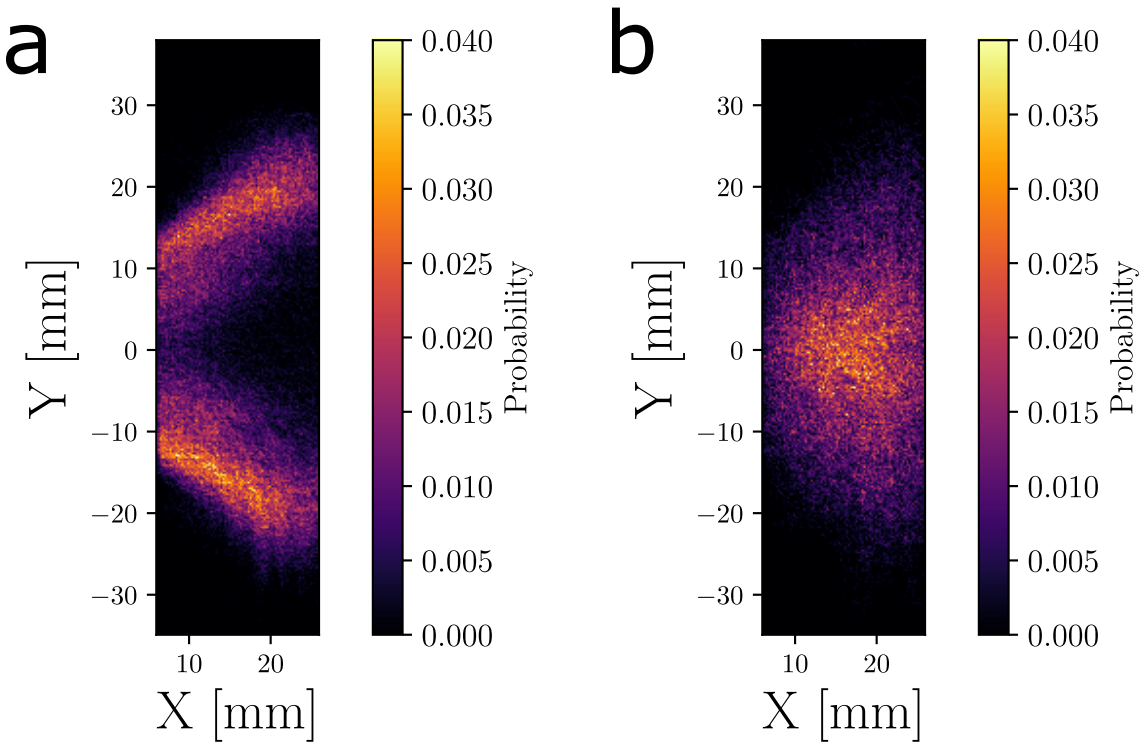

Figure 4.14. Probability of a edge corresponding to the CRB segments from the OH-PLIF images for the attached (a) and lifted (b) flames.

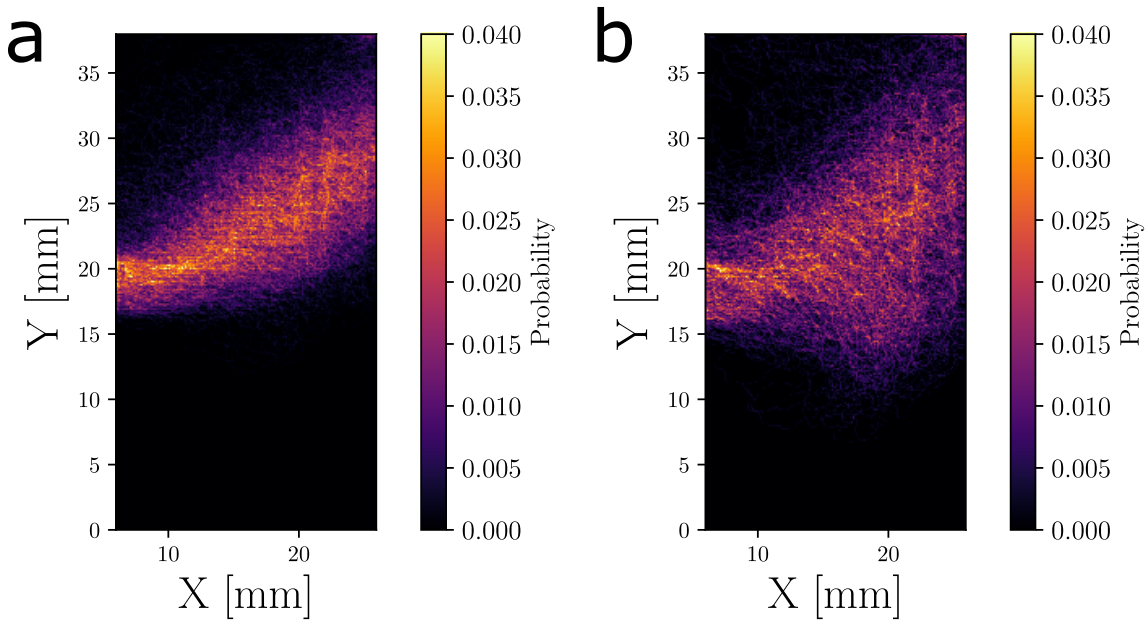

Figure 4.15. Probability of a edge corresponding to the upper OSL segments from the OH-PLIF images for the attached (a) and lifted (b) flames.

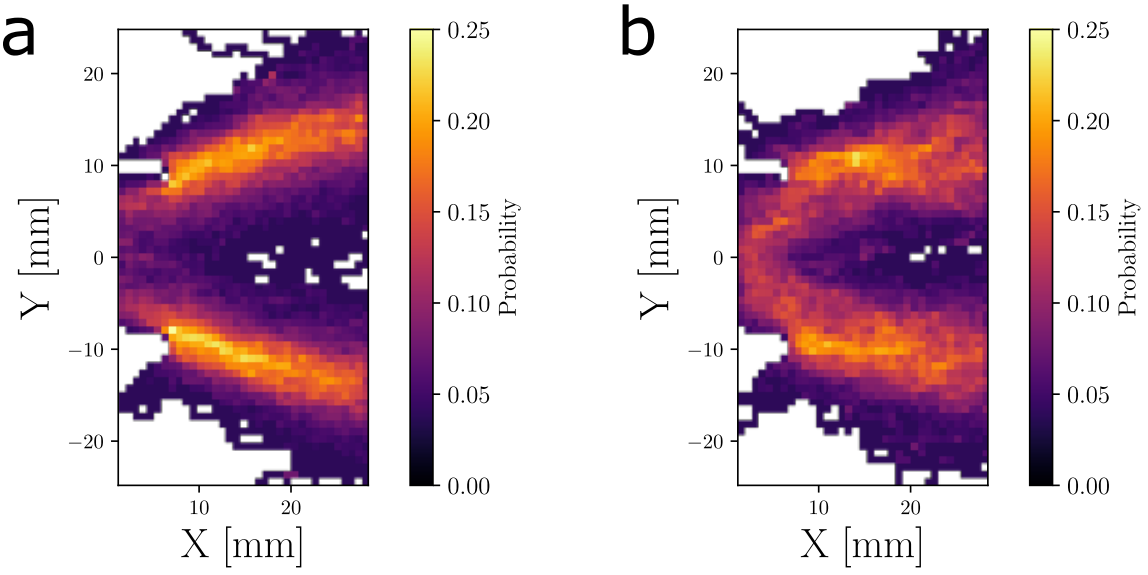

Figure 4.16. Stagnation line likelihoods for attached (a) and lifted (b) flames.

within the field of view. Figure 4.16b also better illustrates the CRB narrowing, where the central region of lower probabilities is shrunk for the lifted flame.

The morphology of the CRB derived from semantic segmenation of the OH-PLIF images is analyzed in a quantitative manner for both flame regimes. Figure 4.17a shows the PDF of the number of distinct segments using a connected components analysis with 8-connected neighborhoods. For each of these segments, an area is computed simply by a pixel count, which forms the PDF shown in figure 4.17b. A bimodal distribution appears for the segment areas in the attached flame. The peak at about 650 mm^2 corresponds to the large connected segments such as what is shown in figure 4.4b. The sub 200 mm^2 segments are due to vortex rollup in the inner shear layer pinching off regions of OH from the main body and very small pockets of OH, both can be seen in figure 4.5a. The disappearance of the high area peak in the lifted flame is due to the flame root moving downstream causing more OH to be out of the field-of-view in the OH-PLIF images.

The lifted flame has been shown to be more dynamic than the attached case with stronger rotation and greater movement of the stagnation lines. This causes enhanced mixing between OH trapped in the CRB and reactants in the high velocity jets. These changes to the velocity field explain how the lifted flame displays a propensity towards an increased number of reduced area segments.

Curvature statistics are used to analyze the changes to strain and wrinkling of the CRB as defined by either the stagnation lines or OH segments. The curvature values give a sense to the length scales where high curvature indicates wrinkling at small spatial scales. The parametric coordinates of each curve are refined by fitting smoothed third order splines. A very similar methodology is performed for OH-PLIF images from a pair of interacting swirl flames [116]. Smoothing was necessary for the binarized OH-PLIF segments, because the edges were heavily aliased resulting in unrealistically high spatial frequencies. Spline interpolation allows for computation of analytic derivatives and reduces error inherent in finite difference methods, especially if points defining the edges are sparse. The derivatives are then used to calculate curvature by $\kappa = \frac{x'y'' - y'x''}{[(x')^2 + (y')^2]^{\frac{3}{2}}}$. Curvature is a signed quantity, and the analysis here follows the convention where the normal vector of the curve points towards the incoming reactant flow [28, 30, 117, 118]. For example, a perfectly circular pocket of OH surrounded by reactants would have a positive curvature equal to the inverse of the radius.

Figure 4.18a,b represent PDFs of curvature for the stagnation lines and edges from the OH segments classified as the CRB, respectively. The mean absolute value of curvature is denoted by the dashed lines, and the standard deviation of the signed curvature is plotted as the solid lines. Both of these statistics indicates finer wrinkling for the lifted flame suggesting that mixing and combustion is shifted to smaller length scales. The mean absolute value and standard deviation of curvature from both measurements are roughly 13% and 9% greater, respectively, for the lifted flame. In addition, the distribution for the lifted flame is skewed towards positive values (figure 4.18b). This could be due to the increased presence of isolated OH pockets, which

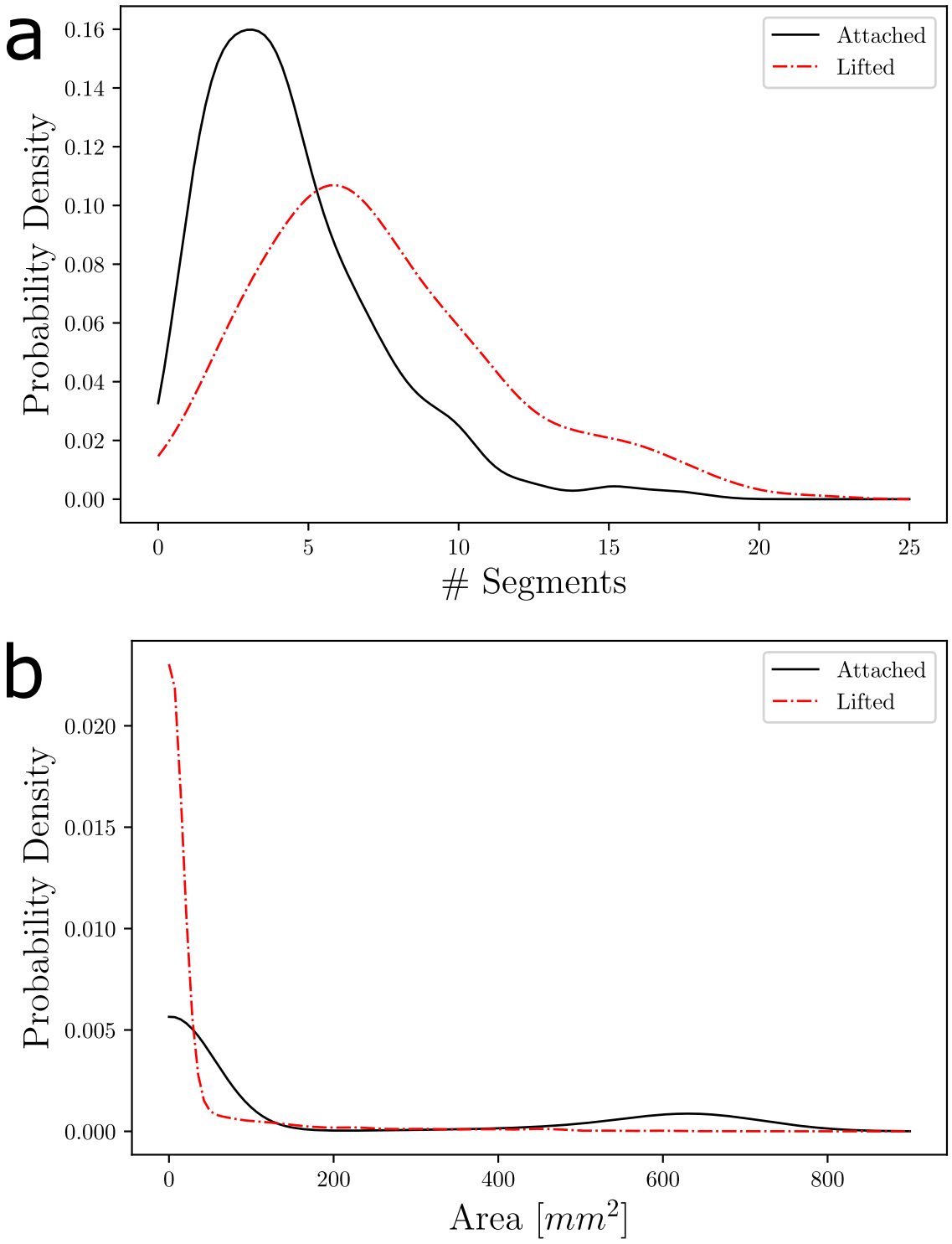

Figure 4.17. Distributions for the number of connected segments classified as the CRB (a) and the area of each connected CRB segment (b).

have a net positive curvature. Reinforcing this notion, such effects are not seen in the stagnation line curvature distribution.

Other investigations have studied flame front curvature using DNS of a high pressure turbulent bunsen flame and single flame kernels [28, 117]. Results indicate that increasing the velocity fluctuations or reducing the length scales led to the an increase in the curvature standard deviation. In order to analyze the turbulent intensity in the lifted and attached flames, a notch filter is applied to the mean subtracted velocity field at every spatial location throughout the SPIV time series [119]. This is necessary because the thermoacoustics, predominantly in the attached flame, causes the velocity fields to oscillate at a regular frequency. The velocity fluctuations would be abnormally high for the attached flame without any filtering. A fluctuation RMS velocity is then calculated for 3 TA cycles (20 time steps) before and after each flame lift-off event. Figure 4.19 shows the RMS velocity fields averaged over every instance of flame lift-off and split into attached and lifted flames. Velocity fluctuations have increased almost everywhere for the lifted flame. Certain locations can even be 100% greater than the attached flame. This can attributed to the strengthening of the PVC when flame lift-off occurs. Accordingly, the maximum fluctuation RMS values are in the inner shear layer where the PVC resides. These findings combined with the curvature statistics matches the relationship described in other investigations of turbulent flames.

4.4.4 Indicators of Flame Transition

The pathway towards flame LR is investigated in an averaged manner, so that only the features found in the majority of LR events are highlighted. If a consistent predictor of flame LR is sought, then one would not want to rely on features that only appear for a single event. First, OH*-CL measurements are analyzed to investigate a path-integrated measure of heat release. An averaged OH*-CL image is computed per the methodology shown in figure 4.6.

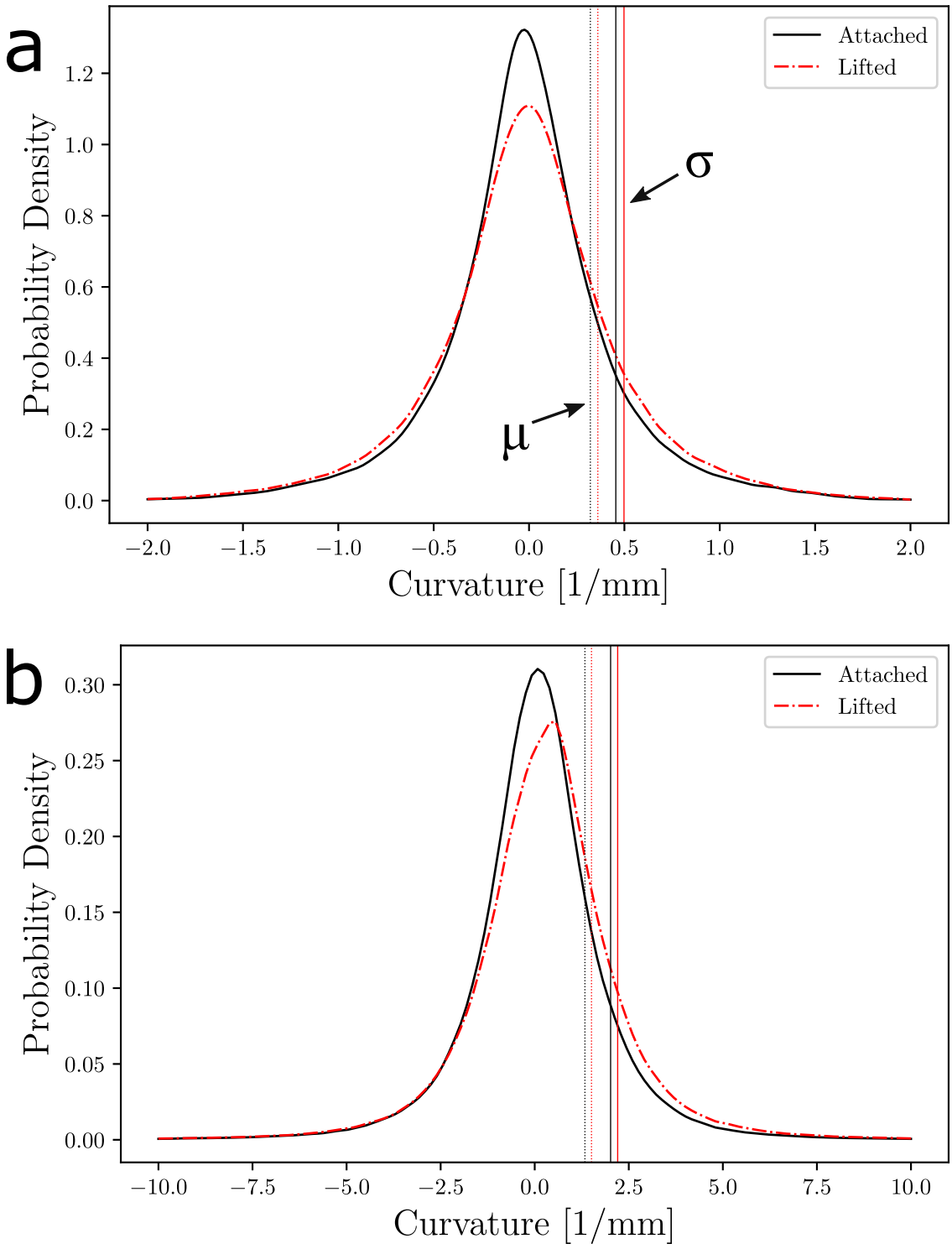

Figure 4.18. PDFs of curvature for the stagnation line (a) and edges of OH segments classified as the CRB (b). The mean absolute value and standard deviation of curvature are represented by dashed and solid lines, respectively.

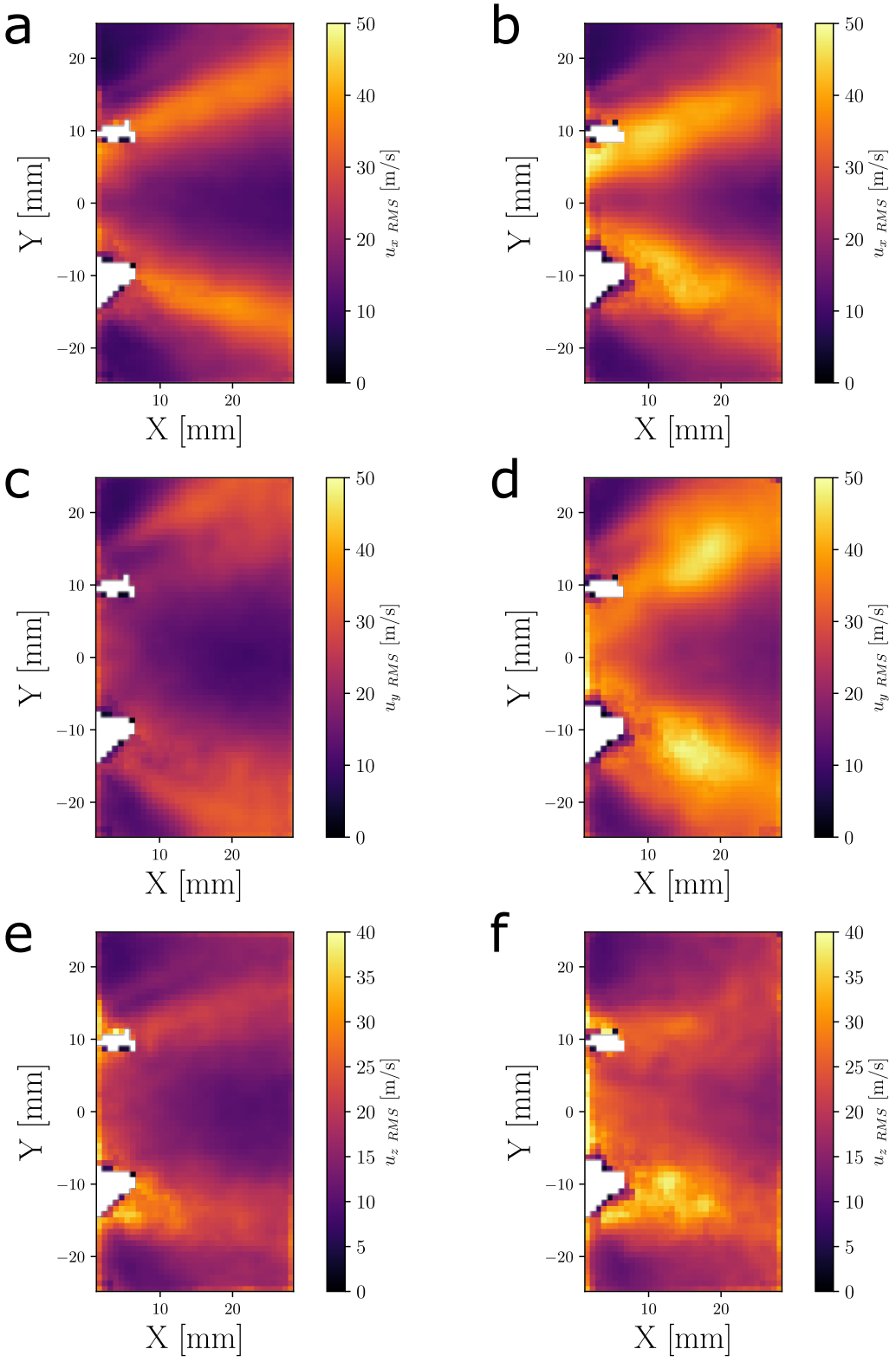

Figure 4.19. Fluctuation RMS velocities for attached (a,c,e) and lifted (b,d,f) flames.

Figure 4.20a shows the distribution of intensity values of the averaged OH*-CL images at specific time steps in relation to the flame lift-off (left subplot) and reattachment (right subplot) reference time step denoted by a dashed green line. A dashed green line denotes the time step where flame lift-off or reattachment occurs. Probability densities below 0.001 are set to black. The mean intensity is overlaid on the histograms to provide a robust depiction of central tendency. The global perspective provided in figure 4.20a shows no discernible features that would signal flame lift-off. However, flame reattachment is preceded by increasing intensity fluctuations but at a lower frequency than what is observed in the attached flame. The green arrow in figure 4.20a shows the intensity distribution spreads towards higher values starting from 14 time steps before flame reattachment. Similarly to the single lift-off events shown in figure 4.9, the flame on average displays less susceptibility to TA oscillations while lifted. This is in contrast to another operating condition for the PRECCINSTA combustor where the attached flame was TA stable but the lifted flame was unstable [80].

Motivated by the precursors of flame lift-off at atmospheric conditions, the statistics are restricted to the inlet region identical to that shown in figure 4.7 [45,80]. With this spatial conditioning, the cyan arrow in figure 4.20b indicates that the mean intensity falls to a lower value than what is observed in the previous five TA cycles. This results in a notification of less than 1 millisecond before flame lift-off. Thus suggesting that lift-off may be triggered by very sudden perturbations at the inlet. However, flame reattachment again appears to be a more gradual transition. The mean intensity begins to rise 6 time steps before reattachment, denoted by the green arrow in figure 4.20b.

As hinted at in figure 4.9, the LR reference time steps have consistent phase with respect to the chamber pressure. Similar observations were made at atmospheric conditions [81]. This results in a coherent oscillation at the TA frequency of the mean intensity before lift-off and after reattachment. Extending the number of time steps significantly beyond 3 TA periods for the lift-off conditioned case does show flame

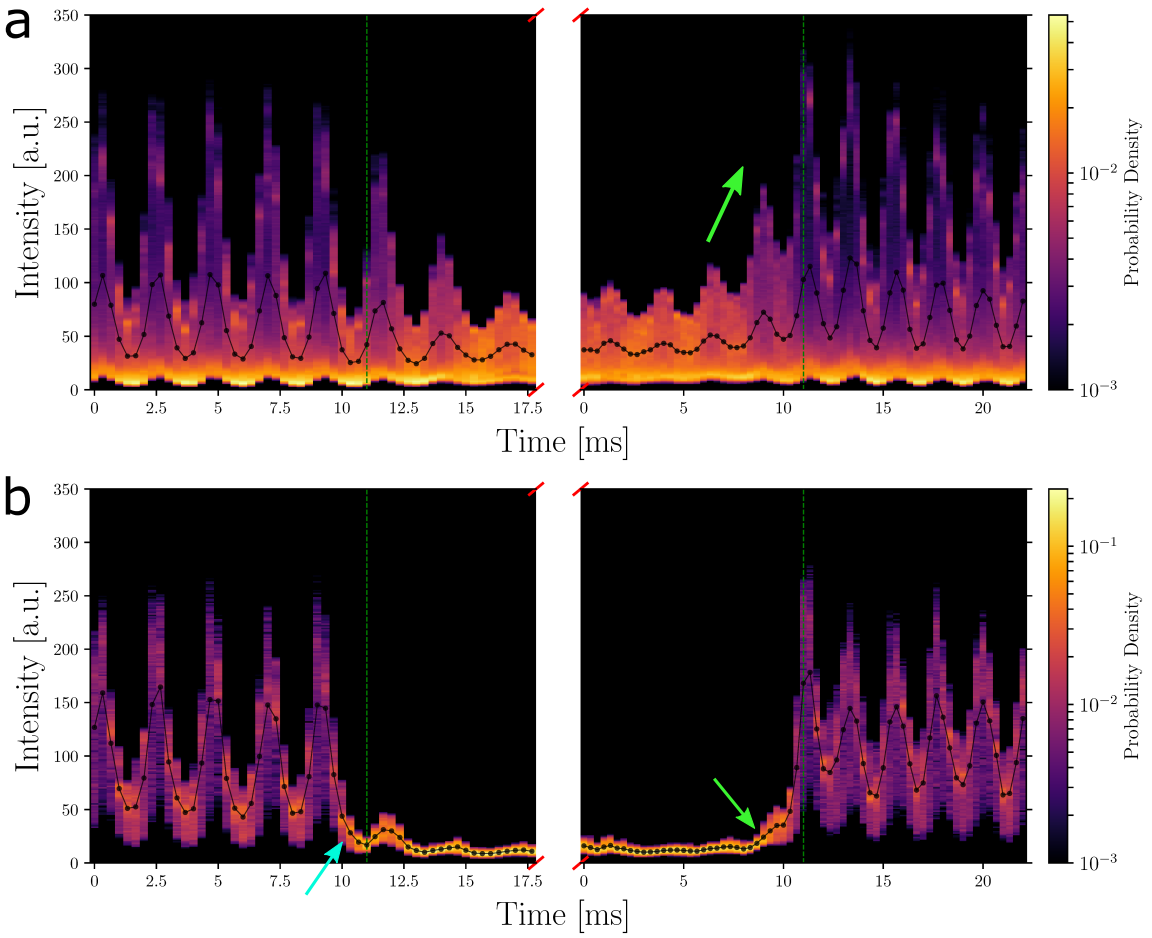

Figure 4.20. Distribution of OH*-CL intensities over the entire field of view (a) and limited to the inlet region (b). The mean intensity is overlaid as a black line of circles.

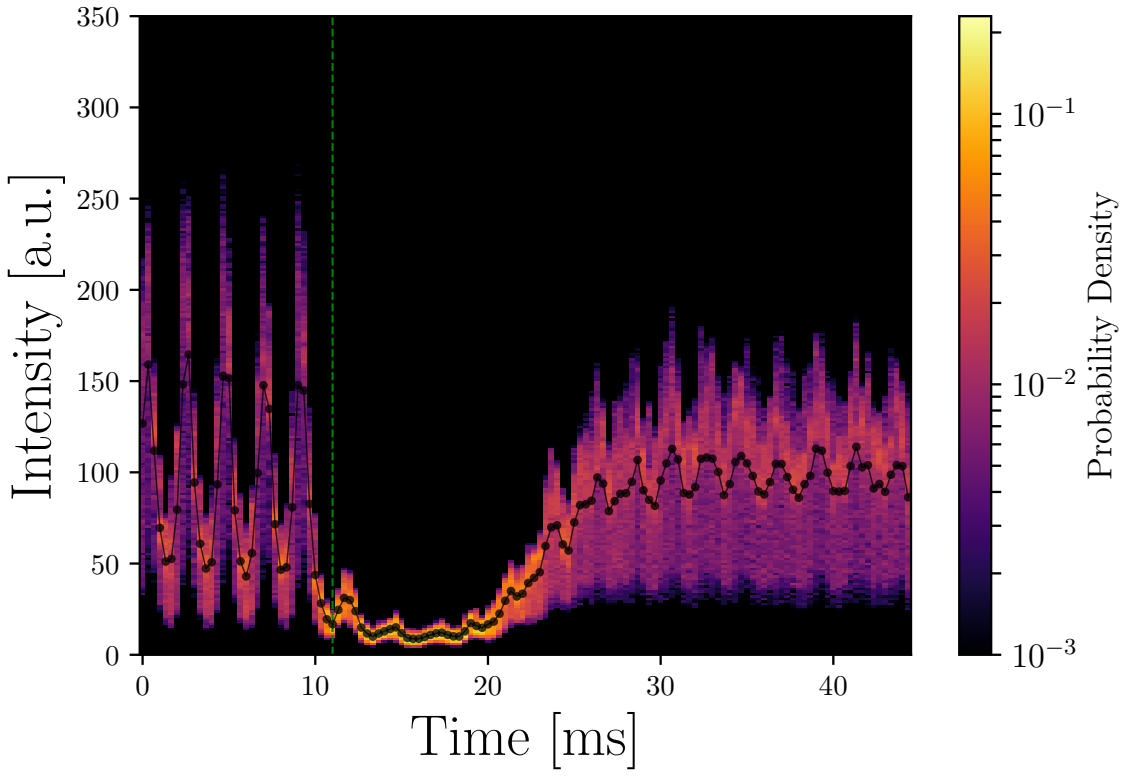

Figure 4.21. Distribution of lift-off conditioned OH*-CL intensities limited to the inlet region but extended to farther times past flame lift-off.

reattachment characteristics. However, phase coherence is lost at the longer time spans, because the exact time when flame reattachment occurs is unique to every event. Figure 4.21 clearly demonstrates this effect by copying the lift-off conditioned portion of figure 4.20b but extended to 33.3 milliseconds after flame lift-off. The periodic oscillations reappear past 30 milliseconds, but it is less coherent than the reattachment conditioned perspective.

For the velocity field, an average image is computed for a number of time steps before and after flame LR. This lift-off and reattachment conditionally averaged image is over of 26 and 27 instantaneous velocity fields, respectively. Restricted to the inlet region, figure 4.22a,b shows the mean u_x and the standard deviation of u_z of the

conditionally averaged velocity fields, respectively. Over 3 TA cycles before flame lift-off, there appears to be a trend of higher peak axial velocities. However, 10 TA cycles are shown in figure 4.22a to demonstrate that increasing velocities are not unprecedented. The lowest axial velocity is circled in green in figure 4.22a and could be an indication of flame lift-off.

The standard deviation of u_z represents the spatial uniformity of the velocity field. It grows to a very large value 1 time step before flame lift-off, which may be a clearer signal than what is seen in the mean u_x. However, this still provides practically zero forewarning time. In addition, both the mean u_x and standard deviation of u_z do not show obvious signs of flame reattachment compared to the OH*-CL measurements. Figure 4.22c shows the average swirling strength across the entire SPIV field of view. Here a steady decrease in swirling strength is observed beginning at 12 time steps before flame reattachment. The amount of time before flame reattachment was increased to 13.3 milliseconds, compared to the 6.7 milliseconds in figures 4.22a,b, to better illustrate this trend. As seen in figure 4.13h, the largest values of swirling strength corresponds to the PVC lying in inner shear layer. This trend then represents a weakening of the PVC that leads to flame reattachment, which is confirmed by a corresponding rise in heat release at the inlet region.

Previous investigations of the PRECCINSTA combustor, at different operating conditions, found that flame lift-off was preceded by a slowly increasing amount of negative axial velocity in the CRB region [80]. This trend was over hundreds of milliseconds, where as the peak negative axial velocity here is observed just 1.67 milliseconds before flame lift-off. Nevertheless, greater velocities at the inlet could destabilize the flame enough to cause the lower heat release at the inlet observed in figure 4.20b. The reduced reaction rate would decrease the local gas viscosity and trigger the PVC to strengthen. This would propagate downstream and cause increased flame quenching as the strain rate would increase beyond the extinction limits. The flame then finds a new stabilization point, which results in a lifted flame.

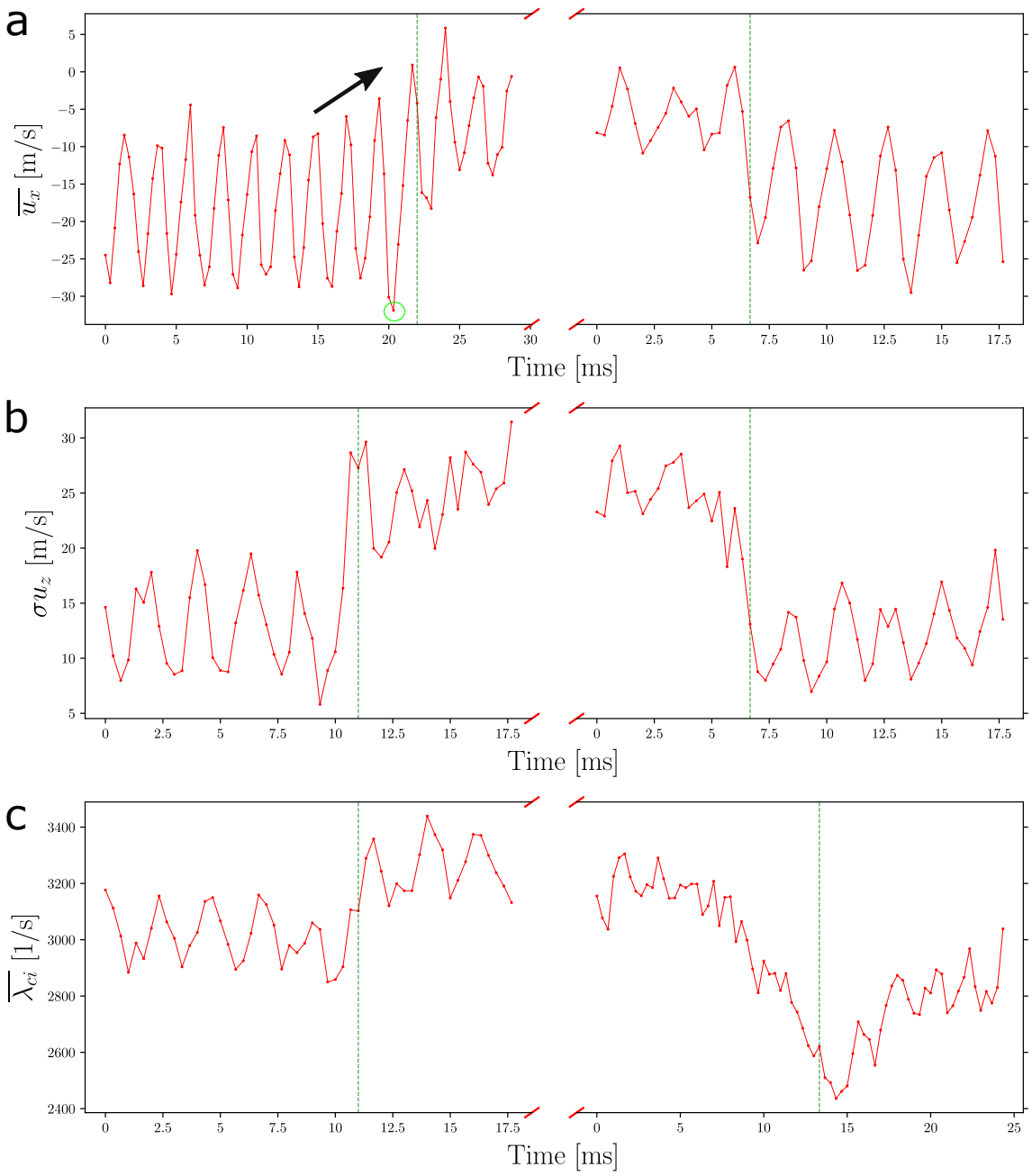

Figure 4.22. Average u_x (a) and standard deviation of u_z (b) over the inlet region. Average swirling strength over the entire SPIV measurement domain (c).

Finally, statistics of the CRB segments extracted from the OH-PLIF images are evaluated for indications of precursor events to flame LR. Figure 4.23a,b shows a time history of the average total area and perimeter of the CRB segments in a LR reference frame. Again, more time steps are shown before flame reattachment than after flame lift-off to better demonstrate trends. The area calculation was described in the previous section. The perimeter of each edge was determined by summing the Euclidean distance between subsequent points. This simple method was compared to a rules based scheme to directly account for corners and diagonal edges and gave similar results [120].

The occurrence of a very low average area only forecasts flame lift-off one time-step ahead. Similar to the average swirling strength, the average CRB area begins to gradually increase 13 time steps before flame reattachment. This point is circled in green in figure 4.23a. At a glance, the average perimeter is no better than the area measure as a forecasting tool. However, a unique characteristic is observed where the highest total perimeter occurs right after lift-off and before reattachment. The cause for this is not abundantly clear, but the instantaneous OH-PLIF images suggest that the regions of OH corresponding to the CRB are heavily distorted at these moments. A sudden rise in mixing from higher swirling strength within the inner shear layer during flame lift-off could partly explain this. However, swirling strength decreases for reattachment, so a different mechanism must be causing the perimeter to gradually increase and then suddenly fall when the flame is reattached.

The centroid based on binarized OH-PLIF segments that correspond to the CRB is evaluated to understand the spatial movement during flame LR. Figure 4.24a,b displays the LR conditionally averaged axial and vertical coordinates, respectively. As markers for flame LR, this metric doesn't perform any better than what has been previously shown. However, these time series still effectively illustrate the traversal of the CRB. The centroid is located further downstream for lifted flame matching the observations from the averaged OH*-CL images in figure 4.10. The vertical position of the centroid stays near the centerline with no obvious periodic oscillation suggest-

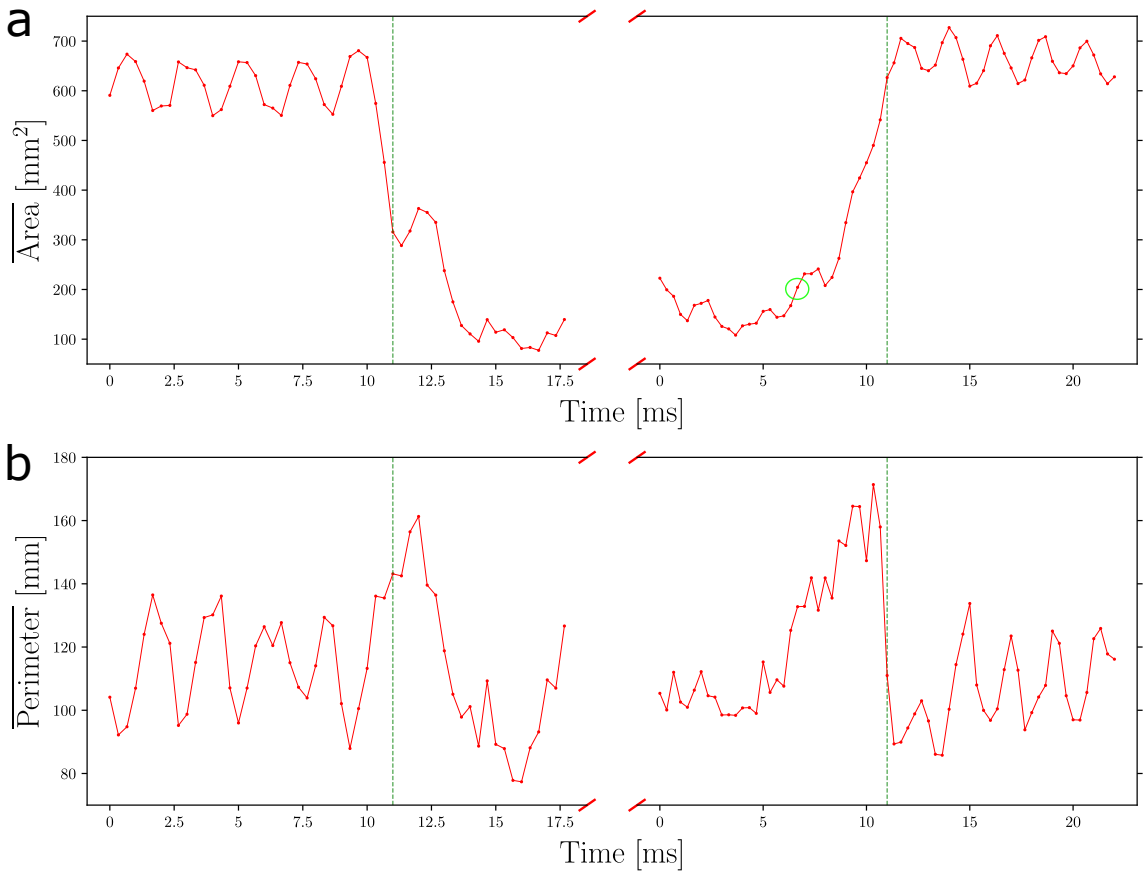

Figure 4.23. Average area (a) and perimeter (b) measures of the CRB.

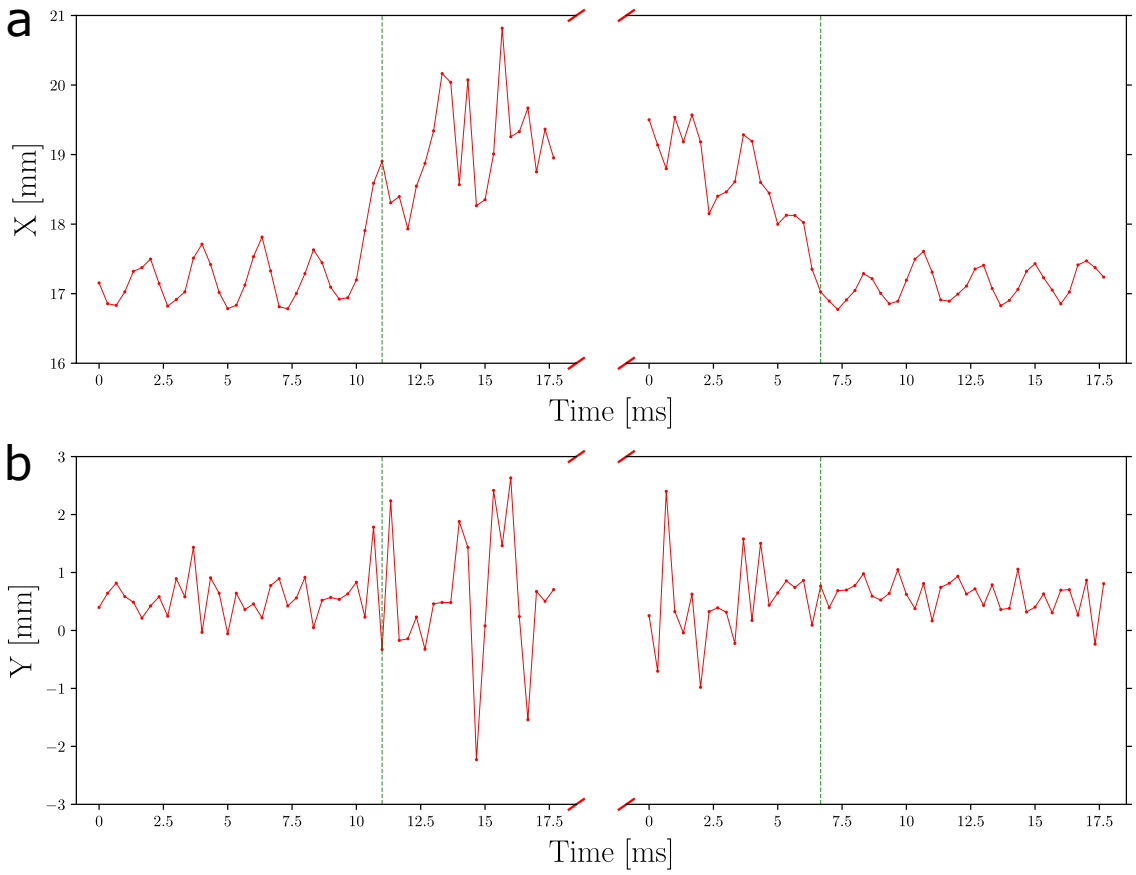

Figure 4.24. Average axial (a) and vertical (b) coordinates of the centroid of the CRB.

ing that the acoustics are predominantly longitudinal when the flame is attached. Fluctuations in the vertical coordinate increase for the lifted flame, which may result from the action of a stronger PVC that heavily shifts the OH within the CRB.

The insights gained from the OH-PLIF help refine our understanding of flame reattachment. As the PVC weakens, indicated by lower average swirling strength, the flame becomes less strained. The flame root is then allowed to move upstream as seen in figure 4.24a. More heat release increases the local gas viscosity further weakening the PVC. This pattern is repeated until the flame is reattached to the

conical centerbody. The convective time delays are re-established to a condition allowing for thermoacoustic instability to present itself again.

These results indicate that either OH*-CL or u_x at the inlet provide the most forewarning to flame lift-off. For flame reattachment, the OH*-CL statistics across the entire flame slightly outperformed both the summed area of CRB segments from the OH-PLIF images and the average swirling strength. The PLIF and SPIV measurements bolster the notion, first described analyzing OH*-CL, that flame lift-off is caused by a very sudden perturbation near the inlet. In terms of practicality towards control in industrial gas turbine combustors, chemiluminescence is far more feasible than the laser diagnostic techniques. However, the time scales shown here are on the order of milliseconds and represent a challenge for real-time prevention of flame lift-off. This problem would be exacerbated by even smaller time scales at very high Reynolds numbers, which is commonplace for modern gas turbine combustors operating at high pressure. It may be possible that each flame lift-off event demonstrates unique precursor features at times long before lift-off. The averaging in this analysis would hide these inconsistent phenomena, but further investigation along these lines is beyond the scope of this work.

4.5 Conclusion

Intermittent flame lift-off and reattachment events were analyzed in a swirl flame undergoing theromacoustic instability with simultaneous 3 kHz OH*-CL, SPIV, and OH-PLIF. The moment of flame lift-off and reattachment was determined by empirical thresholds based on the OH*-CL intensities at the inlet of the combustor. This methodology was shown to reliably isolate the lifted flames and disregard instances of very short lift-off.

Processing techniques for OH-PLIF images were presented to tackle the challenges present in high pressure flames with multiple flow structures and limited laser power. Non-local means denoising was effectively demonstrated to remove camera and in-

tensifier noise to produce higher contrast OH-PLIF images. A convolutional neural network was trained to perform semantic segmenation with very high proficiency. It superbly classified and segmented portions of the image which corresponded to the CRB and upper OSL.

With the augmented OH-PLIF dataset, average characteristics of the attached and lifted flame are compared. Flame lift-off is immediately apparent from an averaged OH*-CL image. The OH-PLIF statistics indicated a dramatic reduction in reaction rate within the inner shear layer. The velocity fields showed major flow structure changes with a weakened CRB and stronger PVC for the lifted flame. Morphological investigations of the CRB show greater wrinkling and spatial movement for the lifted flame.

Lastly, signals indicating imminent flame lift-off and reattachment are sought. The average OH*-CL and axial velocity at the combustor inlet displayed the most sensitivity towards flame lift-off, but with only a couple milliseconds of forewarning at best. On the other hand, flame reattachment was gradual and required a more global perspective. The average OH*-CL intensity, swirling strength, or summed OH area were all roughly equivalent in terms of forecasting power.

5. SUMMARY

Two swirl flames were investigated with varying levels of complexity in their geometry and operating conditions. First, an aviation piloted lean premixed prevaporized injector combusting a synthetic jet fuel was investigated with stereoscopic particle image velocimetry (SPIV). Three operating conditions were chosen based on varying global equivalence ratio and pilot fueling. The stagnation line corresponding to the shear layer between reactant jets and the central recirculation bubble (CRB) is a key feature of a swirl stabilized flame. Therefore, conditioning upon the stagnation line was performed for various measures from the velocity fields. This moves the frame of reference to the stagnation line instead of at a fixed point in space. The flow structures are highly dynamic where at one moment a point may correspond to the CRB and a reactant jet at a different time. The flame with less piloting displayed higher in-plane shear fluctuations and swirling strength than a flame with more piloting. This highlighted the pivotal role of the pilot flame in terms of stabilization of the combustor. More fuel to the pilot injector reduces flow field fluctuations and helps the flame resist perturbations that may arise due to adverse conditions in flight.

The rest of the document consisted of analyzing simultaneous high speed SPIV, OH* chemiluminescence (CL), OH planar laser induced fluorescence (PLIF), and pressure measurements in a less geometrically complex combustor burning natural gas. There are no flame-flame interactions and spray dynamics as seen in the first flame. However, additional complexity is added in the form of thermoacoustic instability driven by equivalence ratio oscillations. Sparse DMD is applied to the velocity fields to decompose the time series into a superposition of two modes with neutral growth rates. One mode corresponds to the thermoacoustic pulsations, and the other matches the staggered vortex structure of the helical precessing vortex core (PVC). A three dimensional velocity field is constructed by converting different phases of the

PVC mode into separate spatial planes. The a vortex with the characteristic helical morphology of the PVC is seen, and the evolution of various flow structures through the thermoacoustic cycle is documented. The CRB shape was observed to vary from symmetric to one containing a helical distortion. Tying the OH*-CL measurements showed that lower intensities occurred when the PVC had less influence on the CRB. The PVC induces intense mixing of the reactants and recirculated hot product gas, which directly influences the heat release rate.

Finally, intermittent flame lift-off and reattachment events are observed in the same flame. These perturbations were short lived, so the previous decomposition techniques did not capture them. Lift-off and reattachment conditioning is performed to calculate statistics for each regime. In addition, a convolutional neural network is implemented to extract quantitative information from the noisy OH-PLIF images. With this methodology, dramatic differences can be observed for the two flame types operating at identical conditions. The lifted flame shows higher velocity fluctuations, a PVC with stronger rotation, and a narrowing of the CRB. These in turn change the morphology of the flame with higher wrinkling and more segmentation.

A bistable flame is undesirable, because combustors are expected to operate in a steady manner. Therefore, the events leading up to flame transition are investigated. Flame lift-off is very sudden with only little forewarning provided by the axial velocity and OH*-CL measurements at the combustor inlet. However, flame reattachment is much more gradual and required a global view of the combustor. Multiple measurements indicated that reattachment is imminent over similar time scales with OH*-CL being the most practical.

REFERENCES

[1] Robert Zhang, Andrew C Pratt, Robert P Lucht, and Carson D Slabaugh. Structure conditioned velocity statistics in a high pressure swirl flame. *Proceedings of the Combustion Institute*, 37(4):5031–5038, 2019.

[2] Robert Zhang, Isaac Boxx, Wolfgang Meier, and Carson D Slabaugh. Coupled interactions of a helical precessing vortex core and the central recirculation bubble in a swirl flame at elevated power density. *Combustion and Flame*, 202:119–131, 2019.

[3] Alwyn Scott. CFM jet engine backlog hits $180 billion as sales rise.

[4] ICAO Council adopts new CO2 emissions standard for aircraft.

[5] Plamen Kasabov and Nikolaos Zarzalis. Pressure dependence of the stability limits and the nox exhaust gas concentrations in case of swirl-stabilized, diffusion flames burning in a lift-off regime. In *ASME Turbo Expo 2009: Power for Land, Sea, and Air*, pages 613–622. American Society of Mechanical Engineers, 2009.

[6] Ahmet E Karataş and Ömer L Gülder. Soot formation in high pressure laminar diffusion flames. *Progress in Energy and Combustion Science*, 38(6):818–845, 2012.

[7] Yi Wu, Vincent Modica, Bjorn Rossow, and Frédéric Grisch. Effects of pressure and preheating temperature on the laminar flame speed of methane/air and acetone/air mixtures. *Fuel*, 185:577 – 588, 2016.

[8] S Daniele, P Jansohn, J Mantzaras, and Konstantinos Boulouchos. Turbulent flame speed for syngas at gas turbine relevant conditions. *Proceedings of the Combustion Institute*, 33(2):2937–2944, 2011.

[9] Bernard L. Koff. Gas Turbine Technology Evolution: A Designers Perspective. *Journal of Propulsion and Power*, 20(4):577–595, 2004.

[10] L. Jofre, J. Urzay, A. Mani, and Parviz Moin. On diffuse-interface modeling of high-pressure transcritical fuel sprays. Technical report, 2015.

[11] B Bork, A Preusche, F Weckenmann, G Lamanna, and A Dreizler. Measurement of species concentration and estimation of temperature in the wake of evaporating n-heptane droplets at trans-critical conditions. In *Proceedings of the Combustion Institute*, volume 36, pages 2433–2440. Elsevier Inc., 2017.

[12] S. CANDEL*, M. JUNIPER†, G. SINGLA, P. SCOUFLAIRE, and C. ROLON. Structure and Dynamics of Cryogenic Flames At Supercritical Pressure. *Combustion Science and Technology*, 178(1-3):161–192, 2006.

[13] Paul E Dimotakis. Turbulent Mixing. *Annual Review of Fluid Mechanics*, 37(1):329–356, 2005.

[14] G. B. Goodwin, R. W. Houim, and E. S. Oran. Effect of decreasing blockage ratio on DDT in small channels with obstacles. *Combustion and Flame*, 173:16–26, 2016.

[15] Seyed G Saddoughi and Srinivas V Veeravalli. Local isotropy in turbulent boundary layers at high reynolds number. *Journal of Fluid Mechanics*, 268:333–372, 1994.

[16] A.H. Lefebvre. *Gas Turbine Combustion*. Combustion: An International Series. Taylor & Francis Group, 1999.

[17] Marcus Hultmark, Margit Vallikivi, SCC Bailey, and AJ Smits. Turbulent pipe flow at extreme reynolds numbers. *Physical review letters*, 108(9):094501, 2012.

[18] Carson D. Slabaugh, Andrew C. Pratt, and Robert P. Lucht. Simultaneous 5 kHz OH-PLIF/PIV for the study of turbulent combustion at engine conditions. *Applied Physics B*, 118(1):109–130, 2015.

[19] I. Boxx, C. Slabaugh, P. Kutne, R. P. Lucht, and W. Meier. 3 kHz PIV/OH-PLIF measurements in a gas turbine combustor at elevated pressure. *Proceedings of the Combustion Institute*, 35(3):3793–3802, 2015.

[20] Ianko Chterev, Nicholas Rock, Hanna Ek, Benjamin Emerson, Jerry Seitzman, Naibo Jiang, Sukesh Roy, Tonghun Lee, James Gord, and Tim Lieuwen. Simultaneous imaging of fuel, OH, and three component velocity fields in high pressure, liquid fueled, swirl stabilized flames at 5 kHz. *Combustion and Flame*, 186:150–165, 2017.

[21] Cheng Huang, Matthew Harvazinski, William Anderson, and Venkateswaran Sankaran. Analysis of Self-Excited Combustion Instability using Decomposition Techniques. *AIAA J.*, 54(September):1–18, 2016.

[22] Carson D. Slabaugh, Andrew C. Pratt, Robert P. Lucht, Scott E. Meyer, Michael Benjamin, Kent Lyle, and Mark Kelsey. The development of an optically accessible, high-power combustion test rig. *Rev. Sci. Instrum.*, 85(3), 2014.

[23] Nicholas Syred. A review of oscillation mechanisms and the role of the precessing vortex core (PVC) in swirl combustion systems. *Progress in Energy and Combustion Science*, 32(2):93–161, 2006.

[24] O. Lucca-Negro and T. O'Doherty. Vortex breakdown: A review. *Progress in Energy and Combustion Science*, 27(4):431–481, 2001.

[25] William E. Lorensen and Harvey E. Cline. Marching cubes: A high resolution 3D surface construction algorithm. *Proceedings of the 14th annual conference on Computer graphics and interactive techniques - SIGGRAPH '87*, 21(4):163–169, 1987.

[26] S. Van Der Walt, Johannes L Schönberger, Juan Nunez-Iglesias, François Boulogne, Joshua D Warner, Neil Yager, Emmanuelle Gouillart, and Tony Yu. scikit-image: image processing in Python. *PeerJ*, 2:e453, 2014.

[27] JMS Prewitt and ML Mendelsohn. The analysis of cell images. *Annals of the New York Academy of Sciences*, 128(1035-1053), 1966.

[28] Sara Gashi, Johan Hult, Karl W. Jenkins, Nilanjan Chakraborty, Stewart Cant, and Clemens F. Kaminski. Curvature and wrinkling of premixed flame kernels-comparisons of OH PLIF and DNS data. *Proceedings of the Combustion Institute*, 30(1):809–816, 2005.

[29] Alan E. Bayley, Yannis Hardalupas, and Alex M K P Taylor. Local curvature measurements of a lean, partially premixed swirl-stabilised flame. *Experiments in Fluids*, 52(4):963–983, 2012.

[30] M. Z. Haq, C. G W Sheppard, R. Woolley, D. A. Greenhalgh, and R. D. Lockett. Wrinkling and curvature of laminar and turbulent premixed flames. *Combustion and Flame*, 131(1-2):1–15, 2002.

[31] Sang Joon Lee, Bu Geun Paik, Jong Hwan Yoon, and Choung Mook Lee. Three-component velocity field measurements of propeller wake using a stereoscopic PIV technique. *Experiments in Fluids*, 36(4):575–585, 2004.

[32] J. Zhou, R. J. Adrian, S. Balachandar, and T. M. Kendall. Mechanisms for generating coherent packets of hairpin vortices in channel flow. *J. Fluid Mech.*, 387:353–396, 1999.

[33] R. J. Adrian, K. T. Christensen, and Z.-C. Liu. Analysis and interpretation of instantaneous turbulent velocity fields. *Exp. Fluids*, 29(3):275–290, 2000.

[34] Ruey Hung Chen and James F. Driscoll. The role of the recirculation vortex in improving fuel-air mixing within swirling flames. *Symp. (Int.) Combust.*, 22(1):531–540, 1989.

[35] Ying Huang and Vigor Yang. Dynamics and stability of lean-premixed swirl-stabilized combustion. *Prog. Energy Combust. Sci.*, 35(4):293–364, 2009.

[36] Sébastien Candel, Daniel Durox, Thierry Schuller, Jean-François Bourgouin, and Jonas P. Moeck. Dynamics of swirling flames. *Annu. Rev. Fluid Mech.*, 46:147–173, 2014.

[37] T C Lieuwen and V Yang. *Combustion instabilities in gas turbine engines: operational experience, fundamental mechanisms and modeling*. Progress in astronautics and aeronautics. American Institute of Aeronautics and Astronautics, 2005.

[38] G A Richards and M C Janus. Characterization of Oscillations During Premix Gas Turbine Combustion. *J. Eng. Gas Turbine Power*, 120(2):294–302, apr 1998.

[39] T. Poinsot. Prediction and control of combustion instabilities in real engines. *Proc. Combust. Inst.*, 36(1):1–28, 2017.

[40] W Meier, P Weigand, X Duan, and R Giezendannerthoben. Detailed characterization of the dynamics of thermoacoustic pulsations in a lean premixed swirl flame. *Combust. Flame*, 150(1-2):2–26, 2007.

[41] Benedetta Franzelli, Eleonore Riber, Laurent Y.M. Gicquel, and Thierry Poinsot. Large Eddy Simulation of combustion instabilities in a lean partially premixed swirled flame. *Combust. Flame*, 159(2):621–637, 2012.

[42] W Meier, I Boxx, M Stohr, and C D Carter. Laser-based investigations in gas turbine model combustors. *Exp. Fluids*, 49:865–882, 2010.

[43] Isaac Boxx, Christoph M. Arndt, Campbell D. Carter, and Wolfgang Meier. High-speed laser diagnostics for the study of flame dynamics in a lean premixed gas turbine model combustor. *Exp. Fluids*, 52(3):555–567, 2010.

[44] Carson D Slabaugh, Isaac Boxx, Stefanie Werner, Robert P Lucht, and Wolfgang Meier. Structure and Dynamics of Premixed Swirl Flames at Elevated Power Density. *AIAA J.*, 54(3):946–961, jan 2016.

[45] Kilian Oberleithner, Michael Stöhr, Seong Ho, Christoph M Arndt, and Adam M Steinberg. Formation and flame-induced suppression of the precessing vortex core in a swirl combustor : Experiments and linear stability analysis. *Combust. Flame*, 162(8):3100–3114, 2015.

[46] Daniel Kroniger, Philipp Vinnemeier, Christian Rudolf, and Manfred Wirsum. High Pressure Combustion Test Rig for 10 MW Full Scale Gas Turbine Combustors. ASME Turbo Expo (2014), 2014.

[47] Scott E Meyer, Stephen D Heister, Carson Slabaugh, Robert P Lucht, Andrew Pratt, Rohan M Gejji, Michael Bedard, and Aaron Lemcherfi. Design and Development of the High Pressure Combustion Laboratory at Purdue University. AIAA Propulsion and Energy Forum (2017), jul 2017.

[48] Oliver Lammel, Harald Schütz, Guido Schmitz, Rainer Lückerath, Michael Stöhr, Berthold Noll, Manfred Aigner, Matthias Hase, and Werner Krebs. FLOX® Combustion at High Power Density and High Flame Temperatures. *J. Eng. Gas Turbine Power*, 132(12):121503, 2010.

[49] W. Meier, P. Weigand, X. R. Duan, and R. Giezendanner-Thoben. Detailed characterization of the dynamics of thermoacoustic pulsations in a lean premixed swirl flame. *Combust. Flame*, 150(1-2):2–26, 2007.

[50] G. P. Smith, D. M. Golden, M. Frenklach, B. Eiteener, M. Goldenberg, C. T. Bowman, R. K. Hanson, S. Song, W. C. Gardiner, V. V. Lissianski, and Z. W. Qin, 2015. `http://www.me.berkeley.edu/gri_mech/`.

[51] J. Westerweel. Efficient detection of spurious vectors in particle image velocimetry data. *Exp. Fluids*, 247:236–247, 1994.

[52] B Wieneke. PIV anisotropic denoising using uncertainty quantification. *Exp. Fluids*, 58(8):1–10, 2017.

[53] Jae S Lim. *Two-dimensional Signal and Image Processing*. Prentice-Hall, Inc., Upper Saddle River, NJ, USA, 1990.

[54] Igor Mezić. Spectral Properties of Dynamical Systems , Model Reduction and Decompositions. *Nonlinear Dyn.*, 41(1-3):309–325, 2005.

[55] Kevin K. Chen, Jonathan H. Tu, and Clarence W. Rowley. Variants of dynamic mode decomposition: Boundary condition, Koopman, and fourier analyses. *J. Nonlinear Sci.*, 22(6):887–915, 2012.

[56] P. J. Schmid. Dynamic mode decomposition of numerical and experimental data. *J. Fluid Mech.*, 656(July 2010):5–28, 2010.

[57] Clarence W Rowley, Igor MeziĆ, Shervin Bagheri, Philipp Schlatter, and Dan S Henningson. Spectral analysis of nonlinear flow. *J. Fluid Mech.*, 641:115–127, 2009.

[58] Sukesh Roy, Jia Chen Hua, Will Barnhill, Gemunu H. Gunaratne, and James R. Gord. Deconvolution of reacting-flow dynamics using proper orthogonal and dynamic mode decompositions. *Phys. Rev. E Stat. Nonlin. Soft Matter Phys.*, 91(1):1–16, 2015.

[59] Timo Buschhagen, Rohan Gejji, John Philo, Lucky Tran, J Enrique Portillo Bilbao, and Carson D Slabaugh. Experimental Investigation of Self-Excited Combustion Instabilities in a Lean, Premixed, Gas Turbine Combustor at High Pressure. *J. Eng. Gas Turbine Power*, 140(11):111503–111509, June 2018.

[60] Taraneh Sayadi, Peter J. Schmid, Franck Richecoeur, and Daniel Durox. Parametrized data-driven decomposition for bifurcation analysis, with application to thermo-acoustically unstable systems. *Phys. Fluids*, 27(3), 2015.

[61] Jonas P. Moeck, Jean François Bourgouin, Daniel Durox, Thierry Schuller, and Sébastien Candel. Tomographic reconstruction of heat release rate perturbations induced by helical modes in turbulent swirl flames. *Exp. Fluids*, 54(4), 2013.

[62] Abdulla Ghani, Thierry Poinsot, Laurent Gicquel, and J. D. Müller. LES Study of Transverse Acoustic Instabilities in a Swirled Kerosene/Air Combustion Chamber. *Flow Turbul. Combust.*, 96(1):207–226, 2016.

[63] Clarence W. Rowley and Scott T.M. Dawson. Model Reduction for Flow Analysis and Control. *Annu. Rev. Fluid Mech.*, 49(1):387–417, 2017.

[64] Maziar S. Hemati, Clarence W. Rowley, Eric A. Deem, and Louis N. Cattafesta. De-biasing the dynamic mode decomposition for applied koopman spectral analysis of noisy datasets. *Theor. Comput. Fluid Dyn.*, 31(4):349–368, Aug 2017.

[65] Scott T M Dawson, Maziar S Hemati, Matthew O Williams, and Clarence W Rowley. Characterizing and correcting for the effect of sensor noise in the dynamic mode decomposition. *Exp. Fluids*, 57(3):1–19, 2016.

[66] Jonathan H Tu, Clarence W Rowley, Dirk M Luchtenburg, Steven L Brunton, and J Nathan Kutz. On Dynamic Mode Decomposition: Theory and Applications. *J. Comput. Dyn.*, pages 391–421, 2014.

[67] Mihailo R. Jovanović, Peter J. Schmid, and Joseph W. Nichols. Sparsity-promoting dynamic mode decomposition. *Phys. Fluids*, 26(2):024103, 2014.

[68] Andrea Ianiro, Kyle P. Lynch, Daniele Violato, Gennaro Cardone, and Fulvio Scarano. Three-dimensional organization and dynamics of vortices in multi-channel swirling jets. *J. Fluid Mech.*, 843:180–210, 2018.

[69] Benjamin Ponitz, Mark Sastuba, and Christoph Brücker. 4D visualization study of a vortex ring life cycle using modal analyses. *J. Vis.*, 19(2):237–259, 2016.

[70] Peter J. Schmid, Daniele Violato, and Fulvio Scarano. Decomposition of time-resolved tomographic PIV. *Exp. Fluids*, 52(6):1567–1579, 2012.

[71] F Güthe and B Schuermans. Phase-locking in post-processing for pulsating flames. *Meas. Sci. Technol.*, 18(9):3036, 2007.

[72] A.M. Steinberg, I. Boxx, M. Stöhr, W. Meier, and C.D. Carter. Effects of flow structure dynamics on thermoacoustic instabilities in swirl-stabilized combustion. *AIAA J.*, 50(4):952–967, 2012.

[73] Isaac Boxx, Campbell D. Carter, Michael Stöhr, and Wolfgang Meier. Study of the mechanisms for flame stabilization in gas turbine model combustors using kHz laser diagnostics. *Exp. Fluids*, 54(5):1532, 2013.

[74] Michael Stöhr, Isaac Boxx, Campbell D. Carter, and Wolfgang Meier. Experimental study of vortex-flame interaction in a gas turbine model combustor. *Combust. Flame*, 159(8):2636–2649, 2012.

[75] M. Stöhr, I. Boxx, C. Carter, and W. Meier. Dynamics of lean blowout of a swirl-stabilized flame in a gas turbine model combustor. *Proc. Combust. Inst.*, 33(2):2953–2960, 2011.

[76] Václav Kolár. Compressibility Effect in Vortex Identification. *AIAA J.*, 47(2):473–475, feb 2009.

[77] M. Stöhr, C. M. Arndt, and W. Meier. Effects of Damköhler number on vortex-flame interaction in a gas turbine model combustor. *Proc. Combust. Inst.*, 34(2):3107–3115, 2013.

[78] P. Weigand, W. Meier, X. R. Duan, W. Stricker, and M. Aigner. Investigations of swirl flames in a gas turbine model combustor: I. Flow field, structures, temperature, and species distributions. *Combust. Flame*, 144(1-2):205–224, 2006.

[79] Zhiyao Yin, Patrick Nau, and Wolfgang Meier. Responses of combustor surface temperature to flame shape transitions in a turbulent bi-stable swirl flame. *Experimental Thermal and Fluid Science*, 82:50–57, 2017.

[80] Michael Stöhr, Kilian Oberleithner, Moritz Sieber, Zhiyao Yin, and Wolfgang Meier. Experimental Study of Transient Mechanisms of Bistable Flame Shape Transitions in a Swirl Combustor. *Journal of Engineering for Gas Turbines and Power*, 140(1):011503, 2017.

[81] Christoph M Arndt, Adam M Steinberg, Isaac G Boxx, Wolfgang Meier, Manfred Aigner, and Campbell D Carter. Flow-field and flame dynamics of a gas turbine model combustor during transition between thermo-acoustically stable and unstable states. In *ASME Turbo Expo 2010: Power for Land, Sea, and Air*, pages 677–687. American Society of Mechanical Engineers, 2010.

[82] Qiang An and Adam M Steinberg. The role of strain rate , local extinction , and hydrodynamic instability on transition between attached and lifted swirl flames. *Combustion and Flame*, 199:267–278, 2019.

[83] Sai Kumar Thumuluru and Tim Lieuwen. Characterization of acoustically forced swirl flame dynamics. *Proceedings of the Combustion Institute*, 32 II(2):2893–2900, 2009.

[84] Davide E. Cavaliere, James Kariuki, and Epaminondas Mastorakos. A comparison of the blow-off behaviour of swirl-stabilized premixed, non-premixed and spray flames. *Flow, Turbulence and Combustion*, 91(2):347–372, 2013.

[85] Sebastian Hermeth, Gabriel Staffelbach, Laurent Y M Gicquel, Vyacheslav Anisimov, Cinzia Cirigliano, and Thierry Poinsot. Bistable swirled flames and influence on flame transfer functions. *Combustion and Flame*, 161(1):184–196, 2014.

[86] Huangwei Zhang, Andrew Garmory, and Davide E Cavaliere. Large Eddy Simulation / Conditional Moment Closure modeling of swirl-stabilized non-premixed flames with local extinction. *Proceedings of the Combustion Institute*, 35(2):1167–1174, 2015.

[87] Andrea Giusti, Maria Kotzagianni, and Epaminondas Mastorakos. LES / CMC Simulations of Swirl-Stabilised Ethanol Spray Flames Approaching Blow-Off. *Flow, Turbulence and Combustion*, pages 1165–1184, 2016.

[88] G. Singla, P. Scouflaire, C. Rolon, and S. Candel. Planar laser-induced fluorescence of OH in high-pressure cryogenic LOx/GH 2 jet flames. *Combustion and Flame*, 144(1-2):151–169, 2006.

[89] Aravind Vaidyanathan, Jonas P. Gustavsson, and Corin Segal. Oxygen/Hydrogen-Planar-Laser-Induced Fluorescence Measurements and Accuracy Investigation in High-Pressure Combustion. *Journal of Propulsion and Power*, 25(4):864–874, 2009.

[90] Craig T. Johansen, Colin D. McRae, Paul M. Danehy, Emanuela C.A. Gallo, Luca M.L. Cantu, Gaetano Magnotti, Andrew D. Cutler, Robert D. Rockwell, Chris P. Goyne, and James C. McDaniel. OH PLIF visualization of the UVa supersonic combustion experiment: Configuration A. *Journal of Visualization*, 17(2):131–141, 2014.

[91] José Pastor and Jesús Benajes. Planar laser-induced fluorescence fuel concentration measurements in isothermal diesel sprays. *Optics Express*, 10(7):309–23, 2002.

[92] A. Buades, B. Coll, and J. . Morel. A non-local algorithm for image denoising. In *2005 IEEE Computer Society Conference on Computer Vision and Pattern Recognition (CVPR'05)*, volume 2, pages 60–65 vol. 2, June 2005.

[93] J. Darbon, A. Cunha, T. F. Chan, S. Osher, and G. J. Jensen. Fast nonlocal filtering applied to electron cryomicroscopy. In *2008 5th IEEE International Symposium on Biomedical Imaging: From Nano to Macro*, pages 1331–1334, May 2008.

[94] Mark Sweeney and Simone Hochgreb. Autonomous extraction of optimal flame fronts in OH planar laser-induced fluorescence images. *Applied optics*, 48(19):3866–3877, 2009.

[95] Rafael Reisenhofer, Johannes Kiefer, and Emily J. King. Shearlet-based detection of flame fronts. *Experiments in Fluids*, 57(3):1–14, 2016.

[96] N. Otsu. A threshold selection method from gray-level histograms. *IEEE Transactions on Systems, Man, and Cybernetics*, 9(1):62–66, Jan 1979.

[97] Pablo Marquez-Neila, Luis Baumela, and Luis Alvarez. A morphological approach to curvature-based evolution of curves and surfaces. *IEEE Transactions on Pattern Analysis and Machine Intelligence*, 36(1):2–17, 2014.

[98] Peer Neubert and Peter Protzel. Compact watershed and preemptive SLIC: On improving trade-offs of superpixel segmentation algorithms. *Proceedings - International Conference on Pattern Recognition*, pages 996–1001, 2014.

[99] Tony Chan and Luminita Vese. An active contour model without edges. In Mads Nielsen, Peter Johansen, Ole Fogh Olsen, and Joachim Weickert, editors, *Scale-Space Theories in Computer Vision*, pages 141–151, Berlin, Heidelberg, 1999. Springer Berlin Heidelberg.

[100] Alex Krizhevsky, Ilya Sutskever, and Geoffrey E Hinton. Imagenet classification with deep convolutional neural networks. In F. Pereira, C. J. C. Burges, L. Bottou, and K. Q. Weinberger, editors, *Advances in Neural Information Processing Systems 25*, pages 1097–1105. Curran Associates, Inc., 2012.

[101] Y. Liu, M. Cheng, X. Hu, J. Bian, L. Zhang, X. Bai, and J. Tang. Richer convolutional features for edge detection. *IEEE Transactions on Pattern Analysis and Machine Intelligence*, pages 1–1, 2018.

[102] Liang-Chieh Chen, Yukun Zhu, George Papandreou, Florian Schroff, and Hartwig Adam. Encoder-decoder with atrous separable convolution for semantic image segmentation. In Vittorio Ferrari, Martial Hebert, Cristian Sminchisescu, and Yair Weiss, editors, *Computer Vision – ECCV 2018*, pages 833–851, Cham, 2018. Springer International Publishing.

[103] K. He, X. Zhang, S. Ren, and J. Sun. Deep residual learning for image recognition. In *2016 IEEE Conference on Computer Vision and Pattern Recognition (CVPR)*, pages 770–778, June 2016.

[104] M. Everingham, S. M. A. Eslami, L. Van Gool, C. K. I. Williams, J. Winn, and A. Zisserman. The pascal visual object classes challenge: A retrospective. *International Journal of Computer Vision*, 111(1):98–136, January 2015.

[105] Dimitrios Marmanis, Mihai Datcu, Thomas Esch, and Uwe Stilla. Deep learning earth observation classification using imagenet pretrained networks. *IEEE Geoscience and Remote Sensing Letters*, 13(1):105–109, 2016.

[106] Hoo-Chang Shin, Holger R Roth, Mingchen Gao, Le Lu, Ziyue Xu, Isabella Nogues, Jianhua Yao, Daniel Mollura, and Ronald M Summers. Deep convolutional neural networks for computer-aided detection: Cnn architectures, dataset characteristics and transfer learning. *IEEE transactions on medical imaging*, 35(5):1285–1298, 2016.

[107] Samet Akçay, Mikolaj E Kundegorski, Michael Devereux, and Toby P Breckon. Transfer learning using convolutional neural networks for object classification within x-ray baggage security imagery. In *2016 IEEE International Conference on Image Processing (ICIP)*, pages 1057–1061. IEEE, 2016.

[108] Luc Vincent. Grayscale area openings and closings, their efficient implementation and applications. In *First Workshop on Mathematical Morphology and its Applications to Signal Processing*, pages 22–27, 1993.

[109] Flavio R Velasco. Thresholding using the isodata clustering algorithm. Technical report, MARYLAND UNIV COLLEGE PARK COMPUTER SCIENCE CENTER, 1979.

[110] Jui-Cheng Yen, Fu-Juay Chang, and Shyang Chang. A new criterion for automatic multilevel thresholding. *IEEE Transactions on Image Processing*, 4(3):370–378, 1995.

[111] C.H. Li and P.K.S. Tam. An iterative algorithm for minimum cross entropy thresholding. *Pattern Recognition Letters*, 19(8):771 – 776, 1998.

[112] P. Malbois, E. Salaün, A. Vandel, G. Godard, G. Cabot, B. Renou, A.M. Boukhalfa, and F. Grisch. Experimental investigation of aerodynamics and structure of a swirl-stabilized kerosene spray flame with laser diagnostics. *Combustion and Flame*, 205:109 – 122, 2019.

[113] Alessandro Schönborn, Parisa Sayad, and Jens Klingmann. Influence of precessing vortex core on flame flashback in swirling hydrogen flames. *International Journal of Hydrogen Energy*, 39(35):20233 – 20241, 2014.

[114] Jian Chen, Jianzhong Li, Li Yuan, and Ge Hu. Flow and flame characteristics of a rp-3 fuelled high temperature rise combustor based on rql. *Fuel*, 235:1159 – 1171, 2019.

[115] Rephael Wenger. *Isosurfaces: geometry, topology, and algorithms*. AK Peters/CRC Press, 2013.

[116] Nicholas A. Worth and James R. Dawson. Cinematographic OH-PLIF measurements of two interacting turbulent premixed flames with and without acoustic forcing. *Combustion and Flame*, 159(3):1109–1126, 2012.

[117] M Klein, H Nachtigal, M Hansinger, M Pfitzner, and N Chakraborty. Flame Curvature Distribution in High Pressure Turbulent Bunsen Premixed Flames. *Flow, Turbulence and Combustion*, pages 1173–1187, 2018.

[118] G Troiani, F Creta, and M Matalon. Experimental investigation of Darrieus – Landau instability effects on turbulent premixed flames. *Proceedings of the Combustion Institute*, 35(2):1451–1459, 2015.

[119] Sophocles J Orfanidis. *Introduction to Signal Processing*. Prentice-Hall, Inc., Upper Saddle River, NJ, USA, 1995.

[120] K Benkrid, D Crookes, and A Benkrid. Design and fpga implementation of a perimeter estimator. In *Proceedings of the Irish Machine Vision and Image Processing Conference*, pages 51–57, 2000.

[121] Ilya Sutskever, James Martens, George Dahl, and Geoffrey Hinton. On the importance of initialization and momentum in deep learning. In *International conference on machine learning*, pages 1139–1147, 2013.

A. Phase Average Quality

Confidence interval estimates are used to assess the quality of the 192 phase averages from the double phase conditioning. A three sigma confidence level is calculated for each phase average and each velocity component. This is interpreted as to mean that 99.7% of repeated experiments contain the true phase average in their confidence intervals. Therefore, smaller confidence intervals are desired as a indication of reduced variance. The variability of an average should be zero in the limit of infinite samples.

All three velocity components at probe locations P1-3 corresponding to figure 3.5 were investigated. However, the widest confidence interval occurred for u_x, so u_y and u_z are not shown for brevity. The variation of the confidence interval of u_x at P2 is shown in figure A.1 for the double phase averages with 192 bins presented in this study. The values represented by the color bar correspond to the half-intervals. For example, the largest confidence interval in figure A.1 occurs at ($\theta_{TA} = 7\pi/6,\ \theta_{PVC} = 9\pi/8$) and is equal to the mean $\pm$ 3.27 m/s. The half-intervals are mainly dependent on θ_{TA} with two bands of larger widths. u_z displays similar patterns but at different θ_{TA} ranges, while u_y shows more dependence on θ_{PVC}.

Table A.1 shows the minimum, maximum, and mean half-interval of each probe location for the phase averages. The labels subscripted with 12×16 denote 192 phase averages used in this work. For contrast, the same confidence interval calculation is performed for double phase averages with the thermoacoustic and PVC phases each split into only 4 bins. In addition, phase averages of the raw dataset are constructed using the instantaneous phase of the 450-460 Hz band-passed dynamic chamber pressure, and the averages are computed for eight phase bins. No phase conditioning on the PVC dynamics is performed on the raw dataset.

As expected, averaging over more velocity fields produces tighter confidence intervals. The mean half-intervals at every probe point for 4×4 is less than the 12×16

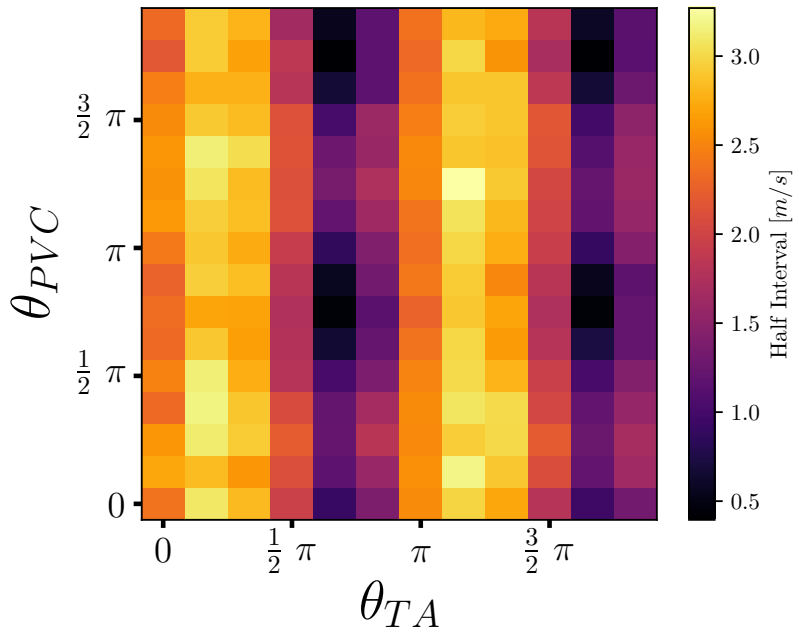

Figure A.1. Confidence half intervals at each phase bin for the u_x velocity component at P2 corresponding to the 12×16 phase bin case.

case. The minimum half-intervals are larger for the 4×4 case, because the larger phase bins contain velocity fields with more variance. The reduction in the mean half-interval between the different bin size configurations is small, because the DMD reconstructed velocity fields are purely sinusoidal with no phase modulation. This is not the case for the raw dataset, which has the largest confidence intervals at P1-2 with a comparable interval as the 12×16 case for P3. More phase bins than the 12×16 case could have been used with small impact to the confidence intervals, but this was enough for reconstructing of the 3D structure of the PVC, CRB, and reactant jets through the thermoacoustic cycle.

Table A.1. Confidence Half Intervals of u_x

Probe	Min	Max	Mean
$P1_{DMD-12\times16\ bins}$	0.24	2.30	1.39
$P2_{DMD-12\times16\ bins}$	0.40	3.27	2.08
$P3_{DMD-12\times16\ bins}$	0.52	2.27	1.44
$P1_{DMD-4\times4\ bins}$	0.40	1.76	1.15
$P2_{DMD-4\times4\ bins}$	1.70	2.13	1.92
$P3_{DMD-4\times4\ bins}$	0.57	1.74	1.15
$P1_{Raw-8\ bins}$	1.59	2.53	2.07
$P2_{Raw-8\ bins}$	2.83	3.84	3.42
$P3_{Raw-8\ bins}$	1.22	1.56	1.44

B. Training Details

The training set consisted of 280 labeled images with 30% corresponding to the lifted flame regime. Only 20 images made up the small validation set. Data augmentation involved random horizontal reflections during training. Each pixel is labeled as either the background, CRB, or upper OSL. The CNN is trained to predict the labels on a per pixel basis. Training is performed using stochastic gradient descent with Nesterov momentum [121]. The learning rate was set to 0.01, momentum kept at 0.9, weight decay equal to 0.0005, and a batch size of 12 fills the available GPU RAM (16 GB). If the previous 5 epochs showed no decrease in training loss, then the learning rate was halved. The cross entropy loss was equally weighted for each class. Training was performed over 50 epochs, which took only 20 minutes on a NVIDIA Tesla V100.

See figure B.1 for the variation in training and validation loss across the epochs. One epoch corresponds to a single cycle through the training set. Labeled data is time consuming, so the validation dataset is far smaller than what is ideal. If the training loss decreases but validation loss increases, then that is a sign of overfitting where generalization to unseen data worsens. The validation loss slowly rises past the 9th epoch while the training loss is steadily decreasing. However, manual inspection of the last epoch still shows good generalization, but segments have smooth edges than earlier epochs. Therefore, the epoch with the lowest validation loss was chosen for this analysis as it produced edges with finer details.

The expert labeled segments from the validation set are shown in figure B.2a,c for an attached and lifted flame, respectively. Likewise, figure B.2b,d shows the output of the CNN before any post-processing. The resulting label for each pixel is equal to the class with the maximum probability from the CNN output. These images demonstrate the capability of the CNN with segments matching very closely to the

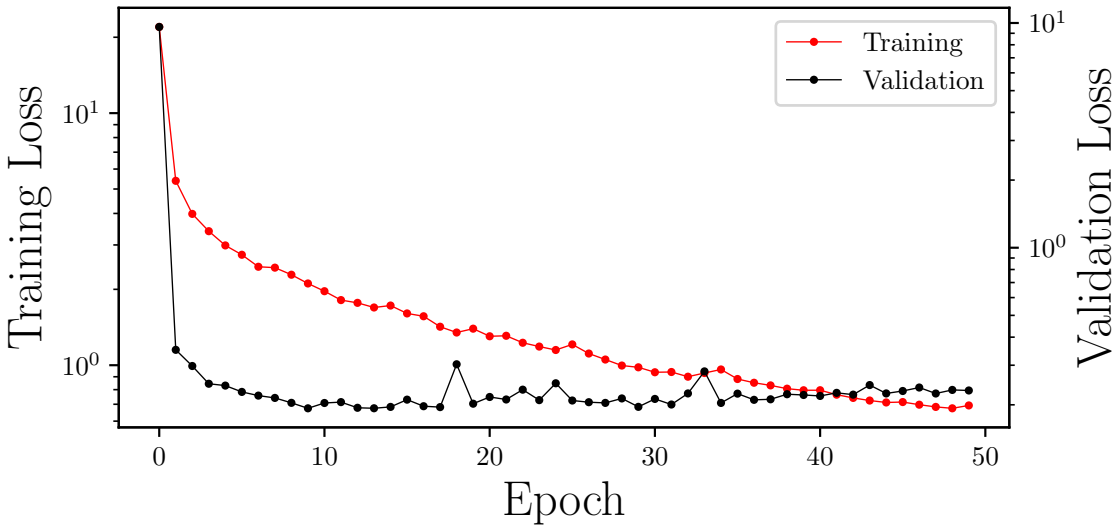

Figure B.1. Training and validation loss over 50 epochs.

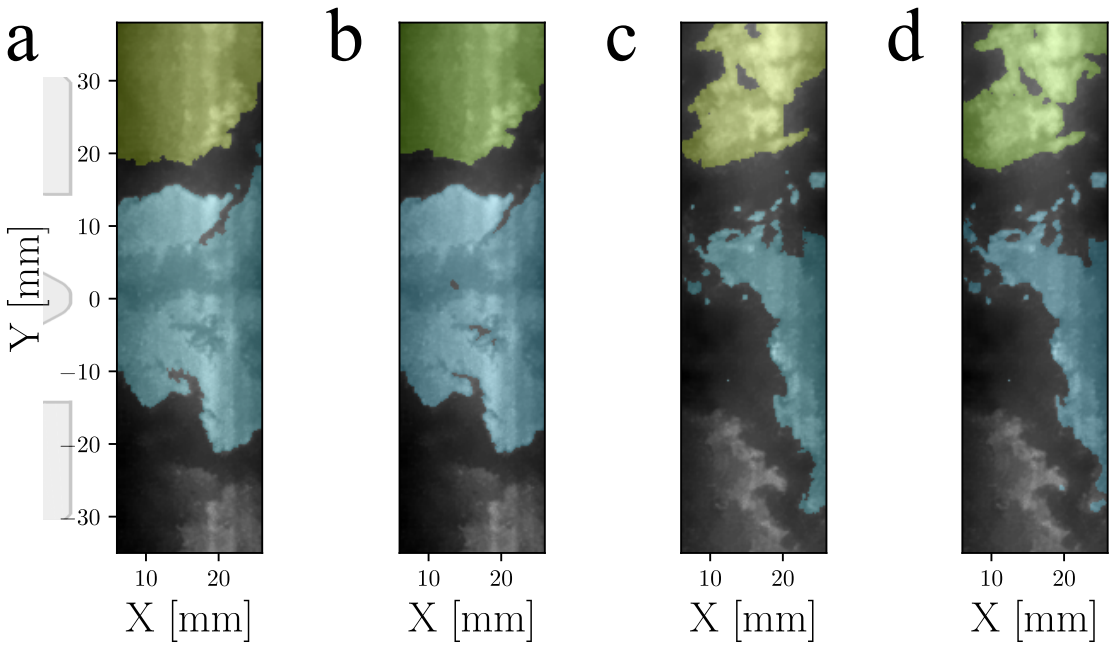

Figure B.2. Examples of manually segmented images (a,c) compared to the output of the CNN (b,d).

ground truth labels. Inference speed was also very fast at 55 images per second. In contrast, manual labeling on average required 180 seconds per image.

VITA

Robert Z. Zhang was born on March 17, 1992 to Yumin Zhang and Qin Zhong. He moved to the United States of American in 1996 from China and spent his childhood throughout the American Midwest. He obtained a Bachelor of Science in Mechanical Engineering at the Missouri University of Science and Technology in 2013. That same year, he enrolled at Purdue University to eventually pursue a doctorate working with Professors Lucht and Slabaugh.